A Systematic Study of Local Active Galactic Nuclei with Infrared and Hard X-ray All-Sky Surveys

Keiko Matsuta

Department of Space and Astronomical Science,
Graduate School of Physical Science,
The Graduate University for Advanced Studies

2013

Abstract

Some galaxies contain compact nuclei, which emit vast amounts of energy over the entire electromagnetic spectrum from radio through gamma-rays, thus called active galactic nuclei (AGN). The powerful activity originates from the release of gravitational energy through accretion of material on to a supermassive black hole with a typical mass in the range of $10^{6-9}M_{\odot}$. Some of the gravitational energy is thermalized in the accretion disk to radiate ultraviolet and soft X-ray emission. Some is channeled into the generation of energetic particles (or jets) and produces X-ray through gamma-ray emission via inverse Compton scattering and radio through X-rays via synchrotron emission. This radiation from the vicinity of the black hole may heat circumnuclear dust in the obscuring torus of clouds, which is believed to exist on parsec scales outside the accretion disk. The warm torus can then be a source of a strong infrared emission. AGN tend to show large variety in their observational properties, such as luminosities, optical line properties, radio brightness, variability, and so on. In spite of such apparent diversity, it is widely believed that the various AGN are intrinsically the same. Just a few parameters - inclination, accretion rate, and presence/absence of jets - may be responsible for the apparent differences. However, details of the geometry of the nuclei, especially of the torus, are poorly known because their angular scales are very small and difficult to resolve spatially.

The main goal of this thesis is to study the geometry of the nuclear emission region based upon unbiased survey data gathered from multiple wavebands. For this purpose, I take two approaches; one is to explore the correlation between hard X-ray and infrared luminosities using unbiased samples systematically for each AGN type. The other is to analyze variability of mid-infrared emission for individual sources and for each AGN type statistically using two all-sky survey catalogs. This is the first large-scale systematic study of mid-infrared variability in AGN, probing timescales of several years separately for different types of AGN.

For the first approach, I used all-sky surveys conducted by *Swift* in the hard X-ray (> 10 keV) band and by *AKARI* in the infrared band. The *Swift*/Burst Alert Telescope all-sky survey provides an unbiased, flux-limited selection of hard X-ray detected AGN. The hard X-ray band is rather insensitive to the photo-electric absorption due to the intervening clouds up to mildly Compton-thick ($N_{\rm H} \sim 10^{24}$ cm^{-2}) column densities. In other words, the hard X-ray flux obtained by the survey reflects the intrinsic luminosity for all Compton-thin AGN and also for mildly Compton-thick ones, thus providing samples largely unbiased by obscuration. In the case of infrared observations, high angular resolution is crucial in order to properly separate AGN from stellar emission in the host galaxy. However, this was not possible until the advent of recent telescopes. The *AKARI* satellite completed an all-sky survey whose catalog was released just before the beginning of this research. This survey is several times more sensitive than previous ones, and was carried out at a much higher angular resolution of the order of arcseconds. Cross-correlating the 22-month hard X-ray survey with the *AKARI* all-sky survey, I studied 158 AGN

detected by both instruments. I find a strong correlation for most AGN between the infrared (9, 18, and 90 μm) and hard X-ray (14–195 keV) luminosities, and quantified the correlation for various complete subsamples of AGN. Partial correlation analysis confirms that the correlation is intrinsic; that is, the correlation between the luminosities remains significant after removing the contribution of redshift. Under the unification scheme of AGN, this result may be viewed as supporting clumpy torus models. The good one-to-one correlation between mid-infrared bolometric luminosities and hard X-ray ones for over four orders of magnitude indicates that the covering factor of torus will decrease with the increase of the intrinsic luminosity. The correlation for radio galaxies has a slope and normalization identical to that for Seyfert 1s, where we have a direct view of the nuclear regions in both hard X-rays and infrared, implying similar hard X-ray/infrared emission processes in both. In contrast, sources with large Compton-thick column densities show a large deficit in the hard X-ray band, because high gas column densities in the torus diminish their apparent luminosities even in the hard X-ray band.

On the other hand, a few radio-loud sources (radio galaxies and blazars) show systematic deviations toward higher X-ray luminosities in the correlations as compared to radio-quiet sources. Origin of the broadband emission of radio galaxies is a matter of considerable debate. One possible explanation of this deviation (i.e., excess X-rays) is the contribution of jets to the hard X-ray emission. Observations of flux variability can be useful for isolating the jet contribution, because strong and rapid fluctuations are characteristic of beamed jet emission. Useful hard X-ray variability data are not yet available, but such data have recently become available in the mid-infrared band. Furthermore, mid-infrared variations can also potentially constrain the geometry of the dusty torus by measuring the response of the torus to changes of the nucleus emission. This leads to the second topic of my thesis to study mid-infrared variability of AGN systematically. I combine two mid-infrared all-sky surveys, i.e., the data released by *AKARI* and Wide-field Infrared Survey Explorer (*WISE*). *WISE* was launched about four years after *AKARI* and accomplished all-sky surveys with high sensitivity in several mid-infrared bands (particularly relevant for my work are the 12 and 22 μm bands). Because the bands observed by the two telescopes are slightly different, I calculated the flux ratio of *WISE* and *AKARI* after subtracting the contribution of band differences, for which the spectral slope calculated for each source was used. In addition, cross-calibration errors of the two telescopes are carefully examined. I find significant mid-infrared variations in 3 sources, 2 blazars and 1 radio galaxy, in either or both of the 9 and 18 μm bands. Although no significant variations are detected from the rest of the sources, low level variations may be hidden in statistical errors. Therefore, I tried to constrain the average sample variability for different AGN types, which was actually detected from Seyfert 1 in the 9 μm band. This is the first detection of variability from Seyfert 1 by using two mid-infrared all-sky surveys. I quantified the amplitudes of sample variability and found that the amplitude reaches $\sim$10% in 4 years for Seyfert 1 in the 9 μm band. If this variability is explained by the torus emission only, dust distribution in the torus should be compact, although other possibilities, such as jet contribution, cannot be excluded. Combining the results of the hard X-ray vs. mid-infrared correlations and mid-infrared variability, geometry and structure of the obscuring torus are discussed.

Contents

1 Introduction **1**

1.1 Active Galactic Nuclei . . . 1

1.2 Classification of AGN . . . 1

1.2.1 Seyfert galaxy . . . 2

1.2.2 Quasar . . . 2

1.2.3 Low-ionization nuclear emission line region . . . 2

1.2.4 Radio galaxy . . . 3

1.2.5 Blazar . . . 3

1.2.6 Compton-thick AGN . . . 3

1.3 The unified model of AGN . . . 4

1.4 Emission from AGN . . . 6

1.4.1 Optical and UV emission . . . 6

1.4.2 X-ray emission . . . 6

1.4.3 Infrared emission . . . 7

1.4.4 Emission from jet . . . 7

1.5 Correlations of the infrared and X-ray emission from AGN . . . 8

1.6 Variability of emission from AGN . . . 9

1.7 Aims of the PhD Thesis . . . 11

2 Infrared and hard X-ray correlations of AGN from *Swift*/BAT and *AKARI* all-sky survey **13**

2.1 Introduction . . . 13

2.2 Observation and Data Selection . . . 14

2.2.1 The *Swift*/BAT 22-month Source Catalog . . . 14

2.2.2 The *AKARI* Point Source Catalogue . . . 14

2.2.3 Source identification . . . 15

2.3 Analysis and Results . . . 17

2.3.1 Redshift, Flux distribution and Completeness . . . 17

2.3.2 Hard X-ray to IR luminosity correlation . . . 17

3 Infrared variability of AGN **27**

3.1 Introduction . . . 27

3.2 *WISE* All-Sky Source Catalog . . . 28
3.2.1 The Wide-field Infrared Survey Explorer . . . 28
3.2.2 The *WISE* All-Sky Source Catalog . . . 29
3.3 Cross-identification of sources . . . 30
3.4 Analysis and Results . . . 32
3.4.1 Sample properties . . . 32
3.4.2 Relative flux variations . . . 33
3.4.3 Correction of the wave band differences . . . 34
3.4.4 Variability criteria . . . 38
3.4.5 Fractional of variability in mid-IR band . . . 43

4 Discussion **47**
4.1 Correlation for each type of AGN . . . 47
4.1.1 Correlation for Seyfert AGN . . . 47
4.1.2 Correlation for Compton-thick AGN . . . 48
4.1.3 Correlation for radio-loud AGN . . . 50
4.1.4 Constraints on the torus geometry . . . 52
4.1.5 Summary of the correlation for each type of AGN . . . 53
4.2 Variability of mid-infrared emission from AGN . . . 54
4.2.1 Variable sources in mid-IR band . . . 54
4.2.2 Fractional of variability for each type of AGN . . . 55
4.2.3 Correlation between variability and torus radius . . . 55
4.2.4 Other origins of variability . . . 56
4.3 Correlation between variability and luminosity . . . 56

5 Conclusion **59**

A Photometric diagnostics for source classification **61**
A.1 Radio-loud AGN . . . 61
A.2 Compton-thick AGN . . . 63
A.3 Distinction between Compton-thick AGN and Starburst galaxies . . . 63
A.3.1 starburst–AGN connection . . . 63
A.3.2 color–color diagnostic . . . 64
A.3.3 *K*-corrections in the color–color plane . . . 66

B SEDs with *AKARI* and *WISE* **69**

C Relative calibration error between *AKARI* and *WISE* **79**

Bibliography **81**

Acknowledgment **89**

List of Figures

1.1 Schematic picture indicating the unified model of AGN 5
1.2 Schematic representation of broadband continuum spectral energy distribution seen in the different types of AGN 8
1.3 Mid-infrared and X-ray luminosity correlation for the sample of 42 VISIR detections and one additional object 10

2.1 Diagram showing the *AKARI* flight system 15
2.2 Redshift distribution of all AGN detected in the *Swift*/BAT 18
2.3 Hard X-ray flux distribution for the *Swift*/BAT sources 19
2.4 Logarithmic luminosity correlations between the *AKARI* and *Swift*/BAT 24
2.4 *Continued.* (b) 18 μm. 25
2.4 *Continued.* (c) 90 μm. 25

3.1 The *WISE* flight system in survey configuration with cover off 28
3.2 Distribution of the angular separation in right ascension and declination between the source positions of the cross-identified sources in *WISE* and *AKARI* catalog . 33
3.3 Distribution of the relative flux ratio between *AKARI* and *WISE* 34
3.4 Distribution of the power-law slopes and their errors of SED with *AKARI* and *WISE* bands 35
3.5 Distribution of relative flux ratio between *AKARI* and *WISE* due to the difference of the observation bands 37
3.6 Distribution of $\Delta F - \Delta F_0$ between *AKARI* and *WISE* 38
3.7 Distribution of the variability criteria defined in Equation 3.9 40
3.8 Same as Figure 3.7, but the center part of the histograms is magnified 40
3.9 Distribution of relative variability of intensity for the total sample of AGN 44
3.10 Distribution of relative variability of intensity for Seyfert 1, Seyfert 2 and type 1 RL AGN 45

4.1 Logarithmic luminosity correlations between the *AKARI* and *Swift*/BAT, when hard X-ray luminosities of Compton-thick AGN in the sample are corrected for obscuration using the columns listed in Table 4.1. 50

A.1 Absolute magnitude vs. Color diagram for 89 *Swift*/BAT and *AKARI* detected sources 62
A.2 Color-color plot of log $L_{\rm X}/\lambda L_{9\mu{\rm m}}$ vs. log $\lambda L_{9\mu{\rm m}}/\lambda L_{90\mu{\rm m}}$ for 89 AGN including 9 Compton-thick sources and 7 starburst galaxies detected by *AKARI* 66

B.1 SEDs of Seyfert 1 with *AKARI* and *WISE* 69
B.1 *Continued.* 70
B.1 *Continued.* 71
B.1 *Continued.* 72
B.2 SEDs of Seyfert 2 with *AKARI* and *WISE* 73
B.2 *Continued.* 74
B.3 SEDs of type 1 radio-loud AGN with *AKARI* and *WISE* 75
B.4 SEDs of type 2 radio-loud AGN with *AKARI* and *WISE* 76
B.5 SEDs of Compton-thick AGN with *AKARI* and *WISE* 76
B.6 SEDs of Blazar with *AKARI* and *WISE* 77
B.7 SEDs of LINER with *AKARI* and *WISE* 77

C.1 Signal-to-Noise ratio of A- and F-type stars detected by *AKARI* and *WISE* bands 79
C.2 Distribution of ΔF for A- and F-type stars between *AKARI* and *WISE* bands . . 80

List of Tables

1.1 Taxonomy of AGN unifications 5

2.1 *AKARI* infrared propaties of the AGN in the 22-month *Swift*/BAT catalog . . . 20
2.1 *Continued.* 21
2.1 *Continued.* 22
2.2 Summary of cross-identifications 23
2.3 Summary of the fitting results 26

3.1 Summary of the cross-identification 32
3.2 Statistics of ΔF 35
3.3 Statistics of slopes of infrared SEDs 36
3.4 Statistics of ΔF_0 38
3.5 Statistics of $\Delta F - \Delta F_0$ 39
3.6 Sources variable at >5 sigma significance level 41
3.7 Statistics of variability criteria R 42
3.8 Statistics of variability fraction 44

4.1 Properties of Compton-thick AGN 49

A.1 The sample of starburst galaxies 65

C.1 Statistics of ΔF of stars 80

Chapter 1

Introduction

In this chapter, I am going to review the active galactic nuclei (AGN) making stress on the unified model from both observational and theoretical sides. In addition to the review, I will summarize recent studies on correlations of infrared-to-X-ray emission and variability of infrared emission from AGN, which are main topics of the present thesis.

1.1 Active Galactic Nuclei

Some galaxies contain compact nuclei, which are active, emitting vast amounts of energy over the entire electromagnetic spectrum from radio through gamma rays, thus called active galactic nuclei (AGN). The origin of this powerful activity is the release of gravitational energy through accretion of material on to a supermassive black hole (SMBH) with a typical mass in the range of $10^{6-9}M_{\odot}$. Some of the gravitational energy is thermalized in the accretion disk to radiate ultraviolet (UV) and soft X-ray emission. Some is channeled into the generation of energetic particles (or jets) and produces X-ray through gamma-ray emission via inverse Compton scattering and radio through X-rays via synchrotron emission. This radiation from the vicinity of the black hole may heat circumnuclear dust in an obscuring torus of clouds, which is believed to exist on parsec scales outside the accretion disk. The warm torus can then be a source of a strong infrared (IR) emission.

1.2 Classification of AGN

AGN tend to show large variety in their observational properties, such as luminosities, optical line properties, radio brightness, variability, and so on. In spite of these apparent differences, it is widely believed that the various AGN are intrinsically the same. Just a few parameters – inclination, accretion rate, and presence/absence of jets – are responsible for the apparent differences. In the following subsections, I review various AGN types based on their observational properties.

1.2.1 Seyfert galaxy

There are two largest subclasses of AGN, Seyfert galaxies and quasars. They are distinguished by their luminosities. In the case of a typical Seyfert galaxy, the total energy emitted by the nucleus at visible wavelengths is comparable to the energy emitted by all of stars in the galaxy (i.e., $\sim 10^{11} L_{\odot}$). On the other hand, in the case of a typical quasar, the nucleus is brighter than that of a Seyfert by a factor of 100 or more. The criteria of Seyferts with B-band magnitude $M_B > -23$ is generally accepted (Schmidt & Green, 1983). Host galaxies of Seyferts are in most cases late type galaxies.

Seyfert galaxies are classified by their spectral properties as Seyfert (Sy) 1 and 2 (Antonucci, 1993). The latter show permitted and forbidden lines from a narrow line region (NLR) in their spectra. Typically, the full width at half maximum (FWHM) of the lines is $\sim$200-900 km s^{-1} and the ratio of line intensity F([O III]λ5007)/F(Hβ)$\sim$10. Sy 1s have the same characteristics, but in addition, exhibit permitted lines (FWHM $\sim 10^3 - 10^4$ km s^{-1}) from a broad line region (BLR). They also show strong variable featureless continua whose strength is in proportion to their broad line emission.

As the strength of the narrow components increase relative to the broad components, AGN are sometime assigned to type 1.5, 1.8, and 1.9 (Osterbrock, 1989). In Sy 1.5, the strengths of the broad and narrow line components in Hβ are comparable. Those with strong narrow components, and very weak but still visible broad components of Hα and Hβ, are often called Sy 1.8. Those in which a weak broad component may be seen at Hα, but none at Hβ, are called Sy 1.9.

1.2.2 Quasar

Quasars compose the most luminous subclass of AGN, with B-band magnitudes $M_B < -23$. Their spectra are remarkably similar to those of Seyferts, except that stellar absorption features are very weak, if detectable at all, and the narrow lines are generally weaker relative to the broad lines compared to the case in Seyferts. In this sense, quasars may be regarded as the brighter end of Seyferts. However, few quasars to show type 2 characteristics are known. About 5–10% of quasars are strong radio sources.

1.2.3 Low-ionization nuclear emission line region

Low-ionization nuclear emission line region (LINER) constitutes the low luminosity end of AGN, which has an optical spectrum dominated by emission-lines from low ionization states (Heckman, 1980). Any broad lines and featureless continua are swamped by starlight and are generally not detected. Spectroscopically, they resemble Sy 2, except that the low-ionization lines (e.g., [O I]λ6300, [N II]$\lambda\lambda$6548, 6583) are relatively strong.

1.2.4 Radio galaxy

AGN may be divided by their activity and/or luminosity in the radio band. Approximately 10% of AGN are classified as radio-loud AGN, which show prominent radio jet and/or lobe emission. Radio galaxies are characterize by their radio-luminous density at 5 GHz to be larger 10^{32} erg s^{-1} Hz^{-1} and by the radio to optical B-band flux density ratio (R_B) to satisfy log $R_B \geq 1$ (Kellermann et al., 1989; Xu et al., 1999; Molina et al., 2008). Strong radio-sources are typically found as giant elliptical galaxies. Two types of radio galaxies are identified with their optical spectra as broad-line radio galaxies (BLRGs, type 1 radio-loud AGN) and narrow-line radio galaxies (NLRGs, type 2 radio-loud AGN), which are counterparts of Sy 1 and Sy 2 in radio-quiet AGN.

The extended radio structures are further divided into two luminosity classes (Fanaroff & Riley, 1974). FR I sources are relatively weak radio sources, which are brightest in the center, with decreasing surface brightness towards the edges. In contrast, the more luminous FR II sources are limb-brightened, and often show regions of enhanced emission (i.e., lobe). The dividing luminosity between the two classes is given by L_ν (1.4 GHz) = 10^{32} erg s^{-1} Hz^{-1} (Bridle & Perley, 1984).

1.2.5 Blazar

A small subset of AGN shows short time-scale (as short as a day) variations with large amplitude ($\Delta m \geq 0.1$ mag) than other AGN in visible wavelengths. In addition to their large variations in flux, they also tend to have high polarization up to a few percent (as opposed to less than $\sim$1% for most AGN). These AGN are known as "optically violent variables (OVVs)". Some of the properties of OVVs are shared by "BL Lac objects", which were originally identified as highly variable stars. BL Lac objects are distinguished from OVVs by the absence of strong emission or absorption lines in their spectra. It is thought that both OVVs and BL Lacs are similar AGN, which have strong relativistically beamed jets close to the line of sight. Collectively, OVVs and BL Lacs are referred to as "blazars". They are also radio-loud sources.

Flat-spectrum radio-loud quasars (FSRQs, Angel & Stockman, 1980) share basically all of the properties of BL Lac objects such as the presence of a strong non-thermal broadband continuum, except for the absence of broad emission lines. Blazars are divided into weak-lined sources (like BL Lac) and strong-lined sources (like FSRQ), both containing essentially similar relativistic jets. BL Lac and FSRQ correspond to FR I (i.e., low luminosity radio galaxy) and FR II (i.e., high luminosity radio galaxy), respectively (Padovani, 1992).

1.2.6 Compton-thick AGN

Some AGN in the local universe are obscured in the X-ray band by large amounts of gas and dust, which prevent observations of their nuclear emission up to energies that depend on the amount of intrinsic absorption. If the X-ray obscuring matter has a column density, which is equal to or larger than the inverse of the Thomson cross-section ($N_H \geq \sigma_T^{-1} \simeq 1.5\times10^{24}$ cm^{-2}), then the source is called Compton-thick AGN. The cross-sections for Compton scattering and

photoelectric absorption (for mater of cosmic abundance) have approximately the same value for energies around 10 keV, which can be considered as the low energy threshold for probing the Compton-thick absorption regime. Indeed, if the column density does not exceed a value of order 10^{25} cm^{-2}, then the nuclear radiation is visible above 10 keV, and the source is called mildly Compton-thick AGN. For higher column densities (heavily Compton-thick AGN), the entire high-energy spectrum is down scattered by Compton recoil and hence depressed over the entire X-ray energy range. The presence of Compton-thick matter may be inferred through indirect arguments, such as the presence of a strong Fe Kα line complex at 6.4–7 keV and the characteristic reflection spectrum.

Compton-thick AGN are important for several reasons. One reason is that a large fraction of AGN (at least a half of Sy 2) in the local universe may be obscured by Compton-thick gas (Maiolino et al., 1998; Risaliti et al., 1999; Matt, 2000). However, Compton-thick AGN with already measured column density occupies only a small fraction of AGN. Thus, more extensive search is required. Another reason is that a sizable population of mildly Compton-thick AGN is postulated in all the AGN synthesis models for the X-ray background (XRB) in order to match the intensity peak of the XRB spectrum at about 30 keV (Ueda et al., 2003). Also, accretion in the Compton-thick AGN may contribute to the local black hole mass density. Unfortunately, the most efficient energy range to search for mildly Compton-thick AGN, i.e., >10 keV is just above the accessible range to the past and most of the present satellites with imaging capabilities. In this sense, recently launched NuSTAR[1], which carries X-ray focusing optics above 10 keV for the first time in space, is highly expected.

1.3 The unified model of AGN

AGN are classified into various types by their observed features (in Section 1.2). In spite of the large variety, AGN may be intrinsically a single phenomenon explained by a few numbers of physical parameters together with the observer-dependent parameters. This lead to the idea of the unified model. The basic scheme of the unified model consists of an accreting SMBH surrounded by an obscuring torus (Figure 1.1, Urry & Padovani, 1995). Matter accreting on to the center black hole form a luminous accretion disk. In optical band, broad-line emission is produced in clouds (i.e., BLR) orbiting around the disk. Some continuum and broad-line can be scattered into the line of sight by hot electrons in BLR. Also, narrow-line emission is produced in clouds (i.e., NLR) much farther from the central source. Some AGN emit bipolar jets from the region near the black hole at relativistic speed.

In the unified model, the key elements are luminosities, viewing angle to torus (inclination), and presence of jets. I summarize the basic idea of the unified model of AGN in Table 1.1. Firstly, AGN are divided by their radio loudness, which originate from prominent radio jet and/or lobe emission. Secondly, viewing angle to obscuring torus separates AGN. If the torus is seen face-on (such sources are classified as "type 1", which include Sy 1, Quasar, and BLRG), we can see the central region directly. If our viewing angle is close to edge-on (such sources are

[1] http://www.nustar.caltech.edu/

Table 1.1: Taxonomy of AGN unifications

Radio properties	Orientation			luminosity
	Pole-on (type 0)	Face-on (type 1)	Edge-on (type 2)	
Radio-quiet	—		LINER	low
	—	Seyfert 1	Seyfert 2	↕
	—	Quasar		high
Radio-loud	Blazar (BL Lac)		(FR I)	low
				↕
	Blazar (FSRQ)	BLRG	NLRG (FR II)	high

classified as "type 2", which include Sy 2, LINER, and NLRG), we cannot see the central region directly. Typically, the former spectra has both narrow and broad emission lines, and the latter has only narrow lines in their emission because the torus prevent us from observing emission from central broad line region. Blazars (including BL Las and FSRQ) are classified as "type 0" because their axes of jets stay parallel to the line of sight (i.e., "pole-on").

Typical sizes of these emission and obscuration regions are as follows. If we take a central black hole of a mass of $10^8 M_\odot$, as an example, it has a typical size of the radius $\sim 10^{13}$ cm; the accretion disk emits mostly from $\sim 10^{15}$ cm; the broad line region are located within $\sim 10^{16}$ cm of the black hole; and the inner radius of the dusty torus is $\geq 10^{17}$ cm. The narrow-line region extends $\geq 10^{18}$ cm; and radio jets are detected on scales ranging 10^{17-24} cm.

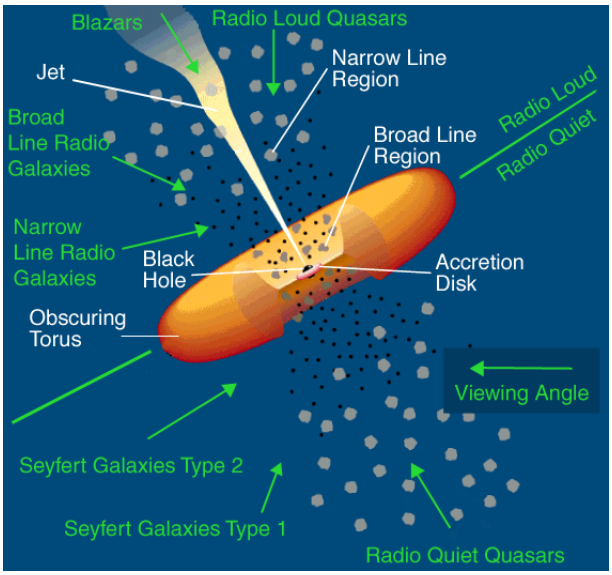

Figure 1.1: Schematic picture indicating the unified model of AGN (Urry & Padovani, 1995).

Jaffe et al. (2004) revealed that the warm (320 K) dust in 2.1×3.4 parsec surround a smaller hot (800 K) region in the galaxy NGC 1068 by using interferometric observations with the Very Large Telescope Interferometer (VLTI). However, it is generally difficult to resolve dust distribution because the central region is too small to resolve. Pier & Krolik (1992, 1993) suggested a torus with cylindrical geometry and homogeneous smooth dust distribution by

using two-dimensional radiative transfer algorithm. On the other hand, Krolik & Begelman (1988) discussed that smooth dust distribution probably cannot survive in the vicinity of an AGN and the dust is arranged in clouds. Nenkova et al. (2002) and Dullemond & van Bemmel (2005) showed results of radiative transfer calculations of such a clumpy medium and suggested that a torus consisting of clouds is capable of suppressing the silicate emission and absorption. Structure and geometry of the dust torus are still not clear and are matters of intense studies.

In addition, it is not clear whether the torus of the Compton-thick AGN conform that of the unified model. Some people conjecture that partially or heavily obscured AGN need not be edge on, since obscuring material only needs to block the observer's sightline (e.g., Elvis, 2000; Risaliti et al., 2002; Miller et al., 2008). They suggested the partial covering is caused by a clumpy gas wind from the accretion disk.

1.4 Emission from AGN

AGN emit broadband radiation over the entire electromagnetic spectrum. Figure 1.2 shows the mean spectral energy distribution (SED) of different types of AGN. In this section, I will give a brief description on the characteristics and origin of the emission in each wave band.

1.4.1 Optical and UV emission

Between the optical and UV bands (0.1–1 μm), there is a dominant and strong broad feature, called "big blue bump", which emit a copious amount of energy. The big blue bump is usually attributed to thermal emission in the range of $10^{5\pm1}$ K. If the emission is optically thick, it is usually considered to be originated from the accretion disk. If so, relativistic effects should produce significant polarization in the accretion-disk continuum, and a Lyman edge (at 912Å), in either emission or absorption, is expected because the opacity changes dramatically at Lyman edge. However, they are not well established observationally. Various reasons are considered for the absence of the edge structure under the assumption of the accretion disk origin of the bump. But, no consensus is reached yet.

1.4.2 X-ray emission

The X-ray emission accounts for typically $\sim$10% of bolometric luminosity of AGN and is produced at the innermost region. The X-ray emission of Seyfert galaxies consists of several components, including a power law continuum in the 1–10 keV range ($\alpha \simeq 0.9$, where $F_\nu \propto \nu^{-\alpha}$), soft excess usually below 1 keV, and a reflection hump in the 10–30 keV range. The nuclear X-ray emission (> 0.1 keV) from AGN is produced by Comptonization of the UV/optical photons from the accretion disk in a hot corona surrounding the disk (Sunyaev & Titarchuk, 1980; Haardt & Maraschi, 1993), with a possible exception of jet-dominated sources. The soft excess is generally considered as the hard tail of blackbody radiation (i.e., big blue bump) from accretion disk. In the spectra of Seyfert galaxies, Fe 6.4 keV line emission is often detected which is attributed to fluorescence of cold material (Mushotzky et al., 1993). The Fe K line and reflection hump in

hard X-ray band are consistent with the idea that the primary X-rays are reflected in optically thick material.

1.4.3 Infrared emission

The average SED also displays a strong IR bump around 1–100 μm, where a significant portion of their power emerges (e.g., Antonucci, 1993; Elitzur, 2008). Its source is considered to be a pc-scale torus of dust and gas clouds. The high-energy disk and corona emission heat the dusty tori located far from the center, where the nuclear UV-to-X-ray continuum is re-processed into thermal IR photons, which are not dominated by beamed emission from relativistic jets (e.g., Elitzur, 2008). There are some strong evidences that the IR continuum in non-blazar AGN is thermal in origin. One is the 1 μm minimum in the spectra (Sanders et al., 1989), which corresponds to the gap between the big blue bump and the thermal emission from dust at a temperature of $\sim$2000 K corresponding to sublimation temperature of dust grains. Second is the delay of near-IR continuum emission to UV/optical continuum emission, which is interpreted as the light travel time because the IR emission region (i.e., torus) is separated from the UV/optical emission region (i.e., accretion disk). Third is the submillimeter break, i.e., the decrease in submillimeter SEDs. At these long wavelengths, a thermal spectrum can produce a sharp cut-off because the emission efficiency of small grains drop off as $F_\nu \propto \nu^{2+\gamma}$, where γ represents the frequency dependence of emissivity .

1.4.4 Emission from jet

In the case of the emission from jet-dominant AGN (e.g., blazars), the broadband spectra are thought to be dominated by non-thermal emission from their relativistic jets (Bregman, 1990; Fossati et al., 1998; Donato et al., 2001). The IR regime is explained mainly by synchrotron radiation. In the case of FSRQs, the X-ray component is produced by the inverse-Compton scattering of seed photons within the jet (synchrotron self-Compton process, SSC) or external to the jet (e.g., within the BLR or dusty tori). In the case of low-power BL Lacs, the high-energy tail of the synchrotron continuum typically produces the X-ray component. In principle it is possible to produce the high-energy emission via the SSC process. The SSC process becomes important when the synchrotron radiation density becomes sufficiently high that the emitted photons are inverse-Compton scattered off electrons, which are responsible for the synchrotron radiation. The SSC model predicts polarization of a few percent, which are observed in continuum only from blazars. Various observations support a picture that much of the radio through optical emission originates in an inhomogeneous plasma jet through which shocks propagate (Bregman, 1990). A shock wave passing through an adiabatic, conical, relativistic jet not only reproduces this broadband variability, but also naturally leads to relatively flat radio spectra.

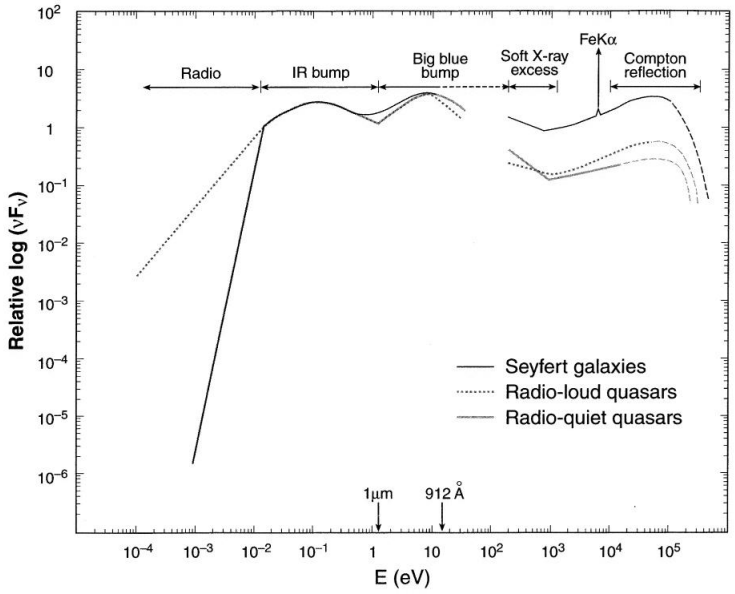

Figure 1.2: Schematic representation of broadband continuum spectral energy distribution (SED) seen in the different types of AGN (Koratkar & Blaes, 1999). The spectra of AGN can be divided into three major components; the big blue bump, the infrared bump, and the emission of X-ray region. The ordinate is normalized logarithmic intensity as νF_ν. The abscissa is log energy in units of eV. Bold-solid line shows the SED of Seyfert galaxies. Dashed and thin-solid lines show SEDs of radio-loud and radio-quiet quasars, respectively.

1.5 Correlations of the infrared and X-ray emission from AGN

Correlations of emission from different wavebands are a potentially powerful tool for investigating the geometry of nuclear region and emission mechanisms. Especially, correlations between IR and X-ray bands have been investigated well in order to obtain information from the innermost region of AGN. Since the 1980s, space-based telescopes have provided a wealth of new information in the previously unexplored IR and X-ray wavelengths. For the samples measured in X-rays (2–10 keV), mostly Sy 1s, Carleton et al. (1987) found that the 3–10 μm luminosities are tightly correlated with the X-ray luminosities, while the UV and far-IR luminosities are not. Mulchaey et al. (1994) found that distribution of the flux ratio of IR (sum of 25 and 60 μm) -to-X-rays (2–10 keV, corrected for observed absorption) emitted from AGN are similar between Sy 1s and Sy 2s. Using larger samples, Lutz et al. (2004) found that there is no significant difference between Sy 1s and Sy 2s in the average ratio of mid-IR-to-absorption-corrected X-ray emission. With the high angular resolution in the mid-IR imaging by VLT/VISIR, Horst et al. (2006, 2008) could exclude any significant non-torus contribution to the mid-IR continuum, and they found similarity in the mid-IR-to-X-ray (12.3 μm-to-2-10 keV) luminosity ratio between Sy 1s and Sy 2s, which is intrinsic to AGN. Augmenting samples with their previous observations and with published intrinsic X-ray fluxes, Gandhi et al. (2009) found strong mid-IR vs. X-ray luminosity correlation for AGNs and that unobscured, obscured, and Compton-thick sources

follow the similar luminosity correlation (Figure 1.3). The fact that unobscured, obscured, and Compton-thick sources all closely follow the same luminosity correlation has important implications for the structures of Seyfert cores.

However, because samples observed in soft X-ray (< 10 keV) band are strongly biased to small line-of-sight column densities, we need to correct absorption effect in fluxes. The X-ray fluxes of Compton-thick AGN, especially, are completely absorbed in soft X-ray band. On the other hand, hard X-ray luminosities (> 10 keV) and IR luminosities are relatively insensitive to obscuration than the soft X-rays. Using *Swift*/Burst Alert Telescope (BAT, 14–195 keV) Survey 9-month AGN Catalog (Tueller et al., 2008), Mushotzky et al. (2008) found that the near-IR nuclear *J*- (1.21 μm) and *K*-band (2.18 μm) luminosity is correlated with the BAT luminosity over a factor of 10^3 in luminosity ($L_{\rm IR} \approx L_{\rm BAT}^{1.25}$). Also, it is found that the [OIV] 25.89 μm emission-line luminosity is an accurate indicator of the intrinsic power of the AGN based on the good correlation between [OIV] and BAT luminosities of X-ray selected nearby Seyferts (Meléndez et al., 2008; Rigby et al., 2009).

X-ray emission from AGN is generally attributed to the nuclear engine itself and heats the circumnuclear dust, which in turn becomes the source of the nuclear mid-IR emission. As noted before, there is a good linear correlation between the logarithms of the observed continuum emission in the mid-IR and the intrinsic soft X-ray (< 10 keV) band luminosities of local AGN, which appears to be largely independent of the amount of dust reddening (e.g., Krabbe et al., 2001; Lutz et al., 2004; Horst et al., 2006, 2008; Gandhi et al., 2009; Levenson et al., 2009; Asmus et al., 2011). This is not expected according to the pioneering AGN dust torus model (Pier & Krolik, 1993), which assumed homogeneous and smooth dust distribution, because IR emission from the warm-inner clouds is expected to be dramatically scattered and reduced when viewed from an edge-on orientation. On the contrary, observations show tight correlations with little scatter and no IR depletion, largely independent of orientation (which ought to be correlated approximately with dust reddening) at all AGN luminosities. Under the torus paradigm, correlations may be consistent with models having a clumpy obscuring geometry (e.g., Krolik & Begelman, 1988; Dullemond & van Bemmel, 2005; Hönig et al., 2006; Nenkova et al., 2008; Schartmann et al., 2008; Hönig et al., 2010; Hönig & Kishimoto, 2010), in which the inner torus regions can be visible even at edge-on orientations.

1.6 Variability of emission from AGN

Variability of emission from AGN is precious information to probe the nuclear regions because it is difficult to resolve them on parsec scale (i.e., torus and/or interior region) directly by the present resolution power of a single telescope.

Strong UV and X-ray variability is common to AGN on a wide range of timescales with the most rapid variations seen in X-rays (e.g., McHardy, 1988; Grandi et al., 1992; Mushotzky et al., 1993). By studying light curves and spectra, long-term (from days to months) and short-term (from hours to days) variability are observed from most of AGN with amplitude up to a factor of 50 or so (Ulrich et al., 1997). Both the soft excess below 1 keV and the X-ray

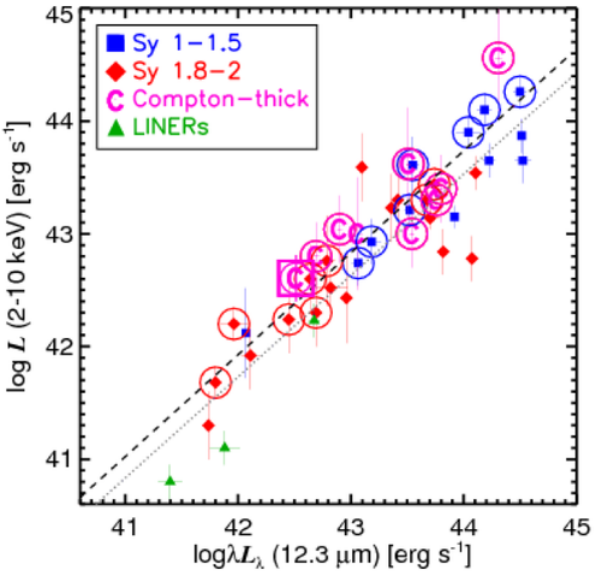

Figure 1.3: Mid-infrared and X-ray luminosity correlation for the sample of 42 VISIR detections and one additional object (ESO 428-G014, "C" with both a box and a circle around it, Gandhi et al., 2009). The sources classified as being "well-resolved" are circled, and the diagonal dashed line is the fitted correlation. The dotted grey line is the correlation fit to all 42 sources.

power-law component (1–10 keV) are variable. In radio-quiet AGN, the X-ray variability results from the emission from the innermost region of accretion disk. In the innermost region, hot optically thin plasma surrounding and/or mixed with the optically thick plasma gives rise to the X-ray emission. However, the origin of the soft X-ray emission in the reprocessing model is not established. An attractive possibility is that the soft excess is due to reprocessing of the Comptonized emission into thermal radiation. This clearly has strong implications on the expected correlation of variability in different bands.

The UV/optical continuum variability seems to be correlated with the X-ray variability with little time delay. This means that the UV/optical emission may be due to the reprocessing of the X-ray emission from the central source. Some models explain that the UV/optical flux is emitted by an optically thick medium (i.e., accretion disk) irradiated by the variable central X-ray source (Haardt & Maraschi, 1993).

On the other hand, IR variations have smaller amplitude and longer time scale than that in UV/optical bands (Neugebauer et al., 1989; Hunt et al., 1994). In near-IR band, variations with time scales on the order of years are seen in the radio-loud quasars, whose amplitude is less than 1 mag. Variations of Seyfert 1s and quasars of 226 samples were studied in near-IR for a time scale of a few years (Enya et al., 2002a,b,c). About a half of the sources showed significant variations. They argued that near-IR variability of the radio-quiet AGN is consistent with a simple dust reverberation, but that of radio-loud AGN may require a non-thermal variable component. Unfortunately, in the mid-IR band, there is no strong and rapid variation than X-ray and UV/optical emissions. A few sources show variability on timescale of a year, whose

average variation reaches ∼10% at 10 μm (Gorjian et al., 2004). Long-term monitoring of 25 quasars for several decades at near- and mid-IR showed that several radio-loud sources displayed significant variability at 10 μm band suggestive of non-thermal origin (Neugebauer & Matthews, 1999). The IR continuum shows a significant time delay compared to variations of UV/optical continuum. The delay is explained by thermal radiation from dust lying at ∼1 light-year from UV/optical energetic source (Clavel et al., 1989). Launch of several IR satellites in 2000s enable us to make statistical analysis of variability for large samples of data. Kozłowski et al. (2010) carried out first systematic mid-IR variability analysis using *Spitzer* deep-wide field survey of the Boötes field in the NOAO Deep Wide Field Survey. Out of 474,179 sources, which include both galactic and extra-galactic sources, 1.1% of the sources are found to be variable. They estimated about 76% of the sources are AGN. The mid-IR AGN variability was found to be well described by a single power-law structure function. The mean amplitude of variation was ∼0.1 mag at both 3.6 and 4.5 μm on time scale of 2 years.

Radio-loud AGN (i.e., Blazars) exhibit the most rapid and the largest amplitude variations among all the AGN and the variations affect the whole electromagnetic range from the radio to the gamma-ray band (Stein et al., 1976; Angel & Stockman, 1980). The combination of extreme variability and relatively weak spectral features suggests that the continuum is emitted by a relativistic jet close to the line of sight and hence that the observed radiation is strongly amplified by relativistic beaming (Blandford & Ostriker, 1978). Mechanisms for variability involve essentially two possibilities, shock waves moving along the jet and rotation of the beaming cone across the line of sight; both could be relevant at different times or in different objects.

Optical monitoring of AGN has been done for many samples and general properties of variability are studied statistically. However, IR variability data of AGN obtained so far are far less than that of optical.

1.7 Aims of the PhD Thesis

Main goal of this thesis is to study the nature and geometry of the nuclear emission region based upon unbiased survey data gathered from multiple wavebands. For this purpose, I take two approaches; one is to explore the correlation between the hard X-ray and IR luminosities using unbiased samples systematically for each AGN type. The other is to analyze variability of mid-IR emission both for individual sources and for each type of AGN statistically using two all-sky survey catalogs. This is the first large-scale systematic studies of AGN variability in mid-IR in time scales of several years. Because of the large sample, it becomes possible to study variability separately for each type of AGN.

Previous works are based on small and incomplete samples, with selection criteria biased toward bright sources visible in the mid-IR from the ground or sources in which the intrinsic soft X-ray power could be determined. Furthermore, it is difficult to determine unabsorbed fluxes from the data only below 10 keV, and to separate various emission components through detailed modeling of the spectrum (e.g., power law, obscuration, scattering, non-thermal emission of relativistic jets in case of the radio-loud sources, and thermal emission of hot gaseous interstellar

medium). Recently, new information becomes available in the hard X-ray band above 10 keV, which reflect intrinsic luminosity of the source.

In the IR band, high angular resolution is believed to be crucial in order to properly separate AGN from stellar emission of the host galaxy (e.g., Gandhi et al., 2009; Horst et al., 2009; Vasudevan et al., 2010; Mullaney et al., 2011). Recent all-sky surveys in IR band have reached sensitivity several times higher than the previous survey.

This paper is organized as follows. In section 2, I describe details of the sample selection and catalog cross matching with *Swift*/BAT and *AKARI* all-sky surveys. I show the main results obtained from the hard X-ray and IR luminosity correlation. In section 3, I explain details of analyses of variability in the mid-IR band with *AKARI* and *WISE* all-sky surveys. I try to treat both the statistical and systematic errors accurately to evaluate variability of sample AGN. In section 4, I discuss the nature and geometry of AGN inferred from the correlation and variability studies. Section 5 describes the main conclusions.

Chapter 2

Infrared and hard X-ray correlations of AGN from *Swift*/BAT and *AKARI* all-sky survey

2.1 Introduction

I use the *Swift*/Burst Alert Telescope (BAT) hard X-ray (> 10 keV) survey as the base AGN selection catalog. The hard X-ray energy band is rather insensitive to the intervening column density up to mildly CT columns. The survey reflects the intrinsic luminosity of the source and provides samples largely unbiased by obscuration. I use the *Swift*/BAT 22-month Source Catalog herein (Tueller et al., 2010). The *AKARI* survey thus provides the best IR sample for cross-correlation with *Swift* AGN. High angular resolution is crucial in order to properly separate AGN from stellar emission in the IR band (e.g., Gandhi et al., 2009; Horst et al., 2009; Vasudevan et al., 2010; Mullaney et al., 2011). For many years, *IRAS* provided the most complete all-sky survey (Joint Iras Science, 1994), but with an angular resolution only of order arcmins. The *AKARI* satellite (Murakami et al., 2007) has now completed its all-sky survey which is several times more sensitive than *IRAS*, and at a much higher angular resolution of order arcsecs, ($7''$ and $48''$ for the mid- and far-IR instruments, respectively).

This work is closely related to that of Ichikawa et al. (2012), in which the relation between the IR/X-ray spectra of Seyferts and new type AGN are studied by using the *Swift*/BAT 9-month AGN Catalog (Tueller et al., 2008) and the *AKARI*/PSC complemented by those with *IRAS* and *WISE* to ensure high completeness of cross identification. The larger 22-month BAT sample used as the starting catalog for the present work includes several heavily CT AGN and radio-loud (RL) sources, and I can compare the regions occupied by these various AGN classes in the luminosity correlation plane. I also provide detailed statistical tests and correlation fits, and construct AGN photometric classification plots.

2.2 Observation and Data Selection

I used the following two all-sky survey catalogs to study the correlation in a complete, flux-limited sample and examine the luminosity correlation between the observed IR and hard X-ray bands of local AGN ($z < 0.1$); the *Swift*/BAT 22-month Source Catalog and the *AKARI*/PSC.

2.2.1 The *Swift*/BAT 22-month Source Catalog

The prime objective of the *Swift*/BAT is the study of gamma-ray bursts, covering the hard X-ray band of 14–195 keV. In the 22-month BAT catalog, the total source count is 461 (above a significance of 4.8σ), of which 268 (58%) are AGN. The catalog includes source information of optical counterpart position, X-ray flux, flux error, luminosity, redshift, and AGN type. I adopted the position of the optical counterpart as the source position. The counterpart position error is usually less than $4''$. The detection limit of the catalog is 2.3×10^{-11} erg cm^{-2}s^{-1} (for 50% sky coverage). The faintest source included in the catalog has $F_{14-195\ \mathrm{keV}} = 0.28 \times 10^{-11}$ erg cm^{-2}s^{-1}. Although progressively-deeper BAT catalogs are becoming available (e.g., Cusumano et al., 2010), the flux limit of the *AKARI* all sky survey is well-matched for detection of a large fraction of the 22-month X-ray catalog in the infrared, as I show below. Thus, I have restricted ourselves to the 22-month sample for AGN analysis in the present work.

The *Swift*/BAT survey produces a long-term average flux, so variability is expected to be partially smoothed over, as compared to large stochastic fluctuations on weekly or monthly timescales. I defined a minimum flux error of 10%, in order to account for low-order long term variations.

I adopted the spectroscopic AGN types from the BAT catalog for most sources, but for some AGN I checked other works because these source classifications are ambiguous [NGC 235A, NGC 612, ESO 549-G049, NGC 3998, WKK 1263, 4C 50.55, and 3C 445, Véron-Cetty & Véron (2010); NGC 4945, Moorwood et al. (1996); NGC 4992, Bodaghee et al. (2007); Circinus Galaxy, Matt et al. (2000); 3C 345, Unwin et al. (1997)]. I excluded AGN defined as 'confused and confusing with nearby sources' in the BAT catalog. Finally, I identified all radio-loud AGN in the combined sample, including type 1 objects such as broad-line radio galaxies and blazars correctly recognized in the BAT classification, and also type 2 sources including narrow-line radio galaxies and low-power FR I radio galaxies which in the BAT catalog are classified simply as Seyfert galaxies (or LINERs) based solely on the characteristics of their optical spectra and regardless of their radio properties.

2.2.2 The *AKARI* Point Source Catalogue

I use data available in the *AKARI* Point Source Catalogs (*AKARI*/PSC; Ishihara et al., 2010; Yamamura et al., 2010) over a range of wavelengths from 9–160 μm. *AKARI* has two instruments; the Infrared Camera (IRC) and the Far-infrared Surveyor (FIS). The IRC band centers are 9 and 18 μm, and the FIS band centers are 65, 90, 140, and 160 μm. The *AKARI*/PSC contains the positions and fluxes of 870,973 (IRC) and 427,071 (FIS) sources. In the *AKARI*/PSC,

the IRC 80% flux completeness limits are 0.12 and 0.22 Jy, respectively. Also, the FIS 80% completeness corresponds to 3.3, 0.43, 3.6, and 8.2 Jy, respectively. The FIS may be incomplete or show a larger flux error due to detector saturation for sources brighter than ∼100 Jy. The angular resolution is 7″ (IRC) and 48″ (FIS), respectively. Although *AKARI*'s angular resolution is lower than large ground telescopes (e.g., the diffraction limit of the Very Large Telescope/VISIR ∼0.3″ in the *N*-band), our study has the capability of probing predominantly nuclear emission in the mid-IR (in addition to hard X-rays). This is because torus emission typically dominates over nuclear stellar emission in AGN host galaxies in the wavelength regime of 10–20 μm (e.g., Mor et al., 2009).

In the *AKARI*/PSC, there is a quality flag, *FQUAL*, par band. This flag is a four-level (3-0) flux quality indicator, and the *AKARI* team recommends using only sources with $FQUAL = 3$ for secure scientific analysis. Although sources with $FQUAL = 2$ or 1 may have flux values reported (Yamamura et al., 2010), I used only sources that are confirmed and described by the quality flag $FQUAL = 3$, indicating high reliability of detection and flux accuracy.

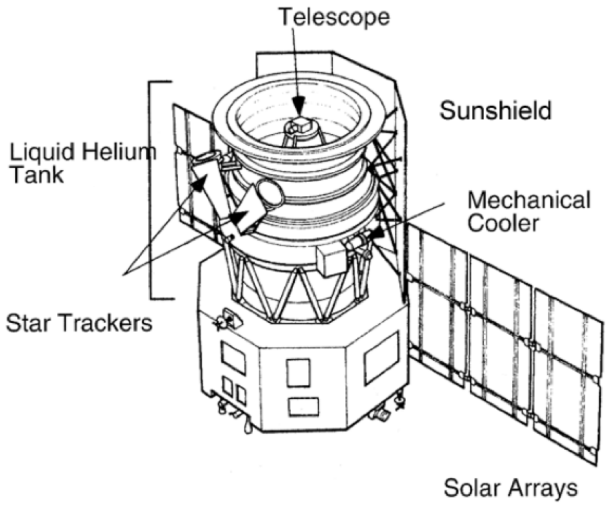

Figure 2.1: Diagram showing the *AKARI* flight system.

2.2.3 Source identification

I searched for IR counterparts within a 10″ radius for the IRC, and 20″ radius for the FIS around the position of every optical counterpart listed in the BAT catalog using the *AKARI* Catalog Archive Server (CAS; Yamauchi et al., 2011), which provides user interfaces to search and obtain *AKARI*/PSC information. I adopted these search radii based upon the ∼3σ position uncertainties for each of the *AKARI*/PSC.

I concentrated on three *AKARI* IR bands (9, 18, and 90 μm) throughout this paper because other FIS bands have poorer sensitivities. I summarized the selected source parameters (name, IR fluxes, X-ray luminosity, redshift, AGN type) in Table 2.1. Additionally, I summarized the total sample statistics for the three *AKARI* bands in Table 2.2. For the 268 AGN included in

the BAT catalog, 158 AGN (∼59%) are detected in at least one of the IRC and FIS bands (111 in 9 μm; 129 in 18 μm; 113 in 90 μm). These 158 AGN are classified into 81 Seyfert 1 (Sy 1) type AGN (∼51%, including Seyfert 1, 1.2, and 1.5), 67 Seyfert 2 (Sy 2) type AGN (∼42%, including Seyfert 1.8, 1.9, and 2), 4 Low-ionization nuclear emission-line regions (LINERs; ∼3%), and 6 blazars (∼4%). Four blazars are flat-spectrum radio quasars (FSRQs), and two are BL Lac objects.

For the purpose of investigating the IR vs. hard X-ray luminosity correlation for various classes of objects, I divide our sample into the following ten categories:

1. "All"
2. "All, ex CT"
3. "Sy 1"
4. "Sy 1, ex RL"
5. "Sy 2"
6. "Sy 2, ex CT"
7. "CT"
8. "RL"
9. "Blazar"
10. "RL + Blazar".

"All" contains all sources detected by the *AKARI* and *Swift*/BAT. "All, ex CT" excludes CT AGN from "All". "CT" is defined as sources obscured by a gas column density $N_{\rm H} \geq 1.5 \times 10^{24}$ cm^{-2} as measured from X-ray spectroscopy. "Sy 1" combines type 1 AGN including radio-quiet objects (Seyferts) and radio-loud sources such as broad-line radio galaxies (BLRGs) and quasars. "Sy 1, ex RL" excludes RL AGN from "Sy 1". "Sy 2" combines type 2 AGN including CT objects, radio quiet Seyferts, and radio-loud sources such as narrow-line radio galaxies and low-power FR I radio galaxies. "Sy 2, ex CT" excludes CT AGN from "Sy 2". "RL" combines all radio-loud AGN in the sample except of blazars, i.e., all radio galaxies of different morphological and spectral types. "Blazar" combines FSRQs and BL Lacs. Finally, "RL + Blazar" merges the two radio loud subsamples.

The criterion of classification as a RL (non-blazar) AGN is that the radio luminosity density at 5 GHz is at least 10^{32} erg s^{-1} Hz^{-1} and the radio to optical B-band flux density ratio (R_B) satisfies log $R_B \geq 1$ (Kellermann et al., 1989; Xu et al., 1999; Molina et al., 2008). RL objects are identified in the final column of Table 2.1. This list includes 3C and 4C sources from the Cambridge catalogs of radio galaxies, as well as other famous RL sources such as Cen A.

A few additional objects were also identified as RL based on a detailed inspection of the available data and literature. NGC 1052 is a Gigahertz-peaked spectrum (GPS) source, with a spectral peak at 10 GHz (Vermeulen et al., 2003). Although the 5 GHz power is lower than the RL classification threshold, this source displays strong parsec-scale radio emission probably related to newly born jets, and is classified as RL. [HB89]1821+643 is a peculiar radio source, lying at the boundary of the radio-quiet/radio-loud divide (Blundell & Rawlings, 2001). The source is a highly luminous quasar in X-rays ($L_{\rm X} > 1 \times 10^{47}$ erg s^{-1}; Russell et al., 2010) and lies at the center of a massive galaxy cluster. It shows an FR I like radio morphology

(Blundell & Rawlings, 2001). As I discuss below, the *AKARI* observations now show that the IR properties of [HB89]1821+643 are consistent with other RL sources, so I include it within the RL classification herein, as a radio-intermediate (RIM) object. Similarly, two other RIM sources are [HB89]0241+622 (Molina et al., 2008) and Mrk 1501 (Barvainis et al., 2005).

There are several narrow-line Seyfert 1s (NLS1s) in the sample, but these are not distinguishable from the other Seyferts so I do not treat them separately.

2.3 Analysis and Results

2.3.1 Redshift, Flux distribution and Completeness

Figure 2.2 shows redshift distribution of the *Swift*/BAT AGN, split into the classes of *AKARI*-detected or non-detected objects. The median redshift of the detected sources ($z_{\rm med}$) is ≈ 0.0222, so most are local AGN. There are only 8/158 sources (5%) with $z > 0.1$. The detected source with the maximum redshift is 3C 454.3 ($z_{\rm max} \approx 0.8590$). The low-$z$ population is dominated by "regular" (radio-quiet) Seyferts, while the high-z population is made mostly from radio-loud AGN (blazars, luminous radio galaxies). The $z_{\rm med}$ for those not detected in any band is $z_{\rm med} \approx 0.0517$.

Figure 2.3 shows hard X-ray flux distribution of the *Swift*/BAT AGN. The X-ray fluxes of the *AKARI* detected sources are higher than the non-detected sources on average. The median X-ray fluxes of the *AKARI* detected/non-detected sources are 5.07/3.38, 4.70/3.36, and 4.70/3.45 $\times$ 10^{-11} erg cm^{-2} s^{-1} in 9, 18, and 90 μm, respectively.

Our cross-correlation between the all-sky X-ray and IR samples is about 60% complete, with the X-ray sources non-detected in the IR being fainter than the detected ones, on average. It has been shown by Ichikawa et al. (2012) that supplementing the *AKARI* data with the deeper *WISE* samples maintains the luminosity correlation. Overall, none of the statistical inferences presented in the sections below should be affected by incompleteness of the cross-matching.

2.3.2 Hard X-ray to IR luminosity correlation

Figure 2.4 shows the luminosity correlation for the detected sources between hard X-ray (14–195 keV) and IR (9, 18, and 90 μm) bands. I find that there is a strong linear correlation for most AGN between the logarithms of the observed IR and hard X-ray luminosities over four orders of magnitude. Here, I calculated the absolute luminosities by using the redshift listed in the BAT catalog (Tueller et al., 2010). In principle, K-correction may become important for high-z objects, e.g., blazars. Our samples are mainly local AGN, but blazars ($z = 0.0533$–0.8590) are also included. If I apply K-correction to AGN at $z \sim 0.9$, the maximum effect for $L_{\rm X}$ is $\sim$10% assuming a power law spectrum with a photon index of $\Gamma \sim 1.9$, which is a typical value for the majority of AGN in our sample. This is a small effect especially when comparing logarithmic luminosities, so I did not apply any K-corrections.

I tested the luminosity correlation by using the algorithm of Isobe et al. (1990), which is used when the nature of the scatter of points in a correlation is ill understood. I computed the linear

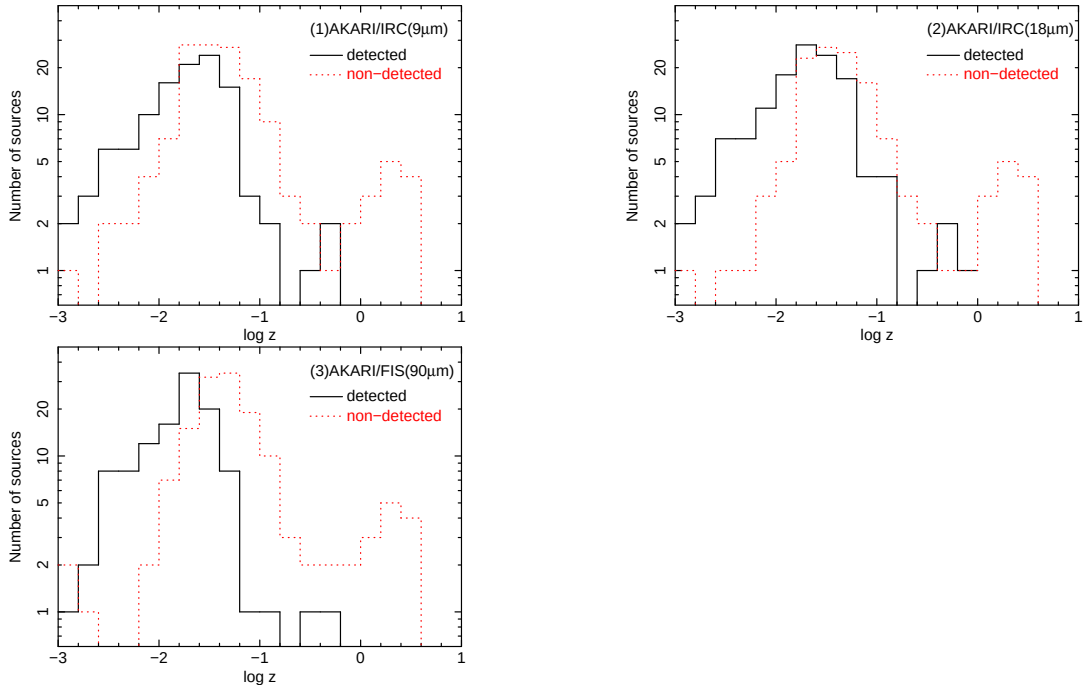

Figure 2.2: Redshift distribution of all AGN detected in the *Swift*/BAT. The values of redshift were taken from those listed in the 22-month *Swift*/BAT hard X-ray survey catalogue (Tueller et al., 2010). The abscissas are logarithmic redshift. The ordinates are total number of sources. Black solid lines show the *AKARI* detected sources (*AKARI*/PSC; $FQUAL = 3$ only), while red dotted lines show the sources not listed in the *AKARI*/PSC.

regression coefficients by one of the methods of the algorithm, "OLS bisector", recommended if the goal is to determine the functional relation between the two axes. The formula is given by

$$\log L_{\rm IR} = a + b \log L_{\rm X}, \tag{2.1}$$

where $L_{\rm IR}$ and $L_{\rm X}$ are observed luminosities in IR (9, 18, and 90 μm) and hard X-ray (14–195 keV). The variables a and b are the intercept and slope of the fitting result, respectively. At 9 μm, the luminosity correlation of the subsample "Sy 1" is described as

$$\begin{aligned} \log\left(\frac{\lambda L_{9\mu\rm m}}{10^{43}\ \rm erg\ s^{-1}}\right) &= (0.15 \pm 0.05) \\ &+(0.94 \pm 0.06) \quad \log\left(\frac{L_{\rm X}}{10^{43}\ \rm erg\ s^{-1}}\right). \end{aligned} \tag{2.2}$$

The fit parameters for other bands are listed in Table 2.3, and are plotted in Figure 2.4 along with the 1σ and 2σ uncertainties on the correlation normalization. Also, I summarize the fitting results with respect to various subsamples in Table 2.3.

I checked two correlation coefficients for every subsample, the Spearman's Rank correlation coefficient (ρ) and the partial correlation coefficient ($\rho_{.z}$). The ρ and $\rho_{.z}$ correlation tests return values in the interval [-1.0, 1.0]. The $\rho_{.z}$ statistic is especially important because artificial correlations between luminosities may be induced in a flux limited-sample even in the absence of any intrinsic correlation, but the partial correlation coefficient can account for this by excluding

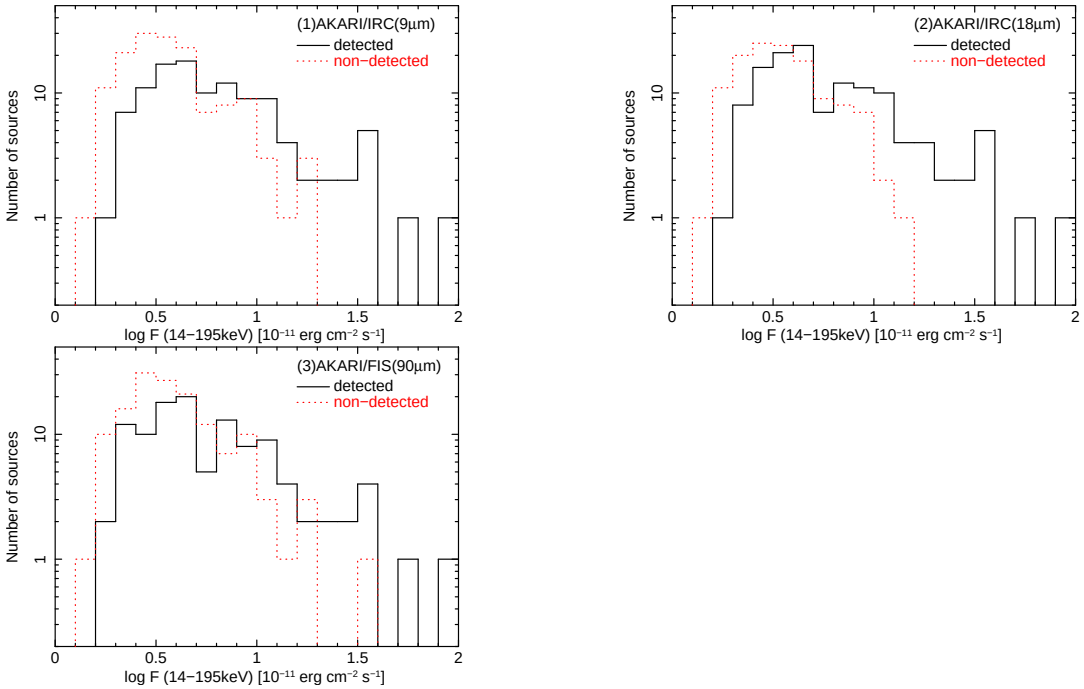

Figure 2.3: Hard X-ray flux distribution for the *Swift*/BAT sources. The abscissa is logarithmic hard X-ray flux. The ordinate is the number of sources. Black solid lines show the *AKARI* detected sources, while red dotted lines show those are not detected by *AKARI* in 3σ.

the effect of redshift. A large value implies a significant positive, linear correlation. These test coefficients values are also listed in Table 2.3.

"Blazar" and "RL + Blazar" typically show very high values of ρ and $\rho_{.z}$ in all three *AKARI* bands. But only a handful of objects included in both subsamples are among the most luminous and distant sources in the entire sample considered, so the correlation results for these may be biased by small number statistics and flux limits. The ρ and $\rho_{.z} = 1$ values in these cases must be treated with caution. The other subsamples with the highest values of ρ and $\rho_{.z}$ are the "Sy 1" and "All, ex CT" subsamples. "Sy 2" also show a correlation, if CT sources are excluded, though somewhat weaker than "Sy 1". CT sources will be discussed separately in section 4.1.2. The correlation coefficients generally decrease towards longer IR wavelengths.

Table 2.1: *AKARI* infrared propaties of the AGN in the 22-month *Swift*/BAT catalog

Serial NO.	BAT No.	Object name	$Flux_{09}$ (mJy)	$Flux_{18}$ (mJy)	$Flux_{90}$ (mJy)	log L_X (erg s^{-1})	Redshift	Type
(1)	(2)	(3)	(4)	(5)	(6)	(7)	(8)	(9)
1	1	Mrk 335	128 ± 3	223 ± 46	...	43.52 ± 0.07	0.0258	Sy1.2
2	2	Mrk 1501	...	134 ± 21	...	44.82 ± 0.05	0.0893	Sy1.2/RIM
3	3	2MASX J00253292+6821442	75 ± 8	216 ± 22	...	42.94 ± 0.09	0.0120	Sy2
4	8	NGC 235A	...	295 ± 32	...	43.61 ± 0.05	0.0222	Sy1[a]
5	9	Mrk 348	...	593 ± 43	736 ± 60	43.79 ± 0.04	0.0150	Sy2
6	21	NGC 526A	141 ± 14	292 ± 26	...	43.64 ± 0.04	0.0191	Sy1.5
7	22	Fairall 9	229 ± 20	440 ± 24	...	44.35 ± 0.04	0.0470	Sy1
8	23	NGC 513	...	...	2533 ± 107	43.20 ± 0.08	0.0195	Sy2
9	24	NGC 612	135 ± 34	...	2604 ± 261	43.98 ± 0.04	0.0298	Sy2[a]/RL
10	25	ESO 297-018	...	...	672 ± 67	43.97 ± 0.04	0.0252	Sy2
11	27	MCG -01-05-047	...	139 ± 7	2597 ± 225	43.22 ± 0.07	0.0172	Sy2
12	28	NGC 788	...	312 ± 25	...	43.54 ± 0.04	0.0136	Sy2
13	34	NGC 931	349 ± 12	763 ± 48	2430 ± 64	43.56 ± 0.04	0.0167	Sy1.5
14	35	IC 1816	55 ± 32	265 ± 20	1473 ± 54	43.17 ± 0.07	0.0170	Sy1.8
15	36	NGC 973	...	93 ± 77	1704 ± 69	43.21 ± 0.07	0.0162	Sy2
16	37	NGC 985	165 ± 14	368 ± 38	1291 ± 16	44.11 ± 0.05	0.0430	Sy1
17	41	NGC 1052	146 ± 34	377 ± 17	793 ± 36	42.27 ± 0.07	0.0050	Sy2/RL
18	42	NGC 1068	24923 ± 188	72285 ± 27	202591 ± 28886	42.03 ± 0.06	0.0038	Sy2/CT
19	43	[HB89] 0241+622	300 ± 14	635 ± 34	576 ± 80	44.52 ± 0.04	0.0440	Sy1/RIM
20	44	2MASX J02485937+2630391	...	...	1398 ± 25	44.42 ± 0.08	0.0579	Sy2
21	47	NGC 1142	265 ± 16	380 ± 71	7036 ± 178	44.23 ± 0.04	0.0289	Sy2
22	50	NGC 1194	169 ± 7	415 ± 56	530 ± 42	43.13 ± 0.07	0.0136	Sy1
23	54	NGC 1275 (3C 084)	442 ± 26	1989 ± 21	6928 ± 245	43.63 ± 0.04	0.0176	Sy2/RL
24	55	B2 0321+33 NED02	...	95 ± 4	...	44.56 ± 0.07	0.0610	Sy1
25	57	PKS 0326-288	...	152 ± 7	...	44.88 ± 0.09	0.1080	Sy1.9
26	60	NGC 1365	2234 ± 38	5364 ± 43	80384 ± 13546	42.64 ± 0.04	0.0055	Sy1.8/CT
27	64	ESO 548-G081	...	...	968 ± 61	43.28 ± 0.04	0.0145	Sy1
28	68	2MASX J03534246+3714077	...	...	827 ± 78	43.06 ± 0.10	0.0183	Sy2
29	70	ESO 549- G049	156 ± 15	302 ± 43	2976 ± 170	43.56 ± 0.09	0.0263	Sy1[a]
30	72	IRAS 04124-0803	168 ± 12	423 ± 39	...	43.86 ± 0.08	0.0379	Sy1
31	73	3C 111.0	61 ± 7	...	...	44.82 ± 0.04	0.0485	Sy1/RL
32	75	1H 0419-577	...	106 ± 21	...	44.66 ± 0.06	0.1040	Sy1
33	77	3C 120	203 ± 20	497 ± 68	1468 ± 85	44.41 ± 0.04	0.0330	Sy1/RL
34	78	MCG -02-12-050	...	...	682 ± 111	43.75 ± 0.08	0.0364	Sy1.2
35	79	UGC 03142	...	...	1581 ± 79	43.51 ± 0.07	0.0217	Sy1
36	80	2MASX J04440903+2813003	90 ± 18	...	1427 ± 214	43.25 ± 0.04	0.0113	Sy2
37	83	CGCG 420-015	173 ± 7	471 ± 22	624 ± 32	43.85 ± 0.07	0.0294	Sy2
38	84	ESO 033-G 002	163 ± 7	387 ± 15	646 ± 120	43.23 ± 0.07	0.0181	Sy2
39	85	LEDA 097068	218 ± 13	581 ± 27	852 ± 53	44.36 ± 0.07	0.0577	Sy1
40	87	IRAS 05078+1626	166 ± 14	748 ± 46	957 ± 41	43.78 ± 0.04	0.0179	Sy1.5
41	89	Ark 120	252 ± 18	253 ± 33	...	44.17 ± 0.04	0.0323	Sy1
42	90	ESO 362-18	166 ± 31	366 ± 36	1277 ± 88	43.29 ± 0.04	0.0125	Sy1.5
43	93	PKS 0521-36	97 ± 0.1	216 ± 20	...	44.32 ± 0.06	0.0553	Blazar/BL Lac
44	109	NGC 2110	300 ± 19	566 ± 30	4594 ± 47	43.63 ± 0.04	0.0078	Sy2
45	110	MCG +08-11-011	340 ± 18	1283 ± 35	2377 ± 62	43.91 ± 0.04	0.0205	Sy1.5
46	112	2MASX J05580206-3820043	348 ± 15	536 ± 17	...	43.96 ± 0.04	0.0339	Sy1
47	113	IRAS 05589+2828	201 ± 7	454 ± 33	955 ± 79	44.17 ± 0.05	0.0330	Sy1
48	114	ESO 005-G 004	537 ± 46	520 ± 46	8501 ± 407	42.54 ± 0.05	0.0062	Sy2
49	115	Mrk 3	321 ± 5	1890 ± 49	2939 ± 282	43.76 ± 0.04	0.0135	Sy2
50	118	ESO 490-IG026	...	...	1409 ± 41	43.72 ± 0.04	0.0248	Sy1.2
51	121	Mrk 6	180 ± 8	522 ± 23	920 ± 55	43.73 ± 0.04	0.0188	Sy1.5
52	122	UGC 03601	...	...	385 ± 23	43.41 ± 0.06	0.0171	Sy1.5
53	125	Mrk 79	276 ± 6	611 ± 38	1358 ± 64	43.68 ± 0.04	0.0222	Sy1.2
54	127	Mrk 10	...	...	918 ± 44	43.73 ± 0.07	0.0293	Sy1.2
55	131	2MASX J07595347+2323241	105 ± 22	...	2820 ± 120	43.86 ± 0.07	0.0292	Sy2

Table 2.1: *Continued.*

Serial No. (1)	BAT No. (2)	Object name (3)	$Flux_{09}$ (mJy) (4)	$Flux_{18}$ (mJy) (5)	$Flux_{90}$ (mJy) (6)	log L_X (erg s^{-1}) (7)	Redshift (8)	Type (9)
56	132	IC 0486	...	...	1213 ± 61	43.67 ± 0.09	0.0269	Sy1
57	133	Phoenix Galaxy	274 ± 19	1310 ± 6	1196 ± 62	43.29 ± 0.04	0.0135	Sy2
58	134	FAIRALL 0272	...	...	791 ± 58	43.58 ± 0.07	0.0218	Sy2
59	138	FAIRALL 1146	157 ± 14	441 ± 30	1059 ± 152	43.82 ± 0.06	0.0316	Sy1.5
60	145	IRAS 09149-6206	407 ± 7	792 ± 17	1735 ± 48	44.33 ± 0.06	0.0573	Sy1
61	146	Mrk 704	256 ± 30	469 ± 20	...	43.79 ± 0.06	0.0292	Sy1.5
62	148	MCG -01-24-012	...	263 ± 44	...	43.55 ± 0.06	0.0196	Sy2
63	149	MCG +04-22-042	78 ± 15	178 ± 47	...	43.97 ± 0.05	0.0323	Sy1.2
64	152	Mrk 705	99 ± 21	213 ± 44	926 ± 84	43.56 ± 0.08	0.0291	Sy1.2
65	153	NGC 2992	299 ± 49	827 ± 54	9220 ± 194	42.76 ± 0.05	0.0077	Sy2
66	154	MCG -05-23-016	384 ± 14	1391 ± 21	1277 ± 84	43.48 ± 0.04	0.0085	Sy2
67	158	NGC 3081	167 ± 13	699 ± 41	2364 ± 131	43.12 ± 0.04	0.0080	Sy2
68	159	NGC 3079	...	1561 ± 83	59311 ± 1906	41.97 ± 0.05	0.0037	Sy2/CT
69	163	ESO 374-G 044	...	307 ± 74	...	43.66 ± 0.08	0.0284	Sy2
70	164	NGC 3227	444 ± 71	1128 ± 44	10596 ± 535	42.63 ± 0.04	0.0039	Sy1.5
71	165	NGC 3281	415 ± 9	1509 ± 29	6011 ± 458	43.31 ± 0.04	0.0107	Sy2/CT
72	167	LEDA 093974	96 ± 23	256 ± 68	941 ± 26	43.62 ± 0.07	0.0239	Sy2
73	171	NGC 3516	262 ± 20	651 ± 16	1317 ± 83	43.29 ± 0.04	0.0088	Sy1.5
74	179	NGC 3783	502 ± 10	1530 ± 41	2716 ± 108	43.56 ± 0.04	0.0097	Sy1
75	185	NGC 3998	98 ± 22	133 ± 20	451 ± 16	41.87 ± 0.06	0.0035	LINER[a]
76	187	LEDA 38038	166 ± 8	614 ± 41	1631 ± 123	43.83 ± 0.06	0.0280	Sy2
77	188	NGC 4051	346 ± 30	885 ± 42	4557 ± 254	41.66 ± 0.04	0.0023	Sy1.5
78	189	ARK 347	...	102 ± 56	...	43.59 ± 0.06	0.0224	Sy2
79	190	NGC 4102	1082 ± 49	3287 ± 74	54050 ± 2235	41.61 ± 0.06	0.0028	LINER/CT
80	191	Mrk 198	...	...	584 ± 97	43.40 ± 0.08	0.0242	Sy2
81	192	NGC 4138	...	...	2161 ± 74	41.82 ± 0.05	0.0030	Sy1.9
82	193	NGC 4151	1032 ± 19	3629 ± 72	4594 ± 126	43.13 ± 0.04	0.0033	Sy1.5
83	195	NGC 4235	...	...	401 ± 50	42.49 ± 0.09	0.0080	Sy1
84	196	Mrk 766	220 ± 13	859 ± 20	3312 ± 190	42.91 ± 0.05	0.0129	Sy1.5
85	197	M 106	387 ± 47	449 ± 72	...	41.10 ± 0.09	0.0015	LINER
86	200	NGC 4388	462 ± 21	1589 ± 31	10349 ± 637	43.69 ± 0.04	0.0084	Sy2
87	204	3C 273	276 ± 3	454 ± 7	814 ± 56	46.28 ± 0.04	0.1583	Blazar/FSRQ
88	206	NGC 4507	510 ± 4	1163 ± 31	4370 ± 117	43.80 ± 0.04	0.0118	Sy2
89	207	ESO 506-G027	114 ± 19	207 ± 1	613 ± 73	44.24 ± 0.04	0.0250	Sy2
90	209	NGC 4593	...	569 ± 5	...	43.20 ± 0.04	0.0090	Sy1
91	211	WKK 1263	...	170 ± 24	769 ± 29	43.68 ± 0.08	0.0244	Sy2[a]
92	215	3C 279	265 ± 57	626 ± 2	2024 ± 117	46.46 ± 0.06	0.5362	Blazar/FSRQ
93	221	NGC 4945	8811 ± 325	9945 ± 495	...	42.38 ± 0.04	0.0019	LINER[b]/CT
94	222	ESO 323-077	472 ± 3	902 ± 17	6945 ± 236	43.33 ± 0.06	0.0150	Sy1.2
95	223	NGC 4992	59 ± 10	...	352 ± 42	43.89 ± 0.04	0.0251	Sy2[c]
96	225	MCG -03-34-064	453 ± 11	1873 ± 45	4634 ± 106	43.23 ± 0.06	0.0165	Sy1.8
97	226	Cen A	10191 ± 2305	13148 ± 1049	102187 ± 12824	42.78 ± 0.04	0.0018	Sy2/RL
98	228	MCG -06-30-015	280 ± 32	591 ± 11	1035 ± 119	42.97 ± 0.04	0.0077	Sy1.2
99	229	NGC 5252	...	...	415 ± 120	43.94 ± 0.04	0.0230	Sy1.9
100	230	4U 1344-60	207 ± 9	556 ± 28	...	43.50 ± 0.04	0.0129	Sy1.5
101	231	IC 4329A	769 ± 12	1790 ± 34	1785 ± 210	44.23 ± 0.04	0.0160	Sy1.2
102	233	Mrk 279	141 ± 9	388 ± 28	...	43.99 ± 0.04	0.0304	Sy1.5
103	235	Circinus Galaxy	13910 ± 173	41447 ± 265	253567 ± 64752	42.03 ± 0.04	0.0014	Sy2[d]/CT
104	236	NGC 5506	823 ± 27	2240 ± 69	8413 ± 302	43.29 ± 0.04	0.0062	Sy1.9
105	237	NGC 5548	157 ± 5	409 ± 40	1073 ± 237	43.68 ± 0.04	0.0172	Sy1.5
106	238	ESO 511-G030	...	...	847 ± 150	43.67 ± 0.06	0.0224	Sy1
107	239	SBS 1419+480	46 ± 6	189 ± 13	...	44.34 ± 0.07	0.0723	Sy1.5
108	241	Mrk 817	188 ± 10	669 ± 27	1575 ± 60	43.64 ± 0.07	0.0314	Sy1.5
109	242	NGC 5728	176 ± 21	418 ± 31	11383 ± 420	43.26 ± 0.04	0.0093	Sy2/CT
110	246	WKK 4438	94 ± 15	266 ± 12	1105 ± 86	43.01 ± 0.10	0.0160	Sy1

Table 2.1: *Continued.*

Serial No. (1)	BAT No. (2)	Object name (3)	$Flux_{09}$ (mJy) (4)	$Flux_{18}$ (mJy) (5)	$Flux_{90}$ (mJy) (6)	log L_X (erg s^{-1}) (7)	Redshift (8)	Type (9)
111	247	IC 4518A	243 ± 27	677 ± 22	7039 ± 243	43.24 ± 0.06	0.0163	Sy2
112	248	Mrk 841	126 ± 13	372 ± 25	...	43.89 ± 0.07	0.0364	Sy1
113	254	NGC 5899	...	...	4683 ± 184	42.50 ± 0.08	0.0086	Sy2
114	257	MCG -01-40-001	...	...	2304 ± 108	43.59 ± 0.06	0.0227	Sy2
115	258	Mrk 290	...	151 ± 13	...	43.65 ± 0.06	0.0296	Sy1
116	264	NGC 5995	325 ± 19	671 ± 4	4580 ± 329	43.76 ± 0.06	0.0252	Sy2
117	277	Mrk 1498	67 ± 12	214 ± 21	...	44.42 ± 0.04	0.0547	Sy1.9
118	285	3C 345	102 ± 7	353 ± 8	...	46.37 ± 0.08	0.5928	Blazar/FSRQ
119	292	NGC 6240	350 ± 15	1489 ± 12	23179 ± 433	43.94 ± 0.04	0.0245	Sy2/CT
120	295	1RXS J165605.6-520345	135 ± 13	248 ± 24	1109 ± 84	44.35 ± 0.08	0.0540	Sy1.2
121	317	NGC 6300	277 ± 24	1336 ± 97	14928 ± 1066	42.45 ± 0.04	0.0037	Sy2
122	360	[HB89] 1821+643	131 ± 4	326 ± 10	635 ± 34	45.49 ± 0.08	0.2970	Sy1/RIM
123	370	3C 382	120 ± 12	...	...	44.75 ± 0.04	0.0579	Sy1/RL
124	372	FAIRALL 0049	411 ± 20	920 ± 59	2619 ± 180	43.38 ± 0.07	0.0202	Sy2
125	374	ESO 103-035	300 ± 25	1446 ± 12	1227 ± 77	43.60 ± 0.04	0.0133	Sy2
126	377	3C 390.3	90 ± 10	242 ± 17	...	44.84 ± 0.04	0.0561	Sy1/RL
127	378	Fairall 0051	301 ± 7	697 ± 62	1705 ± 180	43.27 ± 0.06	0.0142	Sy1
128	401	ESO 141-G 055	150 ± 5	233 ± 38	...	44.14 ± 0.05	0.0360	Sy1
129	404	2MASX J19301380+3410495	130 ± 12	254 ± 23	...	44.41 ± 0.06	0.0629	Sy1
130	405	2MASS J19334715+3254259	101 ± 10	269 ± 8	...	44.19 ± 0.08	0.0578	Sy1.2
131	407	NGC 6814	...	258 ± 29	6954 ± 350	42.63 ± 0.04	0.0052	Sy1.5
132	415	Cygnus A (3C 405)	...	418 ± 17	2455 ± 78	44.89 ± 0.04	0.0561	Sy2/RL
133	418	NGC 6860	155 ± 13	357 ± 61	1369 ± 73	43.46 ± 0.05	0.0149	Sy1
134	420	MCG +04-48-002	388 ± 11	538 ± 16	12160 ± 289	43.53 ± 0.04	0.0139	Sy2
135	425	4C +74.26	147 ± 6	175 ± 9	...	45.04 ± 0.04	0.1040	Sy1/RL
136	426	RX J2044.0+2833	...	199 ± 46	...	44.10 ± 0.07	0.0500	Sy1
137	427	Mrk 509	247 ± 18	499 ± 17	...	44.35 ± 0.04	0.0344	Sy1.2
138	428	IC 5063	...	2246 ± 26	3821 ± 141	43.35 ± 0.04	0.0114	Sy2
139	429	2MASX J21140128+8204483	71 ± 5	105 ± 32	...	44.77 ± 0.05	0.0840	Sy1/RL
140	434	4C 50.55	...	188 ± 21	...	44.15 ± 0.04	0.0200	Sy1[a]/RL
141	435	SWIFT J212745.58+565635.6	211 ± 15	435 ± 17	...	43.22 ± 0.04	0.0147	Sy1
142	441	1RXS J213623.1-622400	...	142 ± 11	...	44.43 ± 0.06	0.0588	Sy1
143	445	Mrk 520	146 ± 12	320 ± 11	5040 ± 100	43.70 ± 0.07	0.0266	Sy1.9
144	446	NGC 7172	316 ± 17	424 ± 44	8087 ± 218	43.44 ± 0.04	0.0087	Sy2
145	447	BL Lac	247 ± 36	319 ± 34	937 ± 122	44.62 ± 0.05	0.0686	Blazar/BL Lac
146	449	NGC 7213	360 ± 35	...	2943 ± 146	42.59 ± 0.05	0.0058	Sy1.5
147	451	3C 445	141 ± 13	358 ± 6	...	44.44 ± 0.05	0.0562	Sy1.5/RL
148	452	MCG +02-57-002	...	...	575 ± 39	43.54 ± 0.09	0.0290	Sy1.5
149	455	NGC 7314	...	304 ± 58	4499 ± 258	42.33 ± 0.05	0.0048	Sy1.9
150	456	NGC 7319	88 ± 14	158 ± 8	576 ± 39	43.60 ± 0.05	0.0225	Sy2
151	457	Mrk 915	...	482 ± 284	...	43.76 ± 0.06	0.0241	Sy1
152	460	3C 454.3	...	498 ± 6	...	47.37 ± 0.04	0.8590	Blazar/FSRQ
153	463	UGC 12282	...	...	1284 ± 124	43.16 ± 0.08	0.0170	Sy1.9
154	465	NGC 7469	767 ± 17	2692 ± 60	27694 ± 1738	43.55 ± 0.05	0.0163	Sy1.2
155	466	Mrk 926	60 ± 3	214 ± 36	647 ± 119	44.65 ± 0.04	0.0469	Sy1.5
156	467	NGC 7582	1368 ± 90	3287 ± 199	60906 ± 6037	42.63 ± 0.04	0.0052	Sy2
157	468	NGC 7603	295 ± 11	321 ± 12	1340 ± 104	43.91 ± 0.04	0.0295	Sy1.5
158	473	LCRS B232242.2-384320	...	...	654 ± 80	43.79 ± 0.08	0.0359	Sy1

Col. (1): serial number. Col. (2): Object number in the 22-month *Swift*/BAT hard X-ray survey catalog (Tueller et al., 2010). Col. (3): Object name. Col. (4)(5)(6): The flux and error in 9, 18, and 90 μm taken from *AKARI*/PSC in units of mJy. Col. (7): The logarithmic luminosity and error in hard X-ray band (14-195 keV) taken from Tueller et al. (2010), in units of erg s^{-1}. Col. (8): Redshift. Col. (9): Optical AGN type taken from Tueller et al. (2010) or from other literature sources as follows: [a]Véron-Cetty & Véron (2010); [b]Moorwood et al. (1996); [c]Bodaghee et al. (2007); [d]Matt et al. (2000)

Table 2.2: Summary of cross-identifications

AKARI detector		Source type				Total	Excluded source
		Sy1	Sy2	LINER	Blazar		
(1)	(2)	(3)	(4)	(5)	(6)	(7)	(8)
IRC 9 (μm)	detection	59	43	4	5	111	2
	non-detection	66	56	2	21	145	10
IRC 18 (μm)	detection	67	52	4	6	129	5
	non-detection	57	47	2	20	126	8
FIS 90 (μm)	detection	48	60	2	3	113	3
	non-detection	76	41	4	22	143	9

Col.(1): The *AKARI* instruments and the center bands. Col.(3): The number of source detection and non-detection of Seyfert 1 type AGN including Seyfert 1.2 and 1.5. Col.(4): The number of source detection and non-detection of Seyfert 2 type AGN including Seyfert 1.8 and 1.9. Col.(5): The number of source detection and non-detection of LINERs. Col.(6): The number of source detection and non-detection of Blazars. Col.(7): The total number of source detection and non-detection, i.e., sum of columns (3) through (6). Col.(8): The number of excluded sources, which are confused or confusing sources as defined by Tueller et al. (2010).

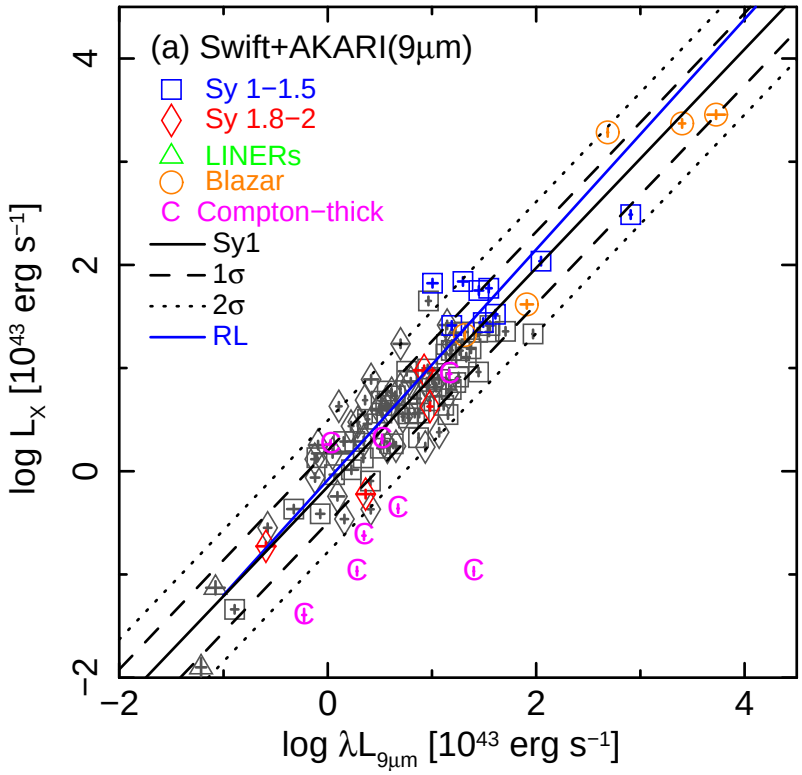

Figure 2.4: Logarithmic luminosity correlations between the *AKARI*and *Swift*/BAT. The ordinates are hard X-ray (14-195 keV) luminosities, and the abscissas are IR luminosities at (a) 9 μm, (b) 18 μm, and (c) 90 μm. Symbols indicates the AGN types (Seyfert 1, Seyfert 2, LINERs, and Blazars). Color symbols in the plots are radio-loud AGN and blazars. Gray symbols are radio-quiet AGN. Magenta character "C" indicates Compton thick sources. The black and blue solid lines are the correlation fitted to only Seyfert 1s ("Sy1") and "RL", by using the liner regression algorithm, respectively. The dashed and dotted lines show the standard deviation of the correlation; 1σ and 2σ.

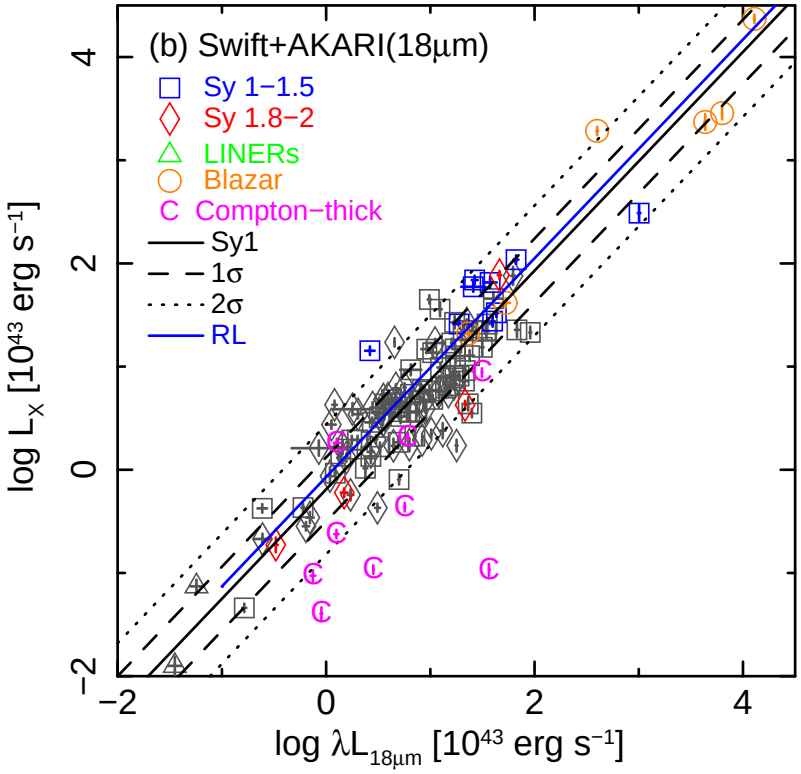

Figure 2.4: *Continued.* (b) 18 μm.

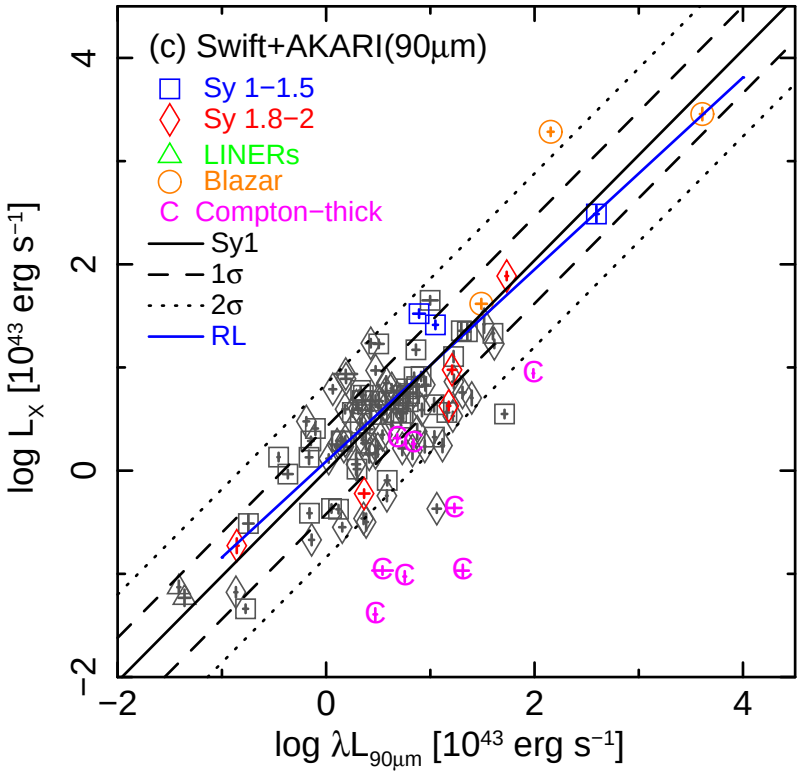

Figure 2.4: *Continued.* (c) 90 μm.

Table 2.3: Summary of the fitting results

AKARI detector	Subsample	N	ρ	$\rho_{\cdot z}$	a	b	$\bar{r}$	σ_r
(1)	(2)	(3)	(4)	(5)	(6)	(7)	(8)	(9)
IRC 9 (μm)	All	111	0.85	0.79	0.22 ± 0.05	0.88 ± 0.04	0.14	0.42
	All, ex CT	103	0.88	0.87	0.13 ± 0.04	0.94 ± 0.04	0.08	0.32
	Sy1	59	0.87	0.85	0.15 ± 0.05	0.94 ± 0.06	0.09	0.30
	Sy1, ex RL	50	0.87	0.69	0.15 ± 0.05	0.99 ± 0.07	0.14	0.26
	Sy2	43	0.58	0.06	0.23 ± 0.08	0.84 ± 0.07	0.17	0.53
	Sy2, ex CT	37	0.70	0.44	0.11 ± 0.07	0.91 ± 0.08	0.06	0.35
	CT	8	0.31	-0.14	0.81 ± 0.28	0.81 ± 0.24	0.87	0.81
	RL	13	0.81	0.89	0.09 ± 0.15	0.90 ± 0.11	-0.14	0.39
	Blazar	5	1.00	0.87	0.11 ± 0.23	0.96 ± 0.10	-0.002	0.36
	RL + Blazar	18	0.86	0.88	0.05 ± 0.14	0.95 ± 0.07	-0.03	0.37
IRC 18 (μm)	All	129	0.84	0.77	0.27 ± 0.05	0.89 ± 0.04	0.19	0.43
	All, exc CT	120	0.86	0.84	0.18 ± 0.04	0.94 ± 0.03	0.14	0.34
	Sy1	67	0.84	0.75	0.18 ± 0.06	0.94 ± 0.06	0.13	0.31
	Sy1, ex RL	58	0.84	0.68	0.20 ± 0.06	0.97 ± 0.07	0.17	0.28
	Sy2	52	0.62	0.31	0.31 ± 0.07	0.86 ± 0.06	0.27	0.53
	Sy2, ex CT	45	0.72	0.57	0.18 ± 0.06	0.94 ± 0.06	0.17	0.38
	CT	9	0.55	-0.12	0.93 ± 0.26	0.86 ± 0.15	1.00	0.81
	RL	13	0.90	0.80	0.07 ± 0.18	0.94 ± 0.11	-0.02	0.41
	Blazar	6	1.00	0.75	0.04 ± 0.16	0.98 ± 0.07	-0.03	0.38
	RL + Blazar	19	0.93	0.84	0.04 ± 0.15	0.97 ± 0.07	-0.02	0.39
FIS 90 (μm)	All	113	0.57	0.48	0.21 ± 0.06	0.88 ± 0.06	0.15	0.58
	All, ex CT	106	0.65	0.64	0.10 ± 0.05	0.94 ± 0.06	-0.08	0.48
	Sy1	48	0.77	0.66	0.002 ± 0.074	0.98 ± 0.08	-0.01	0.39
	Sy1, ex RL	45	0.75	0.37	0.007 ± 0.079	1.01 ± 0.11	0.01	0.39
	Sy2	60	0.33	0.06	0.32 ± 0.08	0.91 ± 0.06	0.29	0.63
	Sy2, ex CT	53	0.46	0.25	0.17 ± 0.07	0.94 ± 0.07	0.18	0.53
	CT	8	0.50	-0.26	1.24 ± 0.16	0.65 ± 0.05	1.32	0.69
	RL	8	0.79	0.83	0.09 ± 0.18	0.93 ± 0.09	0.02	0.42
	Blazar	3	1.00	1.00	–	–	-0.37	0.67
	RL + Blazar	11	0.91	0.81	0.08 ± 0.18	0.89 ± 0.11	-0.08	0.50

Col.(1): The *AKARI* data used for the correlation studies. Col.(2): Subsamples used for fitting (See Sec. 2.3.2). Col. (3): number of sources in each subsample. Col. (4): Spearman's Rank correlation coefficient (ρ). Col. (5); partial correlation coefficient ($\rho_{\cdot z}$) estimated excluding the effect of the redshift. Col. (6): regression slope and its 1-σ uncertainty computed with the algorithm of OLS bisector for Equation (2.1). Col. (7): same as column (6) but for regression intercept and its 1-σ uncertainty. Col. (8) (9): average and standard deviation of the luminosity ratio $r = \log(L_{\rm IR}/L_{\rm X})$.

Chapter 3

Infrared variability of AGN

3.1 Introduction

Cross-correlating the 22-month hard X-ray survey with the *AKARI* all-sky survey, I find a strong correlation between the infrared (IR; 9, 18, and 90 μm) and hard X-ray (14–195 keV) luminosities of the AGN. On the other hand, a few radio-loud sources (radio galaxies and blazars) show systematic deviations toward higher X-ray luminosities in the correlations as compared to radio-quiet sources. One possible explanation of this deviation (i.e., excess X-rays) is the contribution of jets to the hard X-ray emission. Observations of flux variability can be useful for isolating the jet contribution, because strong and rapid fluctuations are characteristic of beamed jet emission. Useful hard X-ray variability data are not yet available, but such data have recently become available in the mid-infrared. Furthermore, mid-infrared variations can also potentially constrain the geometry of the dusty torus by measuring the response of the torus to changes in the AGN continuum. Therefore, I study mid-infrared variability of AGN systematically in this chapter.

AKARI scanned the whole sky twice or more during the 16 months of the cryogenic mission phase. I first tried to estimate the time variations by looking into each scan of data, which are separated by half a year. However, it turned out that the readout noise of IRC was relatively high compared to the intrinsic variations of most of the AGN. Thus it was difficult to obtain meaningful constraint on time variations with the *AKARI* data. On the other hand, the Wide-field Infrared Survey Explorer (*WISE*; Wright et al., 2010), which was launched in 2009 about four years after *AKARI* accomplished all-sky surveys with high sensitivity in several mid-infrared bands (particularly relevant for my work are the 12 and 22 μm bands). I could quickly check whether sources were variable or not by the variability flag in the *WISE* catalog, but only a few blazars were flagged with high reliability. Therefore, I decided to study a long-term variation at mid-IR bands by combining the two all-sky survey catalogs, the *AKARI* Point Source Catalogues and the *WISE* All-Sky Source Catalog.

3.2 *WISE* All-Sky Source Catalog

3.2.1 The Wide-field Infrared Survey Explorer

WISE was launched on 2009 December 14 as one of the National Aeronautics and Space Administration (NASA) Medium Class Explorer mission. The main aim of the mission is to survey the whole sky at mid-IR band with much higher sensitivity than previous surveyors.

The *WISE* flight system is 285 cm tall, 200 cm wide, and 173 cm deep. It has a mass of 661 kg. *WISE* conducted its survey using a 40 cm cryogenically-cooled telescope equipped with a camera containing four mid-IR focal plane array detectors, which have the same 47×47 arcmin field-of-view on the sky. Surveys started on January 7, 2010 with full 4-band (W1, W2, W3, and W4 centered at 3.4, 4.6, 12, and 22 μm, respectively), and the cryogenic survey operations continued until August 6, 2010 till the solid hydrogen in the outer cryogenic tank was exhausted. *WISE* surveyed the sky approximately 1.2 times during the full cryogenic phase. The azimuthally averaged point spread function (PSF) of *WISE* has FWHMs of 6.″1, 6.″4, 6.″5, and 12.″0 in W1–4, respectively. In the geometric limit without diffraction the estimated FWHM is roughly 5.″5. The 95% of the sky has been covered at least 10.81, 10.75, 9.78 and 9.90 times in W1-4, which is sometimes referred to as a depth of observations. The estimated *WISE* sensitivities are 0.068, 0.098, 0.86, and 5.4 mJy (5σ), respectively.

In the release of the *WISE* all-sky survey data, such database is also included that the solid hydrogen cryogen in the inner tank was already sublimated. In the 3-Band Cryo phase, *WISE* continued to survey another 30% of the sky using W1, W2, and W3 bands detectors till September 29, 2010. I do not use this database in the thesis because the database is not reliable as the *WISE* All-Sky Source Catalog. This contains spurious detections (e.g., image artifacts, noise excursions, transient events such as cosmic rays, satellite trails, and hot pixels). Therefore, I use the *WISE* All-Sky Source Catalog for cross matching with the *AKARI* Point Source Catalogue, which summarize the results of full 4-band cryogenic survey.

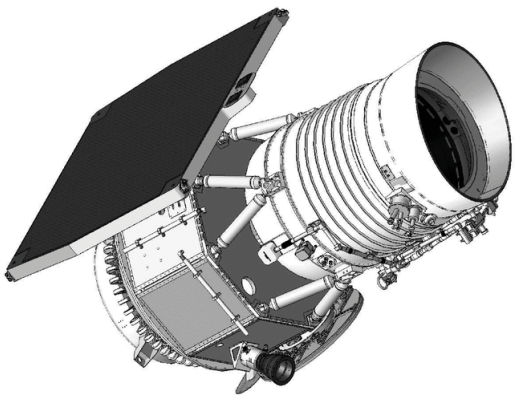

Figure 3.1: The *WISE* flight system in survey configuration with cover off.

3.2.2 The *WISE* All-Sky Source Catalog

The *WISE* All-Sky Source Catalog contains information of astrometry and photometry for 563,921,584 objects detected on the Atlas Intensity Images. The catalog includes source information of positions, magnitudes, and astrometric/photometric uncertainties, and flags indicating reliability and quality of the source characterizations. I concentrate on two *WISE* bands (W3 and W4 centered at 12 and 22 μm, respectively) throughout in this thesis in order to compare fluxes observed at the near bands of *AKARI* (9 and 18 μm).

There are two types of photometry data in this catalog, the profile-fit photometry and aperture measurement[1]. Since the majority of sources detected by *WISE* are spatially unresolved, the profile-fitted flux represents the best estimate in most cases, which handles PSF variations and masked pixels in an optimal fashion, and extends the dynamic range for bright sources well into the saturated regime. On the other hand, for extended sources, which is indicated by the elevated chi-squared value, an aperture flux should be used instead. A simple aperture system employs circular apertures to characterize the integrated flux and "curve-of-growth" of point sources as measured in the co-added images. Here, "curve-of-growth" indicates a relation between the aperture radius and the ratio of measured flux / encircled flux. Systematic errors in *WISE* photometry arise predominantly from (1) stellar confusion, (2) data corruption (e.g., saturation), and (3) calibration and zero point magnitude errors. Because the aperture photometry is most influenced by these effects of source crowding and saturation[2], I use the profile-fit photometry throughout in this thesis. For the purpose of cross-check, I compare magnitudes between these two types of *WISE* photometry for cross-identified sources in Section 3.3.

The root mean square error of positions in *WISE* catalog with respect to the Two Micron All Sky Survey (2MASS) catalog positions is less than $0.''5$, for sources with signal-to-noise ratio > 20 in at least one *WISE* band[3]. Sources are flagged with *ext_flg* $= 0-5$[4] in the catalog, which indicate whether or not the morphology of a source is consistent with the *WISE* PSF in any band, or whether the source is affected by or superimposed on a known extended object from the 2MASS Extended Source Catalog (XSC). If *ext_flg*$= 0$, the source shape is consistent with a point source and the source is not affected by or superimposed on a 2MASS XSC source. But almost 68% of *Swift*/BAT-*AKARI* selected sources are flagged as *ext_flg* $= 5$, which indicate that the profile-fit photometry goodness-of-fit, χ^2, is > 3.0 in one or more bands, and the source position falls within $5''$ of a 2MASS XSC source. In Section 3.3, I show the limits of cross-identification of sources to eliminate extended sources without *ext_flg*.

Each source has a variability flag, *var_flg*, which is related to the probability of flux variation calculated by the standard deviation of the single exposure flux measurements and the band-to-band flux correlation significance. The flag has values of 0 or 1-9, latter of which indicate increasing likelihood of variability. A *var_flg* $= 0$ in a band indicates insufficient or inadequate data to make a variability determination. Hoffman et al. (2012) describe the derivation of this

[1] http://wise2.ipac.caltech.edu/docs/release/allsky/expsup/sec4_4c.html
[2] http://wise2.ipac.caltech.edu/docs/release/allsky/expsup/sec6_3c.html
[3] http://wise2.ipac.caltech.edu/docs/release/allsky/expsup/sec6_4.html
[4] http://wise2.ipac.caltech.edu/docs/release/allsky/expsup/sec4_4c.html

flag for sources in the *WISE* Preliminary Data Release Source Catalog[5] covering 57% of the sky. In this catalog, we can exclude insufficient or inadequate sources by the flag (in this case, *var_flg* = 0). However, in the *WISE* All-Sky Source Catalog, sources often flagged as *var_flag* $\neq$ 0 despite unreliability of data due to saturation, poor PSF fitting, and contamination. Also, if I apply these strict limitations (no extension, no saturation, and no contamination) to *Swift*/BAT-*AKARI* selected sources with a high value (*var_flg* = 9 in each band), I get only a few blazars as variable sources in *WISE* All-Sky Source Catalog. Therefore I decided to search for variable sources by combining *AKARI* and *WISE* catalogs. in Section 3.3 and 3.4.

The photometric data of *WISE* are given in Vega magnitude computed with the isophotal fluxes in units of Jy, as follows:

$$m = -2.5 \times \log_{10} S_\nu / F_\nu(\mathrm{iso}), \tag{3.1}$$

where m is Vega magnitude, S_ν is observed fluxes in units of Jy, and F_ν(iso) is isophotal fluxes. The isophotal fluxes are constant, and are F_ν(iso) = 31.674 and 8.363 Jy in 12 and 22 μm, respectively (Jarrett et al., 2011). I convert the Vega magnitudes in the *WISE* catalog to Jy in order to compare *AKARI* fluxes in Section 3.4.

3.3 Cross-identification of sources

Because the variability flag (*var_flg*) in *WISE* All-Sky Source Catalog does not reflect to unreliability of sources, I select sources using by other limitations. In what follows, I explain the method of cross-identification in the *WISE* All-Sky Catalog for 158 *Swift*/BAT-*AKARI* AGN. Some conditions are based on to the filters for generating of variability flag, *var_flg*, in the *WISE* Preliminary Data Release Source Catalog (Hoffman et al., 2012). In this cross-identification, I do not use *var_flg* or *ext_flg* in the *WISE* All-Sky Source Catalog.

1. Search radius
   I search *WISE* All-Sky Catalog using the *NASA*/Infrared Processing and Analysis Center (IPAC) Infrared Science Archive (IRSA)[6] for the *Swift*/BAT-*AKARI* AGN. Here I adopt a search radius of 2″centered at the position of the optical counterpart listed in the BAT catalog. This search radius is comparable to position accuracy of *WISE* at 3σ level.

2. Signal-to-noise ratio
   The catalog contains a photometric quality flag, *ph_qual*, for each band. This provides the quality of the profile-fit photometry measurement derived from the signal-to-noise ratio. I use only sources confirmed and described by *ph_qual* = *A*, indicating a flux signal-to-noise ratio > 10.

3. Reduced chi-square
   High chi-square values usually indicate confusion with nearby objects, or that the source is

[5] `http://wise2.ipac.caltech.edu/docs/release/prelim/`
[6] `http://irsa.ipac.caltech.edu/index.html`

extended, both of which lead to measurement inaccuracy. I cross-identified only the *WISE* sources satisfying chi-square < 5.0 in each band in order to minimize the source confusion.

4. Number of PSF components
   This indicates a number of PSF used simultaneously to fit the source image. It includes the source itself, so the minimum value of nb is "1". The number of nb becomes greater than "1" when the source is fitted concurrently with other nearby sources (passive deblending), or when a single source is split into two components during the fitting process (active deblending). I set the limit as $nb < 3$, which avoid to generate spurious flux sometimes be seen due to confusion.

5. Active deblending flag
   This flag indicates whether a single detection was split into multiple sources in the process of profile fitting, which indicates false variability produced by one or more close neighbors. In order to eliminate sources with active deblending, I set the limit as $na = 0$, which mean the source is not actively deblended.

6. Contamination and confusion flag
   This flag, taking one of the values of D (d), P (p), H (h), O (o), and 0, indicates that the photometry and/or position measurements of a source may be contaminated or biased due to proximity to an image for each band. In order to avoid contamination or confusion, I set the limit to $cc\_flg = 0$, which eliminate sources contaminated by a diffraction spike from a nearby bright star on the same image (cc_flg = d), a short-term latent image left by a bright source (cc_flg = p), a scattered light halo surrounding a nearby bright source (cc_flg = h), and an optical ghost image caused by a nearby bright source (cc_flg = o).

7. Saturation
   The observed saturation levels of *WISE* are 0.7 and 10 Jy for W3 and W4, respectively. The saturated pixel fractions listed in the catalog are flagged as $w1\text{-}4sat$ in each band. I eliminate sources, which satisfy both limits of higher fluxes exceeding the saturation level and high fraction of the saturated pixels ($w1\text{-}4sat \neq 0$).

As a result, among 111/129 AGN of the *Swift*/BAT-*AKARI* (9/18 μm bands) sample, 75 and 109 AGN are detected in W3 (68%) and W4 (84%) bands, respectively. I summarize the results of the source-identification in Table 3.1. For the purpose of investigating mid-IR variability for various classes of objects, I divide our sample into the following ten categories:

1. "All"
2. "Sy 1"
3. "Sy 2"
4. "LI"
5. "BL"
6. "RL 1"
7. "RL 2"

Table 3.1: Summary of the cross-identification

IR band	Source type							total
	Sy1	Sy2	LI	BL	RL1	RL2	CT	
(1)	(2)	(3)	(4)	(5)	(6)	(7)	(8)	(9)
9 μm	39	19	1	4	9	2	1	75
18 μm	52	35	1	6	8	3	4	109

Col. 1: Mid-infrared bands. Col. 2–8: Numbers of detected sources for (2) Seyfert 1 including Seyfert 1.2 and 1.5, (3) Seyfert 2 including Seyfert 1.8 and 1.9, (4) LINERs, (5) Blazars, (6) type 1 radio-loud AGN, (7) type 2 radio-loud AGN, and (8) Compton-thick AGN. Col. 9: Total numbers of detected sources, i.e., sum of columns (2) through (8).

8. "CT".

"All" contains all sources detected by *Swift*/BAT, *AKARI* and *WISE*. "Sy 1" contains type 1 radio-quiet AGN (Seyfert 1). "Sy 2" contains type 2 radio-quiet AGN (Seyfert 2). "LI" contains LINERs. "BL" combines FSRQs and BL Lacs. "RL 1" contains non-blazar type 1 radio-loud AGN. "RL 2" contains non-blazar type 2 radio-loud AGN such as narrow-line radio galaxies and low-power FR I radio galaxies. "CT" is defined as sources obscured by a gas column density $N_{\rm H} \geq 1.5 \times 10^{24}$ cm^{-2} as measured from X-ray spectroscopy. The median of absolute-delta fluxes, |(the profile-fit photometry) – (the aperture measurement)|, relative to fluxes of the profile-fit photometry, $\Delta {\rm F}_{\rm abs}$, are 2.10 % and 1.67% in W3 and W4 respectively. There are only 3/75 (4%) and 7/109(6%) sources with $\Delta {\rm F}_{\rm abs} > \pm$ 5% in W3 and W4, respectively.

3.4 Analysis and Results

3.4.1 Sample properties

Figure 3.2 shows distribution of the angular separation in right ascension and declination, ΔRa and ΔDec, between the positions of the cross-identified sources in *WISE* and *AKARI* catalog. If the angular separation was larger than their aperture sizes, the cross-identification could be wrong. I confirmed that distribution of the angular separation is consistent within the *AKARI* position uncertainty $\sigma \sim 3''$.

The median *AKARI* aperture radius (*mean_AB*) of cross-identified sources is $\approx 2.''60$, and $2.''68$ in 9 and 18 μm, respectively. The cross-identified sources with maximum *mean_AB* is NGC 3783 ($3.25''$) and NGC 7582 ($5.09''$) in 9 and 18 μm, respectively. This means that the cross-identified sources can be regarded as point sources with *AKARI*.

The median signal-to-noise ratio of *AKARI* was $\sim$143 and 105 in W3 and W4, respectively. The *WISE* signal-to-noise ratio exceeded 50 for all sources. These were consistent with the source selection criteria.

The median redshift of cross-identified sources is $\sim$0.0252, and 0.0222 in 9 and 18 μm, respectively. Only 4/75 (5%) and 8/109 (7%) sources have a redshift of $z > 0.1$. Thus all the

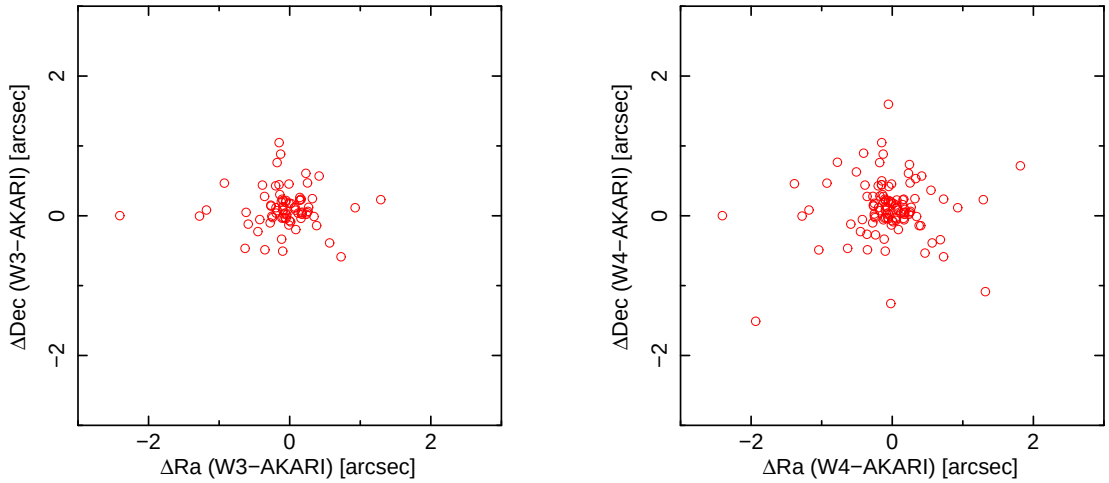

Figure 3.2: Distribution of the angular separation of the cross-identified sources in right ascension and declination, ΔRa and ΔDec, between the source positions in *WISE* and *AKARI* catalog. Numbers of cross-identified sources are 75 and 109 in W3 (12 μm) and W4 (22 μm), respectively. The abscissa is the differences of right ascension in *WISE–AKARI* positions. The ordinate is those of declination in *WISE–AKARI* positions. The left and right panels are for W3 (12 μm) and W4 (22 μm) bands, respectively.

cross-identified sources are effectively local AGN.

3.4.2 Relative flux variations

In order to compare the *AKARI* and *WISE* fluxes, I introduce relative flux ratios, ΔF^i, as follows:

$$\Delta F^i = \frac{F^i_W - F^i_A}{F^i_A}, \tag{3.2}$$

where F^i_W and F^i_A are observed fluxes of *WISE* and *AKARI*, respectively. Superscript i indicate the sequence number of the cross-identified sources. Because of the proximity of the central wavelengths, I compare fluxes of *WISE* 12 μm (W3) with *AKARI* 9 μm (S9W), and *WISE* 22 μm (W4) with *AKARI* 18 μm (L18W), respectively. As the central wave lengths of the observations, I use the isophotal wavelengths defined are 8.61, 11.56, 18.39, and 22.09 μm for S9W, W3, L18W, and W4, respectively (Ishihara et al., 2010; Wright et al., 2010). Because the observation bands of *AKARI* and *WISE* are slightly different, the difference must be corrected when we evaluate the relative flux ratios. I will explain the correction method in detail in the next subsection §3.4.3. Before that, I will see the properties of the relative flux ratios quantitatively.

I show frequency distribution of ΔF for sources detected in 4-band (71 sources) in Figure 3.3. I summarize statistics of the relative flux ratios in Table 3.2. The average value of the flux ratio of whole sample is 0.26 and 0.25, respectively. These offsets result from the differences of the observation wave bands between *AKARI* and *WISE*. The standard deviations of ΔF are also affected by the differences of the observation bands, because the slope of the SED varies from source to source.

The standard deviation of ΔF in Table 3.2 are calculated using the standard formula:

$$\sigma^2 = \frac{1}{N-1}\sum_{i=1}^{N}(\Delta F^i - \overline{\Delta F})^2, \tag{3.3}$$

where ΔF^i is a relative flux ratio of each source, $\overline{\Delta F}$ is an average of relative flux ratio of each subsample, and N shows the number of sources in the subsample. In addition, the error of standard deviations, σ_σ, are calculated with the formula below:

$$\sigma_\sigma = \frac{\sigma}{\sqrt{2(N-1)}}, \tag{3.4}$$

where σ shows the standard deviation of ΔF^i for each subsample calculated by Equation 3.3, N shows the number of sources in the subsample. This formula assumes the normal distribution of ΔF^i. In reality, it may not follow the normal distribution and I apply a different method to estimate the errors.

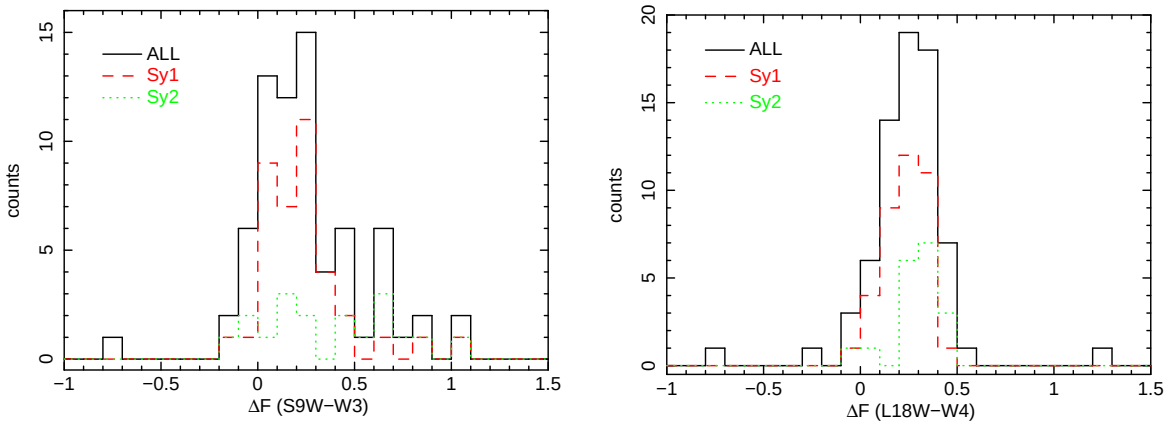

Figure 3.3: Distribution of the relative flux ratio, ΔF, between *AKARI* and *WISE*. Black-solid, red-dashed, and green dotted lines show the distribution of all sources (71 sources), Seyfert 1 (38 sources), and Seyfert 2 (18 sources), respectively. The abscissa show ΔF, and the ordinate show the number of sources. The left and right panels are for the S9W-W3 and L18W-W4, respectively. In both distribution, the bin size is set as $\Delta F = 0.1$.

3.4.3 Correction of the wave band differences

When we correct the wave band differences, we need to use SED of each source. I assume that the SED has a power-law form, which is a good approximation for AGN except for local emission/absorption structures. I use the *AKARI* and *WISE* data themselves to determine the power-law slope of the SED. Of course, because the source may be time variable, *AKARI* and *WISE* data may show systematic offset. However, the power-law slope of SED is considered to be rather insensitive to the time variation. This is because the observation bands are close and slope is basically determined with the *WISE* data due to much better statistics than the *AKARI* data. I show SEDs with the best-fit power-law model in Appendix B. I use the isophotal wavelengths described in the previous subsection as the center of the wave bands. I computed

Table 3.2: Statistics of ΔF

Type	N	ΔF			
		S9W-W3		L18W-W4	
		average	standard deviation	average	standard deviation
(1)	(2)	(3)	(4)	(5)	(6)
All	71	0.26	0.29 ± 0.02	0.25	0.21 ± 0.02
Sy1	38	0.24	0.22 ± 0.03	0.24	0.10 ± 0.01
Sy2	18	0.38	0.35 ± 0.06	0.29	0.13 ± 0.02
RL1	7	0.14	0.17 ± 0.05	0.16	0.27 ± 0.08
RL2	2	0.39	0.44 ± 0.31	0.32	0.20 ± 0.14
BL	4	-0.01	0.50 ± 0.20	0.21	0.84 ± 0.34

Col. 1: Object type. Col. 2: Number of sources in each subsamples. Col. 3 and 5: Average of ΔF in the S9W-W3 and L18W-W4 bands. Col. 4 and 6: Standard deviation of ΔF in the S9W-W3 and L18W-W4 bands.

the power-law slope of SEDs with errors. In this computation, I assumed that errors of isophotal wavelengths are small enough to ignore, as compared to errors on fluxes. Distribution of the slopes (α) and their errors are shown in Figure 3.4. I summarize statistics of the slopes in Table 3.3.

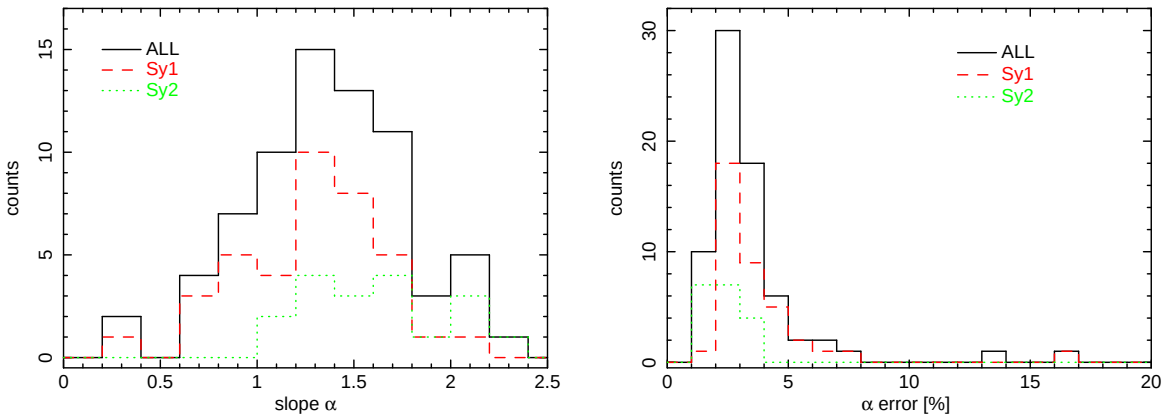

Figure 3.4: Distribution of the power-law slopes and their errors of SED with *AKARI* and *WISE* bands. Black-solid, red-dashed, and green-dotted lines shows slopes of all sources (71 sources), Seyfert 1 (38 sources), and Seyfert 2 (18 sources), respectively. Left figure shows the distribution of slopes. Right figure shows the fractional error of slopes in units of %.

Table 3.3: Statistics of slopes of infrared SEDs

Type	N	α	
		average	standard deviation
(1)	(2)	(3)	(4)
All	71	1.36	0.40
Sy1	38	1.28	0.37
Sy2	18	1.61	0.33
RL1	7	1.13	0.39
RL2	2	1.85	0.34
BL	4	1.19	0.45

Col. 1: Object type. Col. 2: Number of sources in each subsample. Col. 3: Average of the slope. Col. 4: Standard deviation of the slope.

Once the slope is determined, I can calculate the relative flux ratio (ΔF_0) by the slopes of SEDs as follows,

$$\Delta F_0^i = \frac{F_{\rm W}^i - F_{\rm A}^i}{F_{\rm A}^i} \tag{3.5}$$

$$= \left(\frac{\lambda_{\rm W}}{\lambda_{\rm A}}\right)^{\alpha^i} - 1, \tag{3.6}$$

$F_{\rm W}^i$ and $F_{\rm A}^i$ are fluxes observed by *WISE* and *AKARI*, respectively. $\lambda_{\rm W}$ and $\lambda_{\rm A}$ are isophotal wavelength of *WISE* and *AKARI*, respectively. α^i is the slope of the SED of each source. Also, the error of ΔF_0 ($\delta\Delta F_0$) is described as,

$$(\delta\Delta F_0)^2 = \left(\frac{\partial \Delta F_0}{\partial \alpha}\right)^2 \delta\alpha^2 \tag{3.7}$$

$$\delta\Delta F_0^i = \left(\frac{\lambda_{\rm W}}{\lambda_{\rm A}}\right)^{\alpha^i} \log\left(\frac{\lambda_{\rm W}}{\lambda_{\rm A}}\right) \times \delta\alpha^i, \tag{3.8}$$

$\delta\alpha^i$ is the error of α of each source. I show distribution of ΔF_0 and errors in Figure 3.5. I summarize statistics of ΔF_0 in Table 3.4.

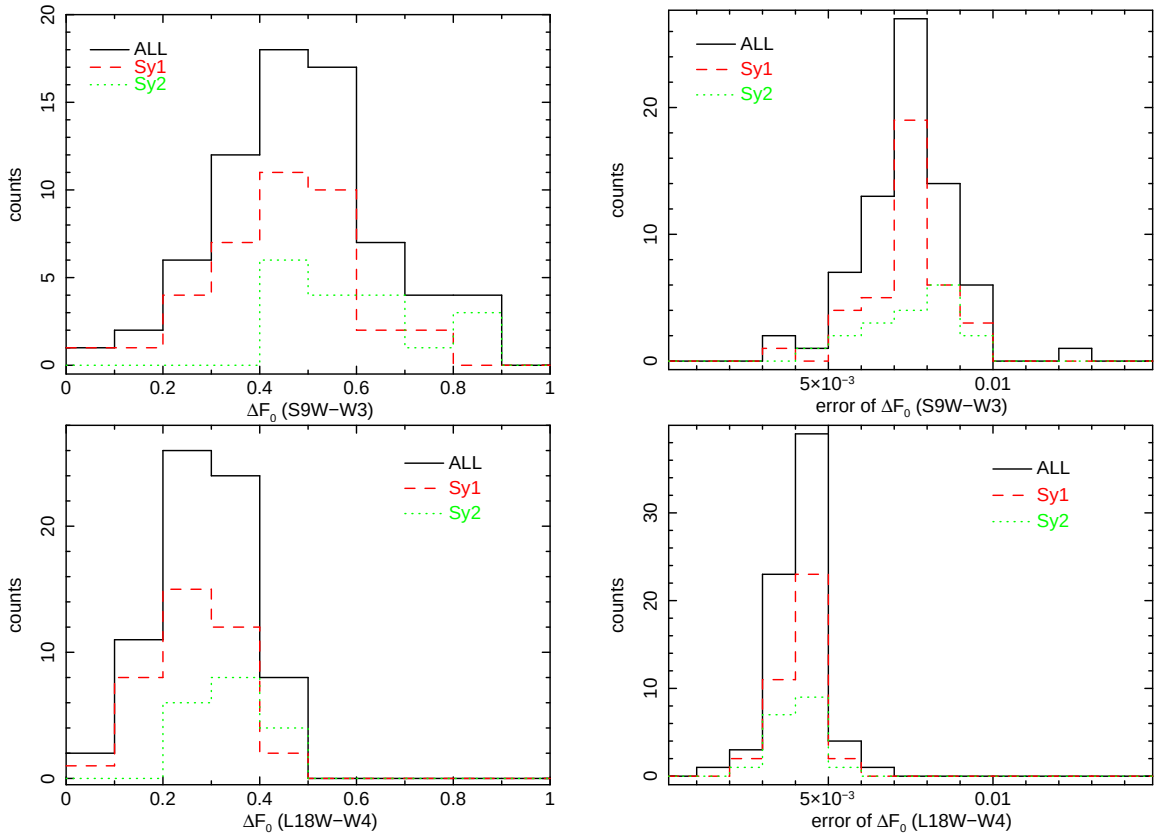

Figure 3.5: Distribution of relative flux ratio, ΔF_0, between *AKARI* and *WISE* due to the difference of the observation bands. Details of the calculation method are found in text. Black-solid, red-dashed, and green dotted lines shows the distribution of all sources (71 sources), Seyfert 1 (38 sources), and Seyfert 2 (18 sources), respectively. The abscissa show the ΔF_0 of each sources. The ordinate show the number of sources. The upper and lower panels are distribution between the S9W-W3 and L18W-W4, respectively. The left and right panels are distribution of ΔF_0 and their errors, respectively. When plotting the histograms, bin sizes were set to $\Delta F = 0.1$ and 0.01 for ΔF_0 and errors, respectively.

I calculate $\Delta F - \Delta F_0$ for each source detected in 4-bands in order to exclude the effect of the variations of the SED slopes from relative flux ratios. I show the distribution of $\Delta F - \Delta F_0$ in Figure 3.6. However, the center of the distribution in S9W-W3 bands is offset from zero in all samples. Similar tendency is also seen in the L18W-W4 band. The reason of the offset may be that the centers of the wave bands may be effectively shifted from the isophotal values due to the different slope of SED than Vega. Furthermore, local structures due to the emission/absorption lines in the SED may also be contributed. I summarize statistics of $\Delta F - \Delta F_0$ in Table 3.5.

Table 3.4: Statistics of ΔF_0

Type	N	ΔF_0			
		S9W-W3		L18W-W4	
		average	standard deviation	average	standard deviation
(1)	(2)	(3)	(4)	(5)	(6)
All	71	0.49	0.17 ± 0.02	0.29	0.09 ± 0.01
Sy1	38	0.45	0.15 ± 0.02	0.27	0.08 ± 0.01
Sy2	18	0.60	0.16 ± 0.03	0.35	0.08 ± 0.01
RL1	7	0.39	0.15 ± 0.04	0.23	0.08 ± 0.02
RL2	2	0.70	0.16 ± 0.17	0.40	0.09 ± 0.06
BL	4	0.42	0.21 ± 0.07	0.25	0.12 ± 0.05

Col. 1: Object type. Col. 2: Number of sources in each subsamples. Col. 3 and 5: Average of the ΔF_0 in the S9W-W3 bands. Col. 4 and 6: Standard deviation of the ΔF_0 in the L18W-W4 bands.

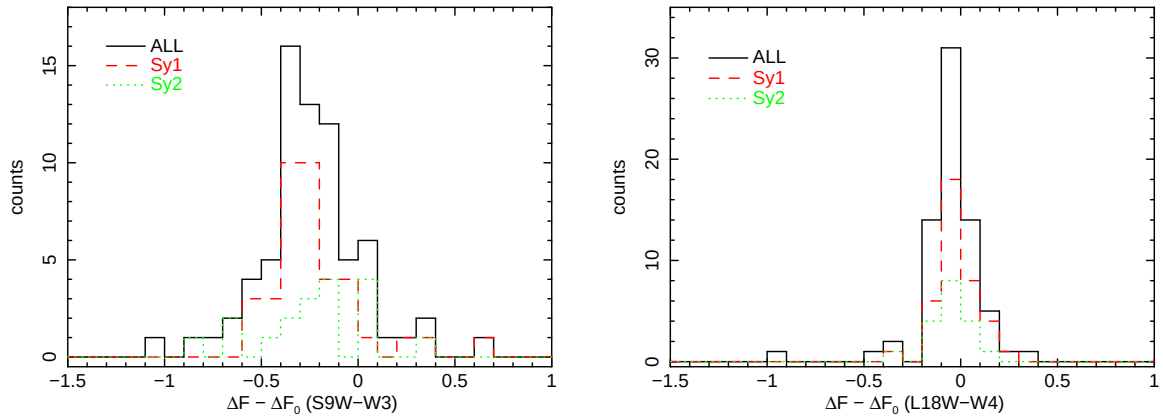

Figure 3.6: Distribution of $\Delta F - \Delta F_0$ between *AKARI* and *WISE*. Black-solid, red-dashed, and green dotted lines shows distribution of all sources (71 sources), Seyfert 1 (38 sources), and Seyfert 2 (18 sources), respectively. The abscissa show $\Delta F - \Delta F_0$ of each sources. The ordinate show the number of sources. The left and right panels are distribution between the S9W-W3 and the L18W-W4, respectively. When plotting the histograms, bin size was set to $\Delta F = 0.1$.

3.4.4 Variability criteria

I have introduced the relative flux ratios corrected for the wave band differences in the previous subsections. These ratios can be the basis to search the catalogs for the variable sources. However, it would be more convenient to normalize the ratios with the errors, because the normalized ratios are directly related to the significance of variations. Thus, I introduce the variability criteria R following Enya et al. (2002c) as follows:

$$R_i = \frac{\Delta F^i - \Delta F_0^i - f_c}{\sqrt{\delta\Delta F^{i\,2} + \delta\Delta F_0^{i\,2}}}. \tag{3.9}$$

Here, ΔF^i is the relative flux ratio defined in Equation 3.2, ΔF_0^i and $\delta\Delta F_0^i$ are the correction to the relative flux ratio due to the wave band difference and its error, respectively (Section 3.4.3).

Table 3.5: Statistics of $\Delta F - \Delta F_0$

Type	N	$\Delta F - \Delta F_0$			
		S9W-W3		L18W-W4	
		average	standard deviation	average	standard deviation
(1)	(2)	(3)	(4)	(5)	(6)
All	71	-0.25	0.27 ± 0.02	-0.04	0.21 ± 0.02
Sy1	38	-0.22	0.24 ± 0.03	-0.03	0.10 ± 0.01
Sy2	18	-0.24	0.30 ± 0.05	-0.05	0.12 ± 0.02
RL1	7	-0.26	0.17 ± 0.05	-0.07	0.24 ± 0.07
RL2	2	-0.34	0.27 ± 0.19	-0.08	0.21 ± 0.08
BL	4	-0.44	0.57 ± 0.23	-0.04	0.88 ± 0.35

Col. 1: Object type. Col. 2: Number of sources in each subsamples. Col. 3 and 5: Average of $\Delta F - \Delta F_0$ in the S9W-W3 bands. Col. 4 and 6: Standard deviation of $\Delta F - \Delta F_0$ in the L18W-W4 bands.

I also introduced a factor f_c, which is equal to the average of $\Delta F^i - \Delta F_0^i$ (-0.23/-0.04 in S9W-W3/ L18W-W4 for all sources, Table 3.5). f_c is effectively a 'fudge' factor used for setting the average of the numerator to zero for each subtype. $\delta\Delta F^i$ is an error of ΔF^i calculated according to the law of error propagation,

$$\left(\frac{\delta\Delta F}{\Delta F}\right)^2 = \left(\frac{\delta F_W}{F_W}\right)^2 + \left(\frac{\delta F_A}{F_A}\right)^2 + C^2 \tag{3.10}$$

where F_W and F_A are fluxes listed in *WISE* and *AKARI* catalogs, respectively, and δF_W and δF_A are their respective errors. I also introduced a constant factor, C, to incorporate the cross-calibration error between *AKARI* and *WISE* (Appendix C). C is independent of types of the source, and its value is 1.5% and 4.1% of fluxes in the S9W-W3 and L18W-W4, respectively. Note that the variability criterion R can be defined for those detected in 4-band wavelengths. Those detected less than 4 bands are not analyzed here (4 and 38 sources in the S9W-W3 and L18W-W4, respectively).

I show frequency distribution of R in a bar chart in Figure 3.7 for the cross-identified AGN in the S9W-W3 and L18W-W4 bands. It is clear that most of AGN have R concentrated around $R = 0$ with a few exceptions. These exceptional sources may be time variable ones. In order to evaluate the statistical significance of these sources, I fit the distribution by the Gaussian model, and the best-fit σ of 1.60, and 0.85 were obtained (Figure 3.8). I list largely deviated sources with $> 5\sigma$ confidence limit in Table 3.6. These are the best candidates of variable sources. Fractions of the variable sources defined as $|R| > 5\sigma$ are 2 sources (3%) in each band. Only 1 source, which is a blazar, shows significant variability in both bands.

After excluding significantly variable sources in Table 3.6, I calculated the standard deviation and error of R for the remaining samples by using Equation 3.3 and Equation 3.4. The standard deviation is 2.36 ± 0.20 and 1.17 ± 0.10 in the S9W-W3 and L18W-W4, respectively. It is noteworthy that these standard deviations are calculated according to their definition (root mean square of the deviation from the sample average), and are different from sigma obtained

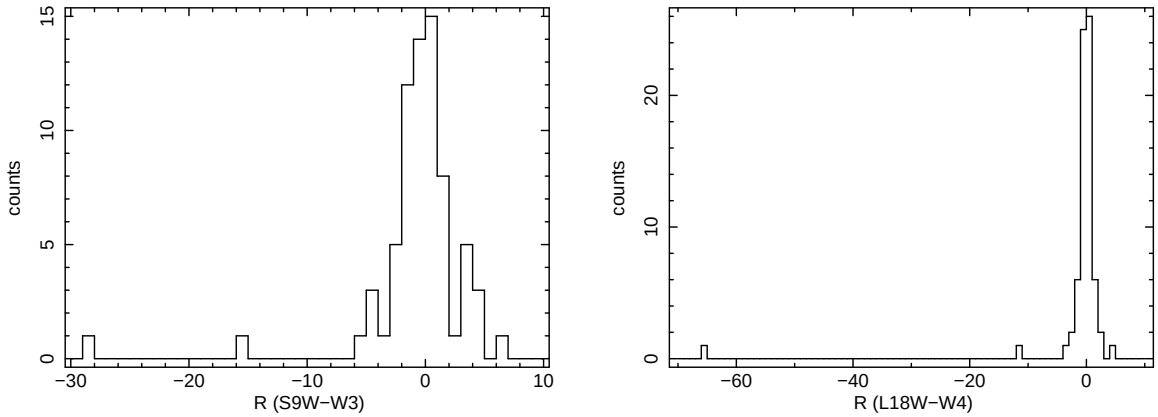

Figure 3.7: Distribution of the variability criteria, R defined in Equation 3.9. The abscissa show R of each sources. The ordinate show the number of sources. The left and right panels are histograms in the S9W-W3 and L18W-W4 bands, respectively. The number of sources are both 71. In both distribution, the bin size is set to $R = 1$.

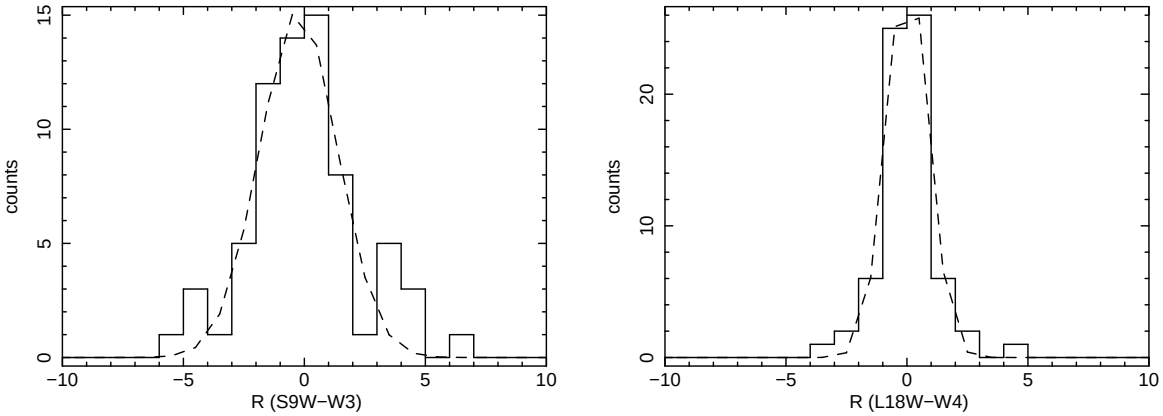

Figure 3.8: Same as Figure 3.7, but the center part of the histograms is magnified. The abscissa show R of each sources. The ordinate show the number of sources. The left and right panels are histograms in the S9W-W3 and L18W-W4 bands, respectively. In both distribution, the bin size is set to $R = 1$. The dashed line show the Gaussian model to best fit the data, which has $\sigma = 1.60$ and 0.85 in the S9W-W3 and L18W-W4 bands, respectively.

from the fitting of a Gaussian model to the histograms. It is immediately noticed that the standard deviation is significantly larger than unity for the S9W-W3 band. This means that the sample distribution in the S9W-W3 is much larger than that expected from the pure statistical variations of the sources. On the other hand, the sample distribution in the L18W-W4 may be consistent to the pure statistical one. In order to evaluate the presence of extra variability, it is crucial to estimate the confidence interval of the standard deviations accurately. Equation 3.4 assumes normal distribution of the data, which is not necessarily true in this case. Thus, I applied the bootstrap method to estimate the reliable confidence interval of the standard deviations. In the bootstrap method, no a priori assumption is made for the parent distribution of the data. The data themselves, R in this case, are assumed to compose the parent distribution, and samples are selected randomly allowing redundancy. This trial is repeated many times to determine the confidence interval. The bootstrap method is applied for both S9W-W3 and

Table 3.6: Sources variable at >5 sigma significance level

Object name	F_{S9W} (mJy)	F_{L18W} (mJy)	F_{W3} (mJy)	F_{W4} (mJy)	R S9W-W3 / L18W-W4	Type
(1)	(2)	(3)	(4)	(5)	(6)	(7)
Variable in both band						
3C 345	102 ± 7	353 ± 8	30.1 ± 0.3	76 ± 1	–28.82 / -65.99	BL
Variable only in the S9W-W3 bands						
3C 273	276 ± 3	454 ± 7	277 ± 2	556 ± 6	-15.59 / -2.56	BL
Variable only in the L18W-W4 bands						
3C 445	141 ± 13	358 ± 6	148 ± 1	267 ± 3	-0.86 / -11.28	RL1

Col. 1: Object name. Col. 2–3: Flux and flux error in 9 (S9W) and 18 (L18W) μm taken from *AKARI*/PSC in units of mJy. Col. 4–5: Flux and flux error in 12 (W3) and 22 (W4) μm taken from *WISE* all-sky source catalog in units of mJy, which are converted from that in units of magnitude by Equation 3.1. Col. 6: Variability criteria in the S9W-W3 and L18W-W4 bands estimated by Equation 3.9 with Col. 2–5. Col. 7: Optical AGN type taken from Tueller et al. (2010). BL = Blazar. RL1 = type 1 radio-loud AGN.

L18W-W4 bands. I summarize all the results in Table 3.7. I could not calculate averages and standard deviations for CT AGN and LINER in both bands because the available sample is only one. Similarly, the results may not be reliable for RL 2 and BL because of the small number of samples.

In summary, I could find three sources clearly variable in the mid-IR band by using the variability criteria R. The statistics of variability criteria for sample AGN show that the sample as a category may be variable at least in the S9W-W3 band.

Table 3.7: Statistics of variability criteria R

Type	N	R			
		average	standard deviation	confidence interval	
				68%	95%
(1)	(2)	(3)	(4)	(5)	(6)
			S9W-W3 band		
All	69	0.003 ± 0.19	2.36 ± 0.20	2.11–2.54	1.92–2.75
Sy1	38	-0.11 ± 0.12	2.33 ± 0.27	1.96–2.60	1.63–2.89
Sy2	18	-0.15 ± 0.31	2.69 ± 0.46	2.20–3.02	1.74–3.37
RL1	7	-0.10 ± 0.10	1.77 ± 0.51	1.26–1.89	0.93–2.17
RL2	2	0.47 ± 0.20	1.69 ± 1.19	–	–
CT	1	...	...	...	...
LI	1	...	...	...	...
BL	2	7.97 ± 0.16	7.30 ± 5.16	–	–
			L18W-W4 band		
All	69	0.01 ± 0.14	1.17 ± 0.10	1.01–1.29	0.88–1.43
Sy1	38	-0.11 ± 0.14	1.00 ± 0.12	0.79–1.16	0.66–1.32
Sy2	18	0.10 ± 0.11	1.14 ± 0.19	0.93–1.26	0.74–1.41
RL1	6	0.25 ± 0.22	0.98 ± 0.31	0.50–1.12	0.24–1.29
RL2	2	0.09 ± 0.07	1.51 ± 1.07	–	–
CT	1	...	...	...	...
LI	1	...	...	...	...
BL	3	0.54 ± 0.17	3.47 ± 1.74	1.42–3.96	< 3.96

Col. 1: Object type. Col. 2: Number of sources in each subtype, from which significantly variable sources listed in Table 3.6 are excluded. Col. 3: Average and error of variability criteria, R. Col. 4: standard deviation and error of variability criteria, R. Col. 5–6: Confidence intervals of standard deviation for R for the confidence limit of 68% and 95%.

3.4.5 Fractional of variability in mid-IR band

I showed in the previous subsection that, in addition to a few numbers of significantly variable sources, the sample as a whole showed extra dispersion due to the time variations difficult to detect individually. Thus I try to quantify the time variations of the sample as a whole in this subsection. For this purpose, I introduce the following quantity, which is defined as the flux variation normalized by the weighted-mean average flux. In the case of sources detected in *AKARI* and *WISE* 4-bands wavelengths, it is defined as:

$$I^i = 100 \times \frac{F_W^i - (1 + \Delta F_0^i + f_c)F_A^i}{\overline{F^i}} \tag{3.11}$$

$$\overline{F^i} = \frac{\delta {F_A^i}^2 F_W^i + \delta {F_W^i}^2 (1 + \Delta F_0^i + f_c)F_A^i}{\delta {F_A^i}^2 + \delta {F_W^i}^2} \tag{3.12}$$

Here, I^i is the flux variation relative to weighted-mean flux $\bar{F^i}$. R is useful to judge the significance of time variation for each source, whereas I^i is suited to quantify variability as a whole because I^i indicate fractional variability of the source. In this analysis, I excluded significantly variable sources with $> 5\sigma$ confidence limit in Table 3.6.

I show frequency distribution of I^i in a bar chart in Figure 3.9 for 4-band detected AGN. Also, I show distribution for the subtypes of Sy 1, Sy 2, and RL 1 in Figure 3.10. The width of the distribution indicates the relative variability of the samples as a whole, but attention should be paid to the contribution of the statistical errors. The width results from both the statistical variations and time variations. The former is defined by the statistical errors of the data. The statistical variations of I^i, which is denoted as δI^i hereafter, is estimated with Equation 3.13. Here I ignored errors of ΔF_0^i and $\overline{F^i}$, because they originate from the errors of F_W^i and F_A^i and do not compose of independent errors. With this equation, I define, δI^i, the standard deviation corresponding to the time variation of the sample as follows:

$$(\delta_{\rm s} I^i)^2 = 100^2 \times \left\{ \left(\frac{\delta F_W^i}{\overline{F^i}} \right)^2 + \left(\frac{1 + \Delta F_0^i + f_c}{\overline{F^i}} \delta F_A^i \right)^2 \right\} \tag{3.13}$$

$$\sigma_I^{\rm int 2} = \frac{1}{N-1} \sum_i \{ (I^i - \bar{I})^2 - (\delta_{\rm s} I^i)^2 \}. \tag{3.14}$$

In this definition of $\sigma_I^{\rm int}$, contribution from the statistical variation is subtracted. The results are summarized in Table 3.8. The error of standard deviation, $\sigma_I^{\rm int}$, are calculated with Equation 3.4. Additionally, I calculate confidence intervals of standard deviation for each subsample using the bootstrap method. I calculate two types of confidence intervals in different levels (68% and 95%) with 2000 trials, and summarize the results in Table 3.8.

I found that Seyfert 1 in the S9W-W3 show significant variability of ∼10% in 95% confidence level. Seyfert 2 and RL 1 AGN show ∼20% and ∼10% variability in 68% confidence level, but they becomes insignificant in 95% confidence level.

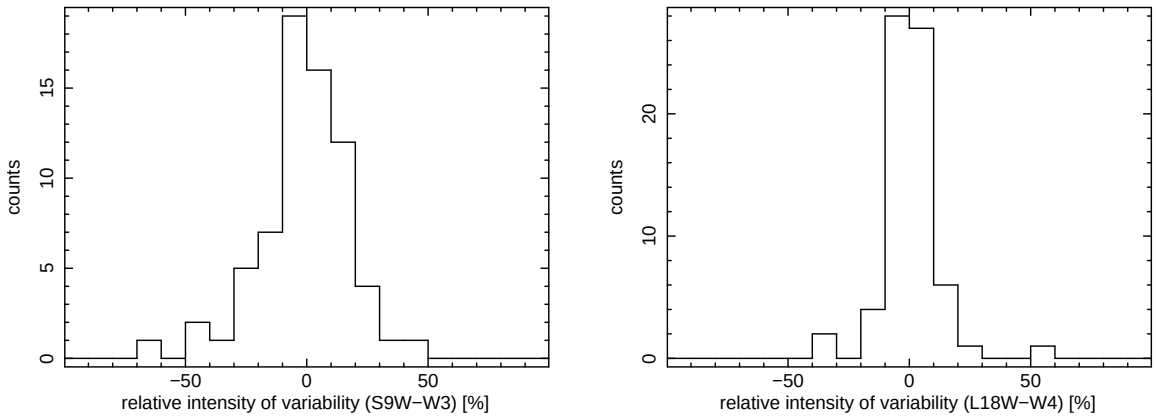

Figure 3.9: Distribution of relative variability of intensity for the total sample of AGN. Left and right figures are histogram in the S9W-W3 and L18W-W4 bands, respectively. The abscissa show relative variability of intensity, I^i, in units of %. The ordinate show the number of sources. In both distribution, the bin size is set to 10%.

Table 3.8: Statistics of variability fraction

Type	N	variability fraction		
		standard deviation	confidence interval	
		%	68%	95%
(1)	(2)	(3)	(4)	(5)
S9W-W3 bands				
All	69	14.4 ± 1.6	11.4–17.0	7.9–19.5
Sy1	38	13.2 ± 1.9	9.8–15.6	6.2–18.0
Sy2	18	19.5 ± 4.4	11.1–23.8	< 28.4
RL1	7	11.5 ± 4.1	5.1–13.6	< 16.5
RL2	2	< 14.4	–	–
CT	1	...	...	...
LI	1	...	...	...
BL	2	< 3.1	—	—
L18W-W4 bands				
All	69	5.2 ± 1.0	< 12.3	< 19.5
Sy1	38	< 1.0	< 1.8	< 6.1
Sy2	18	4.2 ± 1.9	< 8.9	< 12.3
RL1	6	< 3.8	< 2.1	< 7.0
RL2	2	6.7 ± 6.0	–	–
CT	1	...	...	...
LI	1	...	...	...
BL	3	32.7 ± 16.8	< 35.6	< 35.6

Col. 1: Object type. Col. 2: Number of sources in each subsamples, from which the variable sources in Table 3.6 are excluded. Col. 3: standard deviation and error of fractional variability. Col. 4–5: Confidence intervals of fractional variability for the confidence levels of 68% and 95%.

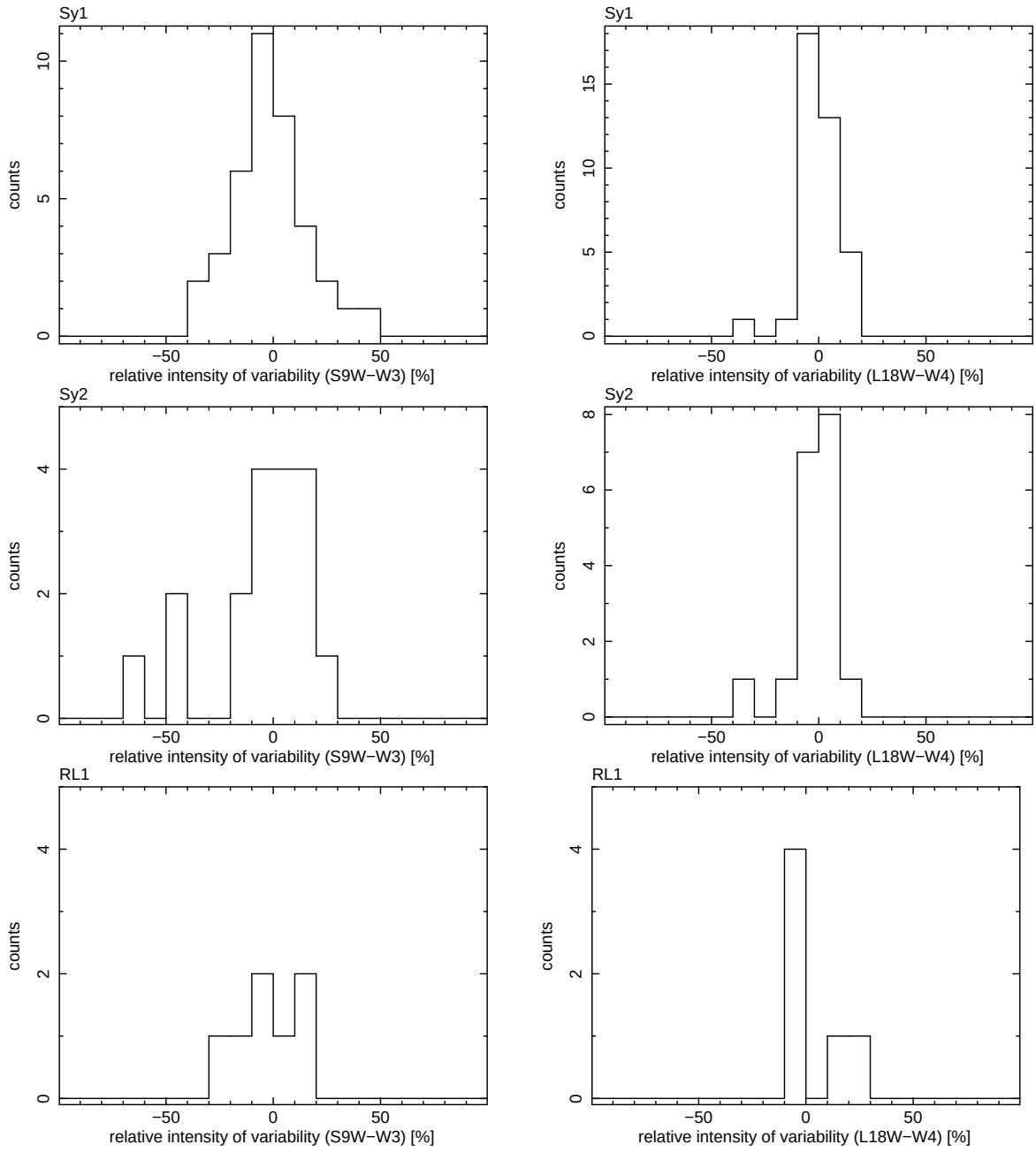

Figure 3.10: Distribution of relative intensity of variability for Seyfert 1, Seyfert 2 and type 1 RL AGN. Left and right figure are distribution in the S9W-W3 and L18W-W4 bands, respectively. Top, middle, and bottom figures are distribution of Seyfert 1, Seyfert 2 and type 1 RL, respectively. The abscissa show relative variability of intensity, I^i, in units of %. The ordinate show the number of sources. In both distribution, the bin size is set to 10%.

Chapter 4

Discussion

4.1 Correlation for each type of AGN

4.1.1 Correlation for Seyfert AGN

Based upon a detailed comparison of the complete, flux-limited *AKARI* and *Swift*/BAT all-sky surveys, I have found a good linear correlation for Seyfert AGN between the logarithms of the observed mid-IR and hard X-ray luminosities over four orders of magnitude (Figure 2.4). The correlation persists even without applying the correction for obscuration or reddening, nor for any contamination by host galaxy. The selected surveys thus provide insight into the nature of mid-IR and X-ray populations of sources selected from all-sky data in a completely unbiased fashion. Statistical tests accounting for redshift effects show that there is definite intrinsic correlation in the two energies for various classes of AGN.

Hard X-ray emission is produced very near the black hole. The soft-to-hard X-ray emission of Seyfert AGN is produced by successive Compton scatterings of the thermal UV photons emitted by accretion disks in hot, most likely patchy coronae formed above the disks (e.g., Haardt & Maraschi, 1993). The high-energy disk and corona emission also heat dusty tori located at further distances from the centers, where the nuclear UV-to-X-ray continuum is re-processed into the thermal IR photons. It is widely accepted that the observed radiative output of Seyfert galaxies at mid-IR frequencies is dominated by the torus emission, which, at least in the case of unobscured (type 1) sources, may even extend up to the near-IR range due to the hot dust located near the dust sublimation radius at the outer edge of the accretion disk (e.g., Elitzur, 2008). In this scenario, result of the good linear correlation for Seyfert AGN between the observed mid-IR and hard X-ray represents well the view of the unified schemes for Seyfert AGN (Antonucci, 1993). Furthermore, no difference between Sy 1s and Sy 2s in the correlation is also consistent to the view of the clumpy torus model.

The best-fit correlation lines for Sy 1s (where we have a direct view of the nuclear regions in both X-rays and IR) are plotted in Figure 2.4 and are used as the benchmark for comparison again among various source classes in the following sections. between IR and hard X-ray powers irrespective of source class. The dispersion in these correlations is $\sim$0.3–0.5 dex (cf. σ_r values in Table 2.3). The strength of the correlation decreases towards longer wavelengths (lower ρ

and $\rho_{.z}$) in conjunction with increasing σ_r values. This may be explained by an increasing host galaxy contribution with wavelength, resulting in a large IR spread. It should be noted that although dominated by torus emission in the mid-IR, *AKARI*'s beam will encompass a stronger host galaxy contribution as opposed to observations with large ground-based telescopes. This manifests itself as slightly flatter best-fit correlation slopes as compared to the previously-measured correlation using VLT data by Gandhi et al. (2009, with the caveat that their sample was much smaller). The slopes I now find for the non-CT radio quiet Seyferts in Table 2.3 range over b (9 μm) $\approx$ 0.92–0.99, as compared to the previously measured value of $b = 1.02$ using the same OLS bisector fit statistic. The host galaxy contribution is relatively stronger for lower luminosity AGN. As a result, the total *AKARI* fluxes are systematically biased towards the right (to higher IR powers) in Figure 2.4, thus flattening the correlation (Vasudevan et al., 2010; Mullaney et al., 2011). The effect is small at luminosities of $L_{\rm X} > 10^{43}$ erg s^{-1} and above where most of the BAT AGN lie (see, e.g., Eq. 1 of Vasudevan et al., 2010). This causes the marginal difference in slopes.

In summary, a significant correlation is observed between the hard X-ray and various IR bands for Sy 1 and Sy 2. The correlation is intrinsic to the source fluxes and is common to both Sy 1s and Sy 2s. This supports the view of the clumpy torus model conjectured from the past observations.

4.1.2 Correlation for Compton-thick AGN

The only class of AGN which does not show any correlation between the two bands is CT AGN, with $\rho_{.z}$ values almost zero (Table 2.3). Including CT sources within the class of "Sy 2" results in a decrease of the Sy 2 correlation as well. In order to study the correlation in more detail, I searched the literature for information on the thickness of obscuring columns. I referred to Table 8.1 in Comastri (2004) and other recent results about CT AGN, preferentially those based upon observations carried out above 10 keV with *Beppo*SAX, *Suzaku*, and *Swift*/BAT. I could find appropriate references for all the nine CT AGN from our sample. Their obscuring column densities and relevant references are listed in Table 4.1.

Gandhi et al. (2009) showed that the mid-IR-to-X-ray correlation for CT AGN is almost indistinguishable from that of typical Seyferts, when the X-ray luminosities are corrected for obscuration. The difference here is that I am using observed hard X-ray fluxes and converting them to luminosities without absorption-correction. While absorption does not affect the observed fluxes in the *Swift*/BAT energy band for Compton-thin column densities, down scattering does deplete hard X-ray photons when the column becomes CT (e.g., Ikeda et al., 2009). Our sample contains a range of obscuring column densities, including one AGN with an extreme column of $N_{\rm H} > 10^{25}$ cm^{-2} (the CT sources are listed in Table 4.1). This leads to eliminate any correlation for our relatively-small sample of CT AGN. I show the luminosity correlation between mid-IR (9 μm) and hard X-ray bands, when the X-ray luminosities of CT AGN in samples are corrected for obscuration (Figure 4.1). It is clear that the absorption corrected samples of CT AGN now follow the linear correlation. This figure means that the poor correlation of CT AGN is well

Table 4.1: Properties of Compton-thick AGN

No.	Object Name	Type	$N_{\rm H}$ (10^{24} cm^{-2})	Observation
(1)	(2)	(3)	(4)	(5)
42	NGC 1068	Sy2	$\geq$10	*Beppo*SAX[a]
60	NGC 1365	Sy1.8	4.0	*Suzaku*[b]
159	NGC 3079	Sy2	10	*Beppo*SAX[c]
165	NGC 3281	Sy2	2.0	*Beppo*SAX[d]
190	NGC 4102	LINER	2.0	*Swift*/BAT[e]
221	NGC 4945	LINER	5.3	*Suzaku*[f]
235	Circinus Galaxy	Sy2	4.3	*Beppo*SAX[g]
242	NGC 5728	Sy2	1.4	*Suzaku*[h]
292	NGC 6240	Sy2	2.2	*Beppo*SAX[i]

Col.(1): Object number listed in the 22-month *Swift*/BAT hard X-ray survey catalogue (Tueller et al., 2010). Col.(2): Object name. Col.(3): AGN type taken from Tueller et al. (2010). Col.(4): Column density in units of 10^{24} cm^{-2}. Col.(5): X-ray observatories used for the observations and the references: [a]Matt et al. (1997); [b]Risaliti et al. (2009); [c]Iyomoto et al. (2001); [d]Vignali & Comastri (2002); [e]González-Martín et al. (2011); [f]Itoh et al. (2008); [g]Matt et al. (1999); [h]Comastri et al. (2010); [i]Vignati et al. (1999)

explained by the high obscuration of hard X-ray luminosities. This hard X-ray deficit is useful for isolating CT sources, as discussed in detail in Appendix A. If we look into the correlation carefully, it is noticed that the absorption-corrected CT AGN tend to lie above the correlation. In other word, the hard X-ray absorption is slightly over corrected. This may be due to the simple assumption of uniform absorber for obscuring column. In reality, the obscuring material may have patchy structure, which increase the observed hard X-ray flux than the case of the uniform absorber. This may be the cause of over correction of absorption. This result may conform to the view of the clumpy torus model.

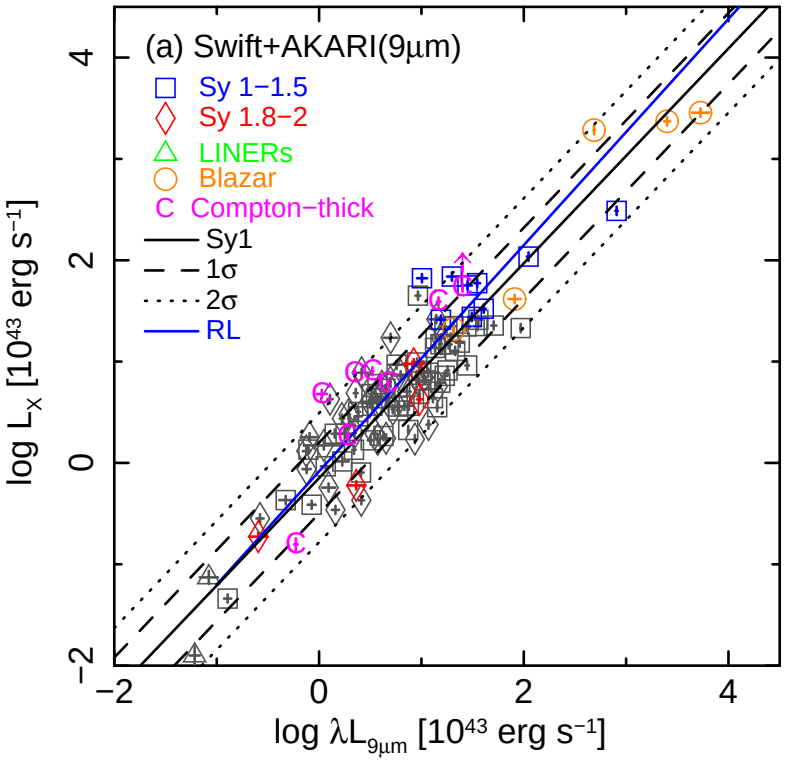

Figure 4.1: Logarithmic luminosity correlations between the *AKARI* and *Swift*/BAT, when hard X-ray luminosities of CT AGN in the sample are corrected for obscuration using the columns listed in Table 4.1. The ordinates are hard X-ray (14-195 keV) luminosities, and the abscissas are IR luminosities at 9 μm. Symbols indicates the AGN types (Seyfert 1, Seyfert 2, LINERs, and Blazars). Color symbols in the plots are radio-loud AGN and blazars. Gray symbols are radio-quiet AGN. Magenta character "C" indicates Compton thick sources. The black and blue solid lines are the correlation fitted to only Seyfert 1s ("Sy1") and "RL", by using the liner regression algorithm, respectively. The dashed and dotted lines show the standard deviation of the correlation; 1σ and 2σ.

4.1.3 Correlation for radio-loud AGN

4.1.3.1 Radio-loud AGN

RL AGN follow a good linear correlation between the logarithms of mid-IR and hard X-ray luminosities (Figure 2.4). A correlation is also present in flux–flux space as seen by the high $\rho_{.z}$ ($= 0.89$) for the "RL" sample in Table 2.3 in all three *AKARI* bands. The correlation slopes of the RL sample match those of Sy 1s within 1σ uncertainties. The above similarity suggests that the hard X-ray and IR emission processes of RL AGN are similar to Seyferts. RL AGN probed by *Swift*/BAT lie at higher redshifts than Seyferts (median redshift is 0.052 for RL AGN and 0.019 for Seyferts, respectively). But their flux distribution, and in particular, the infrared–to–X-ray flux ratios, are very similar to Seyferts (median flux ratio $R = 1.0 \pm 0.1$ for RL AGN and 1.2 ± 0.2 for Seyferts, respectively), where $R = \mathrm{flux}_{9\mu\mathrm{m}}/\mathrm{flux}_{\mathrm{X-ray}}$.

The scatter in the correlation, on the other hand, is larger for the RL sample in all bands. This can be seen in Figure 2.4 as resulting from a few outliers. In all bands, the sources with the largest offset towards higher X-ray luminosities (i.e., those lying *above* the correlation) are

type 1 RL AGN or blazars. The sources that lie above the 2σ uncertainty of the luminosity correlation for "Sy 1" are radio galaxies with particularly powerful jets 3C 111.0, 4C 50.55, and radio-loud quasar 3C 273 in 9, 18, and 90 μm, respectively.

The origin of the broadband emission of radio galaxies is a matter of considerable debate. With regard to the origin of X-ray emission, Evans et al. (2006) demonstrate that both accretion and jet-related components may be present in all radio galaxy nuclei, with the larger contribution of accretion in more luminous population and vice-versa. Hardcastle et al. (2009) found a good correlation between mid-IR (15 μm, *Spitzer*) and accretion-related X-ray luminosities (in 2–10 keV, *Chandra* and *XMM-Newton* bands) in their sample of 135 radio galaxies. This suggests that the mid-IR emission is mainly from dusty torus and is not strongly affected by the jets, especially in the case of luminous sources with intrinsic X-ray powers above $\sim 10^{43}$ erg s^{-1} similar to the range of luminosities that I am probing. This is also supported by mid-IR spectroscopic analysis of luminous RL AGN (Leipski et al., 2010), and finally, is also borne out by the similar mid-IR appearance of radio-quiet and radio-loud quasars in the composite spectra assembled by Elvis et al. (1994).

Hardcastle et al. (2009) did note that quasars and BLRG in their sample tended to have higher X-ray luminosities than the low-power radio galaxies of similar IR luminosity, suggesting that the X-ray powers of brighter sources can be more severely contaminated by jet emission. Our observed outliers appear to show similar X-ray excesses, so I examined detailed X-ray spectroscopic results already published for these AGN to gain further insight. The X-ray spectra of 3C 111.0 obtained with *Suzaku* indeed showed jet dominant component in the hard X-ray band, as found by Ballo et al. (2011). On the other hand, in the broadband X-ray spectra of 4C 50.55 determined by *Suzaku* and *Swift*/BAT data, there is little jet contribution to hot coronal Comptonization (Tazaki et al., 2010). 3C 273 will be discussed in the next section. It is interesting to note that both 3C 111.0 and 4C 50.55 belong to the class of BLRG, which was the only class for which Sambruna et al. (1999) identified some systematic differences in X-ray spectral slope (albeit weak) with respect to radio quiet AGN. On the other hand, other BLRGs such as 3C 120 (Kataoka et al., 2007) are not largely offset from our correlation.

In summary, I lack conclusive evidence of any strong and systematic differences for our RL samples as a whole, though some jet contribution (and related excess variability) may explain slight offsets in the IR–X-ray correlation plane for some objects. In any case, RL sources join on to the luminous end of the sample of Seyferts and extend the observed correlation in that regime.

4.1.3.2 Blazars

The broadband spectra of blazars are thought to be dominated by non-thermal emission from their relativistic jets (Bregman, 1990; Fossati et al., 1998). The IR regime of FSRQs is mainly synchrotron radiation, and hard X-rays are from the inverse-Compton scattering of soft seed photons produced either within the jet (synchrotron self-Compton process) or external to the jet (e.g., within the broad emission line region or dusty tori). In the case of low-power BL

Lacs, X-rays are typically dominated by the high-energy tail of the synchrotron continuum. Such "high frequency-peaked" BL Lacs are however absent in our BAT/*AKARI* sample. Other components including accretion disk and host galaxy emission are present in most sources at a weaker level (e.g., Abdo et al., 2010). Whether or not a torus contributes to the IR emission is debated, but it is generally found to be present more often in luminous FSRQ sources than in BL Lac (e.g., Malmrose et al., 2011; Plotkin et al., 2012).

Our blazar sample contains four FSRQs and two BL Lac. Although the sample size is small, I find high values for partial correlation coefficients between the IR and hard X-ray fluxes for blazars ($\rho_{.z} \approx 0.8 - 0.9$ in 9 and 18 μm; see Table 2.3). This is expected if the various synchrotron and inverse Compton components are intrinsically correlated. On the other hand, the apparent observation from Figure 2.4 that blazars extend the Sy 1 correlation is likely to be a coincidence. This is because the correlation implies a near 1:1 absolute normalization (i.e., mid-IR luminosities are very similar to the hard X-ray powers), which may be explained according to the 'blazar sequence' of Fossati et al. (1998). Figure 12 of their work shows that the *AKARI* (9 μm) and *Swift*/BAT (14–195 keV) bandpasses sample similar power levels at all luminosities, to within a factor of a few at most. Furthermore, Malmquist bias (a selection bias seen in the flux limited samples) certainly contributes to the luminosity-to-luminosity correlation in flux-limited samples for objects spanning a limited flux range but a large redshift range (e.g., Antonucci, 2011), which is true in the case of BAT-selected blazars. A larger flux range needs to be sampled before detailed conclusions on the origin and validity of the correlation for blazars may be drawn.

Among the blazars, the FSRQ 3C 273 shows the strongest mismatch between the observed hard X-ray and IR powers (lying on or well above the 2σ Sy correlation lines in Figure 2.4). This object is known to show strong multi-component variability (e.g., Courvoisier et al., 1987), which may account for its position in the IR-to X-ray plane.

4.1.4 Constraints on the torus geometry

The reason of the 1:1 luminosity correlation between the two bands is unclear. The accurate discussions about correlations needs to bolometric luminosities in mid-IR band instead of monochromatic luminosities. The bolometric luminosities in mid-IR band correspond to the reprocess power of the torus. I assume the mid-IR bolometric luminosity $L_{\rm IR}^{\rm Bol}$ is similar to the monochromatic luminosity $L_{9\mu{\rm m}}$.

Previous studies of optically selected quasars have found a strong correlation between UV (2500 Å) and X-ray luminosity (2–10 keV), parameterized by $L_{\rm UV}^{\rm Bol} \sim L_{\rm 2-10keV}^{1.18\pm0.05}$ (Vignali et al., 2003; Marchese et al., 2012). I assume the equation of $L_{\rm 2-10keV} \sim L_{\rm 14-195keV}$. Therefore, our correlation in Equation 2.2 represents as $L_{\rm IR}^{\rm Bol} \sim L_{\rm 14-195keV}^{0.94\pm0.06} \sim (L_{\rm UV}^{\rm Bol})^{0.8}$. In the result, the covering factor Ω is estimated as $\Omega \sim L_{\rm IR}^{\rm Bol}/L_{\rm UV}^{\rm Bol} \sim (L_{\rm UV}^{\rm Bol})^{-0.2}$. This value shows that the reprocess fraction decrease with the intrinsic luminosities, and the covering factor (the solid angle of the torus) also decrease with the increase of the intrinsic luminosities. This result consistent the scenario of a "receding torus model", which is that the torus geometrical thickness varies

with source power (Lawrence, 1991; Simpson, 2005).

4.1.5 Summary of the correlation for each type of AGN

In summary, results from the above sections support the view of the clumpy torus model. The hard X-ray/IR-brightest blazars included in our flux-limited sample happen to lie along this correlation as well, which is likely to be a coincidence and not an indication for the presence of dust. Thus, the IR vs. X-ray correlation is a useful empirical tool irrespective of the underlying emission physics. This is confirmed by the fact that when I gather all Compton-thin AGN together, irrespective of radio classification, large positive values of $\rho_{.z}$ are found (see "All, ex CT" subsample in Table 2.3).

4.2 Variability of mid-infrared emission from AGN

As described in the previous chapter, I found 3 significantly variable sources (2 blazar, and 1 RL 1) through the systematic studies of mid-IR variability of AGN combining two all-sky surveys. Also, the result of the flux variability for each AGN type suggests that Sy 1 show variability of 6–18% in the S9W-W3 bands with the 95% confidence interval. I discuss implications of these results in the following subsections.

4.2.1 Variable sources in mid-IR band

4.2.1.1 Blazars

Two blazars/FSRQs (3C 345 and 3C 273) show variability with greater than 5σ reliability. Their relative fractional variability is very high ($\sim$50–400%).

3C 345 was observed highly variable in all wave bands including mid-IR. In mid-IR, observations were rather sparse, but time variations of an order of magnitude was clearly detected. In the monitoring at Palomar Observatory of 3C 345 at 1.2–10.2 μm (Bregman et al., 1986), about 60–70% variability time scale of a few years are found that generally correspond to similar optical events. Similar variability ($\sim$50% in 12–25 μm) time scale of a few months was observed by pointed *IRAS* observations (Edelson & Malkan, 1987).

3C 273 is a bright blazar and well studied by multi-wavelength observations. By monitoring observations over two decades at 10.6 μm, variability $\sim$1 mag was detected for a few years (Neugebauer & Matthews, 1999). Its blazar nature is more apparent at near-infrared than at optical wavelengths. Monitoring observations for 4 years in the near-IR and radio bands detected several flares, in which the near-IR fluxes increased by a factor of a few (Robson et al., 1993). McHardy et al. (1999) showed that the X-ray (3-20 keV) and near-IR (K band, 2.2 μm) variability from 3C 273 was highly correlated. The strong correlation supports the synchrotron self-Compton model, where the seed photons of near-IR band are synchrotron photons from the jets.

Thus the two blazars we detected significant variability are consistent to the past observations. The origin of mid-IR emission from blazars is mainly synchrotron radiation by relativistic electrons in the jets, which shows in general high variability with flares.

4.2.1.2 Radio-loud AGN

3C 445 is nearby ($z = 0.056$) FR II radio galaxy. I found that its fractional variability is $\sim$–50% in L18W-W4 bands. On the other hand, in S9W-W3 bands, it is $\sim$–9%.

The origin of mid-IR emission from radio-loud AGN is not clear. From the comparison of SEDs between BLRGs and a blazar (3C 273), Grandi & Palumbo (2007) suggested that the infrared bump of radio galaxies recalls the synchrotron peak of blazars, and the hard spectral slope of their simulated jet resembles non-thermal inverse Compton emission. On the other hand, from the statistical analysis of 19 3CRR radio-loud galaxies including 3C 445 in mid- to far-IR observations, Dicken et al. (2010) concluded that the dominant heating mechanism for

mid-IR emitting dust is AGN illumination due to correlation between mid-IR luminosities and the AGN power indicator [OIII].

From recent infrared observation of 3C 445, the non-thermal emission was not reported. However, it is difficult to explain the large variability of 3C 445 in L18W-W4 bands by a torus alone. According to the type 1 AGN clumpy torus variability model (Hönig & Kishimoto, 2011), the predicted variability in L18W-W4 bands is smaller than that found from 3C 445 in the present analysis, even if a very strong AGN flare with 50% total luminosity were to be occur. The observed large variability may instead be interpreted as the contribution of the non-thermal emission from the jet.

4.2.2 Fractional of variability for each type of AGN

Through the analysis of fractional variability (Section 3.4.5), I found that Sy 1 show variability ∼13% (6-18%) in S9W-W3 bands at the 95% confidence level. Heretofore, few data exist on 10 μm variability on long timescales for Seyferts. In a two decade long multiwavelength monitoring campaign, Neugebauer & Matthews (1999) found a mean variability of ∼10% at 10 μm from 25 radio-quiet quasars. However the B-band magnitude of Seyferts is lower than that of quasars, our results is first detection that similar variability of quasars can be detected from Sy 1 by observations of different satellites. In next subsection, I discuss about the origin of variability in the mid-IR band.

On the other hand, I could obtain only upper limits for variability of other subsamples. Sy 2 seem to show variability ∼20% (11–24%) in 68% confidence interval, but it becomes insignificant in the 95% confidence interval. Although this is a tantalizing result, I have to conclude that no significant difference is found in the time variations between Sy 1 and Sy 2. This supports the unified model predictions of no significant differences of the tori in Sy 1's and Sy 2's.

There are debates whether the mid-IR emission from non-blazar radio-loud AGN is thermal or a combination of thermal and non-thermal components. Unfortunately, from RL 1, I can only obtain the upper limit of variability $< 20\%$, and it is difficult to understand about the origin of the mid-IR emission from RL AGN.

In our results, I found significant variability from Sy 1 in S9W-W3 bands. There is no significant difference of variability between Sy 1 and Sy 2, although the constraint is weak. This supports the unified model that two subsamples have the similar dust torus.

4.2.3 Correlation between variability and torus radius

The thermal equilibrium relation between the temperature of graphite grains in the torus and the distance from the center is defined as,

$$r = \frac{1.3}{3}\left(\frac{L_{\rm UV}}{10^{46}\ {\rm erg\ s^{-1}}}\right)^{1/2}\left(\frac{T}{1500\ {\rm K}}\right)^{-2.8}\ {\rm pc}, \tag{4.1}$$

r is the distance from the central region, $L_{\rm UV}$ is the UV luminosity, T_{1500} is the grain sublimation temperature (Barvainis, 1987). I included in this equation a factor of ∼1/3 (Kishimoto et al.,

2007; Nenkova et al., 2008; Kawaguchi & Mori, 2010) as indicated by the time lag measurements and collections by Suganuma et al. (2006).

If the central X-ray luminosity is 10^{44} erg s^{-1}, which is median value of our sample of AGN, we can estimate that the luminosity in UV band is $\sim$(2–3)$\times10^{45}$ erg s^{-1} (Elvis et al., 1994; Vasudevan & Fabian, 2007), and the dust grains at 300 K, which is comparable to that emits in 9 μm, lie 10 pc ($\sim$30 light-year) from the central region. The theoretical prediction of the distance of dust grains seems to be large compared to the time variation we estimated ($\sim$13% in 4 years). However, model calculations may be necessary for quantitative evaluations.

According to the type 1 AGN variability model (Hönig & Kishimoto, 2010, 2011), time variation in the mid-IR band as a response to the variation of the incident radiation is largely dependent on dust distribution in the torus. Hönig and Kishimoto defined the dust distribution in the torus with the surface brightness as $S_\nu(r) \propto r^\alpha$. The parameter α defines the dust distribution. When the dust distribution is flat ($\alpha > -0.5$), no clear peak appears in the mid-IR emission as a response to the step function change of the incident radiation. On the other hand, if the dust distribution is compact ($\alpha < -1.5$), the mid-IR emission shows delayed peak in the light curve. The time scale of mid-IR variations near the peak can be shorter than the light crossing time of the torus. In this case, the mid-IR emission is dominated by the Rayleigh-Jeans tail of the hot dust emission located in the inner torus. Although this is rather simplified view of time variations, if the mid-IR variability can be explained by the torus emission only , those detected in Sy 1s ($\sim$13% in 4 years) prefer rather compact distribution of dust in the torus. The mid-infrared variability will become a helpful tool to estimate the dust distribution in AGN tori.

4.2.4 Other origins of variability

In previous subsection, I explain variability by the torus emission based on the unified model (i.e., Seyfert AGN generically classified as radio-quiet AGN). On the other hand, the majority of Seyfert 1 show radio-loudness, which is studied through the nuclear radio-to-optical luminosity ratios (Ho & Peng, 2001). Also, elongated jet-like features are discovered from 14 Seyferts by the Very Large Array (VLA) surveys (Ho & Ulvestad, 2001). The recently ejected jet may contribute to mid-IR variability. If this possibility is true, the jet activity should be observed with recent and future all-sky surveys in the radio band such as the LOw Frequency ARray (LOFAR) and the square Kilometer Array (SKA).

4.3 Correlation between variability and luminosity

The result of the good linear correlation for Seyfert AGN between the observed mid-IR and hard X-rays represents well the view of the unified scheme for Seyfert AGN with the clumpy torus model. The 1:1 correlation between two bands indicates that the covering factor decrease with the increase of the intrinsic luminosity. Also, the results of mid-IR variability of Sy 1 and Sy 2, which show no significant difference, support the unified scheme. If the variability of Sy 1 is originated from the torus, dust distribution in the torus should be compact.

RL AGN also follow a good linear correlation between the logarithms of mid-IR and hard X-ray luminosities, but the scatter in the correlation is larger for the RL sample in all bands. As for the mid-IR variability of Sy 1 and RL 1, I could not obtain significant variability from RL 1 (only the upper limit). Thus, RL AGN may also follow the unified scheme, but it is not clear how much contributions from jets appear in variability.

In summary, the unified model of AGN with the clumpy torus is strongly supported by the results of mid-IR and hard X-ray luminosity correlations and mid-IR variability. The covering factor of the torus is considered to depend on the intrinsic luminosity. Because of poor statistics, I could not obtain clear evidence that the torus IR emission is not strongly affected by the jet, on averaged.

Chapter 5

Conclusion

I have combined two complete, flux-limited all-sky surveys, *AKARI* and *Swift*/BAT, in order to study the connection between the IR and hard X-ray (> 10 keV) bands for AGN. I found a good linear correlation between the logarithms of the observed mid-IR and hard X-ray luminosities over four orders of magnitude. Under the AGN orientation-based unification scheme, this result may be viewed as supporting clumpy torus models, although the broad-band correlation alone cannot prove the underlying emission mechanism for the IR and hard X-ray bands. I also found that all the RL AGN follow a good linear correlation, suggesting that their dominant hard X-ray and IR emission processes are similar to those of radio-quiet sources. Coincidentally, blazars also possess a near 1:1 intrinsic correlation between the two bands, which is due to the fact that the synchrotron and inverse Compton powers match each other well along the blazar sequence. I presented quantitative correlation statistics and showed that artificial redshift effects did not dominate the correlation for Seyferts nor for RL AGN. The correlation fits are a useful empirical tool for observers. Most CT AGN show a large deficit in their observed X-ray powers compared to unobscured AGN. This is expected because high gas column densities, even in the hard X-ray band, diminish their observed fluxes.

In the latter part of my research, I studied mid-IR variability of AGN systematically in order to constrain the geometry of the dusty torus. Combining two sets of all-sky survey data from *AKARI* and *WISE*, I calculated time variations of each source excluding the systematic effects as much as possible. As a result, I found 3 sources, 2 blazars and 1 radio-loud galaxy, significantly variable in the mid-IR band. Also, I estimated average variability for each subtype of AGN excluding the significantly variable sources. I found that Sy 1 shows significant variability of $\sim$13% (6–18% in the 95% confidence interval) in the S9W-W3 band. Comparing the detected variation (13%/4 years) with the model calculation for the type 1 AGN, I conjectured that dust distribution in the torus is compact.

No significant difference was found in the variability of Sy 1 and Sy 2 in S9W-W3 bands, although the constrain was rather weak. Combining the results of mid-IR and hard X-ray luminosity correlations and mid-IR variability, I concluded that the unified model of AGN with the clumpy torus is supported very well, and that Sy 1 and Sy 2 have the similar dust torus.

Appendix A

Photometric diagnostics for source classification

The completeness of the base samples (largely unbiased by obscuration) allows us to examine and design various color correlation plots using the hard X-ray and IR powers which can be useful for source classification in blind surveys. Such diagnostics can be particularly powerful if they are redshift independent and can be shown to hold when redshift K-correction is accounted for.

Photometric diagnostics for identifying various source classes (e.g., by using observed power or flux ratios between various bands) can be simple and powerful observational tools. Unbiased all-sky surveys such as ours are ideal for testing various classification schemes, which may be applied to large blind surveys, and I have carried out such a search. The IR-to-X-ray correlations for Sy 1, Sy 2, and LINERs closely match each other (Gandhi et al., 2009; Asmus et al., 2011). Here, I investigate to what extent Seyferts, RL AGN, and CT sources may be separated using the mid-IR and hard X-ray correlations.

A.1 Radio-loud AGN

As already mentioned, RL AGN (and blazars, with the aforementioned caveats) follow the same correlation as Seyferts in Figure 2.4. But these sources lie at the high luminosity end on both axes. RL AGN can also be separated by using a luminosity vs. flux ratio ($L_{\rm X}$ vs. $\lambda L_{\lambda(9\mu{\rm m})}/\lambda L_{\lambda(90\mu{\rm m})}$) plot, equivalent to an absolute magnitude vs. color diagram. The result is shown in Figure A.1. Non-detected RL AGN were included by using IRC 9 μm and FIS 90 μm detection limits of 0.12 and 0.55 Jy, respectively.

Most Seyferts show a large spread in the mid-IR-to-far-IR ratio with an average value of $\lambda L_{\lambda(9\mu{\rm m})}/\lambda L_{\lambda(90\mu{\rm m})} = 1.03$. Type 1 RL AGN and blazars, on the other hand, occupy the region of high hard X-ray emission and high mid-IR-to-far-IR ratio as compared to other AGN types. Using approximate boundaries of $\log L_{\rm X} > 44.3$ and $\lambda L_{\lambda(9\mu{\rm m})}/\lambda L_{\lambda(90\mu{\rm m})} > 1$ for the box shown in the figure, I find that *all* type 1 RL AGN and blazars lie in this region, i.e., selection is 100% *complete*. On the other hand, the box also contains a few (2/16) sources that are neither

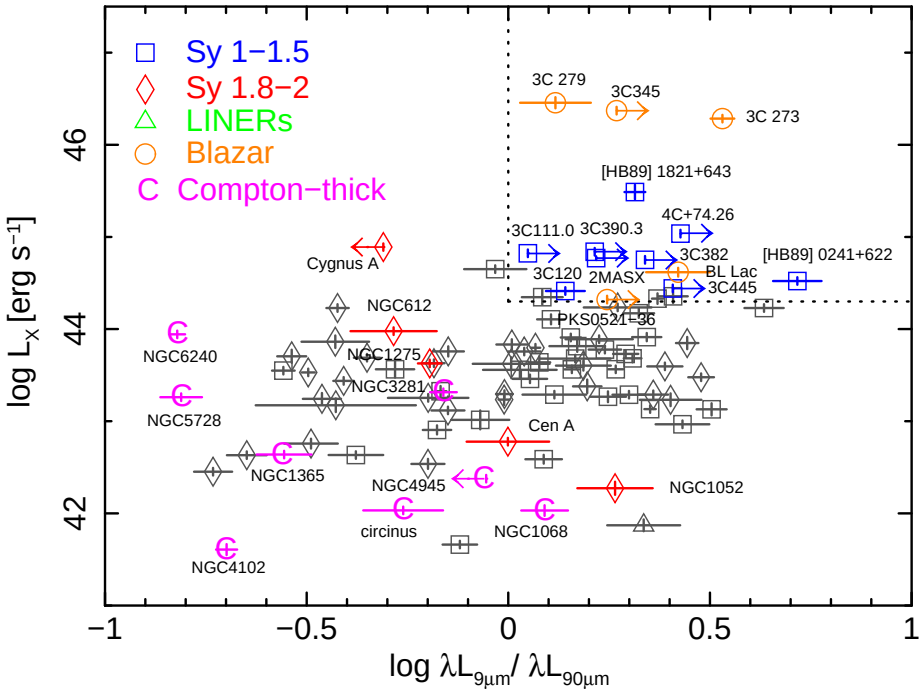

Figure A.1: Absolute magnitude (log $L_{\rm X}$) vs. Color (log $\lambda L_{9\mu{\rm m}}/\lambda L_{90\mu{\rm m}}$) diagram for 89 *Swift*/BAT and *AKARI* detected sources. Color symbols in the plots are radio-loud AGN and blazars. Gray symbols are radio-quiet AGN. Magenta character "C" indicates Compton thick sources. The radio loud sources are located in the upper-right region as indicated by the dotted box. NGC3079, one of the Compton-thick sources, is out of the figure range, (log $L_{\rm X}$, log $\lambda L_{9\mu{\rm m}}/\lambda L_{90\mu{\rm m}}$) = (41.93, -1.69).

type 1 RL AGN nor blazars, i.e., selection is 88% *reliable*. If I classify [HB89]0241+622 and [HB89]1821+643 as radio-quiet (see discussion in section 2.2.3), reliability drops to 75%.

On the other hand, type 2 RL AGN are not clearly separated in this figure. In particular, they show a lower ratio of the mid- to far-IR powers on the ordinates-to-the median values for $\lambda L_{\lambda(9\mu{\rm m})}/\lambda L_{\lambda(90\mu{\rm m})}$ for type 1 RL and type 2 RL are 0.31 and –0.11, respectively. This trend is also seen in the case of the radio-quiet sources (RQ), with the corresponding ratios being 0.16 and –0.16 for type 1 RQ and type 2 RQ, respectively. This trend cannot arise from optically-thick tori in Sy 2 being preferentially 'colder' in the infrared. If this were so, then Sy 2 would also be offset towards lower 9 μm–to–X-ray flux ratios in the IR-to-X-ray correlations. Instead, this trend probably arises because Sy 2 have lower intrinsic accretion (X-ray) luminosities as compared to Sy 1 on average (Winter et al., 2009), as well as a relatively stronger 90 μm contribution from dust in the host galaxy (Malkan et al., 1998). These two facts push down the 9 μm fluxes for Sy 2 and boost their 90 μm fluxes, resulting in the observed trend.

With regard to the fact that blazars occupy the top right of Figure A.1, an x-axis mid–to–far-IR luminosity ratio greater than 1 means that their jet synchrotron peaks must lie in the mid-IR or higher frequencies and not the far-IR or lower frequencies. This is interestingly consistent with the recent study of bright blazars detected at GeV photon energies by Fermi/LAT (Abdo et al., 2010), where no source with the synchrotron continuum peaked at far-IR or lower frequencies

was found. Further investigation is beyond the scope of this paper and is left to future work.

Finally, it is seen from Figure A.1 that there are no luminous X-ray sources with a mid-IR-to-far-IR ratio of less than 1 occupying the top left of the diagram. Type 2 quasars with powerful X-ray emission and bright host galaxies probably occupy this region, but these are known to be elusive and absent in the local universe (e.g., Zakamska et al., 2003; Gandhi et al., 2004, 2006). I also note that I would not have selected sources that are below the *AKARI* detection limit in both 9 and 90 μm. Since our sample contains very few blazars, a selection bias where I miss such sources cannot be ruled out.

In summary, Figure A.1 is helpful for isolating type 1 RL AGN and blazars. Using color and luminosity information I can isolate type 1 RL AGN with high reliability, but this requires knowledge of source redshift.

A.2 Compton-thick AGN

Outliers in the correlation plots of Figure 2.4, which lie *below* the correlation for "Sy 1", are mostly CT AGN. Their average $L_{\rm X}/\lambda L_{\lambda(9\mu{\rm m})}$ ratio is 0.11, as compared to 0.71 for Sy 1. When generating such correlation plots, it is important to use the observed X-ray flux for identifying CT AGN because of the hard X-ray deficit due to Compton down-scattering (Sec. 4.1.2).

The average values of the X-ray-to-IR ratios for other *AKARI* bands are $L_{\rm X}/\lambda L_{\lambda(18\mu{\rm m})} = 0.08$ and $L_{\rm X}/\lambda L_{\lambda(90\mu{\rm m})} = 0.03$. Copious star formation often accompanies obscured AGN activity and several of the CT AGN lie in composite systems also classified as starburst galaxies (e.g., NGC 6240, Circinus Galaxy, NGC 4945. See Table 4.1). The 90 μm to X-ray ratio for CT AGN is large because of an excess far-IR contribution due to bright star formation in the host galaxy (see also Figure 2.4).

A.3 Distinction between Compton-thick AGN and Starburst galaxies

A.3.1 starburst–AGN connection

Starburst galaxies show the large-scale star formation activity. Generally, starburst galaxies are characterized by relatively blue colors and strong HII region-type emission-line spectra due to a large number of O- and B-type stars, and relatively strong radio emission due to recent supernova remnants. If starbursts occur at the galactic center, they look like AGN. However the relationship between AGN and nuclear starburst is not clear, there are some evidences that AGN and starbursts are mutually dependent. Taniguchi et al. (1999) suggest that the violent circumnuclear starbursts could be one of the factors that the ultraluminous infrared galaxies can make SMBHs in the center during their merging. Conversely, it has been argued that the presence of an AGN in a galaxy might trigger a burst of star formation (Rees, 1989; Daly, 1990).

This has been an important problem for many years because star formation and obscured accretion activity often occur together in composite systems (cf. the well known 'starburst–AGN

connection'; e.g., Sanders & Mirabel, 1996; Genzel et al., 1998; González Delgado et al., 1998; Malkan et al., 1998; Schweitzer et al., 2006; Imanishi et al., 2007). The observed soft X-ray and IR appearance is not easily distinguishable in these cases. X-ray information only below 10 keV has been used in most surveys so far. But the observed X-ray fluxes for both these classes of sources in this band need to correct absorption effect. High excitation mid-IR forbidden lines and PAHs can separate the two (e.g., Laurent et al., 2000; Sturm et al., 2002; Dale et al., 2006; Goulding & Alexander, 2009; Weaver et al., 2010), if spectroscopic data are available.

A.3.2 color–color diagnostic

I propose one such color–color diagnostic, and show that it also provides the capability of distinguishing starbursts from CT AGN. I now have new information available from the hard X-ray band above 10 keV. I investigate whether the information is useful for source classification. I checked the hard X-ray emission of starburst galaxies. There is no starburst galaxy detected in the 22-month BAT catalog, so I have extended our search to the 54-month BAT catalog (Cusumano et al., 2010) for this purpose. The detection limits of the 54-month catalog are 1.0×10^{-11} ($|b| < 10^{\circ}$) and 9.2×10^{-12} erg cm^{-2} s^{-1} ($|b| > 10^{\circ}$), respectively. M82 is the only "pure" starburst galaxy detected in this catalog.

Though only one starburst galaxy is detected, hard X-ray predictions on other well-known sources turn out to be interesting for our purpose of comparison with AGN. I picked up two famous "pure" starburst galaxies (NGC 253, Arp 220), and other four "pure" starburst galaxies (NGC 2146, NGC 3256, NGC 3310, and NGC 7714) listed in Brandl et al. (2006), which are all detected in X-rays below 10 keV. I computed hard X-ray flux estimates for these 6 objects by using their observed 2–10 keV fluxes under the two different assumptions of non-thermal and thermal radiation models (The results are listed in Table A.1). These correspond to the emission expected from point sources like X-ray binaries and diffuse thermal gas, respectively (Persic & Rephaeli, 2002). The non-thermal model is based upon the observation of star-forming galaxies in the Hubble Deep Field with an average 2–10 keV X-ray spectral slope (photon index $\Gamma = 2.1$; Ranalli et al. 2003). The thermal model (7 keV `APEC`) is based on the *XMM-Newton* observation of the central region of M82 (Ranalli et al., 2008). Similar starburst-related hot gas bubbles have also been found in Arp 220 (Iwasawa et al., 2005) and NGC 253 (Pietsch et al., 2001).

Because M82 and NGC 253 are very bright in the IR ($\geq$ 100 Jy), the *AKARI* detectors may cause saturation and the flux could have larger uncertainty (Yamamura et al., 2010). The FIS 90 μm fluxes of these two sources are not reliable ($FQUAL = 1$), and there is no IRC 9 μm flux available for M82 in the all-sky survey. Therefore I applied the results of the *AKARI* pointed observation data for M82 (Kaneda et al., 2010) and NGC 253 (Kaneda et al., 2009). In these observations, the IRC and FIS were operated in special observation mode, which is used to observe bright sky regions to avoid detectors saturation.

Figure A.2 shows the results in the form of a $\log L_{\rm X}/\lambda L_{\lambda(9\mu{\rm m})}$ vs. $\log \lambda L_{\lambda(9\mu{\rm m})}/\lambda L_{\lambda(90\mu{\rm m})}$ diagram (equivalent to a color–color plot). I also include an IR color lower limit for the CT AGN, NGC 4945, resulting from it being saturated in the FIS ($\sim$100 Jy). Other CT AGN

Table A.1: The sample of starburst galaxies

Object name	$F_{9\mu m}$ (Jy)	$F_{90\mu m}$ (Jy)	$F_{2-10keV}$ (10^{-13} erg cm^{-2} s^{-1})	$F_{14-195keV}$ (10^{-13} erg cm^{-2} s^{-1})	D (Mpc)
(1)	(2)	(3)	(4)	(5)	(6)
M82	70.0 ± 7.00[a]	2040 ± 410[a]	...	54.0 ± 32.0[b]	3.50[a]
NGC 253	22.6 ± 1.45	1200 ± 240[c]	12.3[d]	15.7 (power-law) ± 1.57 1.76 (APEC) ± 0.18	2.58[d]
Arp 220	0.25 ± 0.01	91 ± 63	0.98[e]	1.25 (power-law) ± 0.13 0.13 (APEC) ± 0.01	72.9[e]
NGC 2146	5.52 ± 0.01	168 ± 15	11.4[f]	14.7 (power-law) ± 1.47 1.65 (APEC) ± 0.17	16.5[j]
NGC 3256	2.39 ± 0.01	108 ± 8	5.86[g]	7.59 (power-law) ± 0.76 0.85 (APEC) ± 0.09	35.4[j]
NGC 3310	1.08 ± 0.02	35 ± 1	21.2[h]	27.2 (power-law) ± 2.72 3.05 (APEC) ± 0.31	19.8[j]
NGC 7714	0.29 ± 0.01	11 ± 1	1.58[i]	2.03 (power-law) ± 0.20 0.23 (APEC) ± 0.02	38.2[j]

Col.(1): Object name. Col.(2)(3): Flux and error in 9 and 90 μm in units of Jy, taken from *AKARI*/PSC and the references below. Col.(4): Flux in 2-10 keV band in units of 10^{-13} erg sec^{-1} cm^{-2}, taken from the references below. Col.(5): Flux and error in 14-195 keV band in units of 10^{-13} erg sec^{-1} cm^{-2}. Except for M82, I simulated the value by using two models, power-law (Γ=2.1) and `APEC` (7 keV). Col(6): Distance in Mpc. [a]Kaneda et al. (2010); [b]Cusumano et al. (2010); [c]Kaneda et al. (2009); [d]Bauer et al. (2008); [e]Teng et al. (2009); [f]della Ceca et al. (1999); [g]Moran et al. (1999); [h]Zezas et al. (1998); [i]Soria & Motch (2004); [j]Brandl et al. (2006)

non-detected at 9 μm are also included as limits. Considering the AGN only, an approximate boundary of $\log L_X/\lambda L_{\lambda(9\mu m)} < -0.9$ successfully isolates CT AGN, i.e., it has very high (100%) reliability. But only 5/8 of CT sources are below this boundary, which means that it is 56% complete. This boundary can successfully identify CT sources, if a source is known to contain an AGN a priori.

But such a priori information is not available for most surveys, and I see from the figure that starburst galaxies also occupy this region. Starburst galaxies (including the single detection of M82 and virtually all prediction ranges) are all concentrated below the line of $\log L_X/\lambda L_{\lambda(9\mu m)} \sim -2.5$. For each source, a vertical line connects the expected range of values based upon the non-thermal model for the X-ray emission (higher horizontal bar) and the thermal model (lower horizontal bar). This shows that the hard X-ray emission from starburst galaxies is expected to be less than $\sim 10^{-3}$ of the mid-IR emission from AGN.

The abscissa, $\log \lambda L_{\lambda(9\mu m)}/\lambda L_{\lambda(90\mu m)}$, shows the ratio of hot-to-cool dust. Starburst galaxies are largely separated on the abscissa as well because of cooler dust temperature compared to AGN. I also tested the ratio of 15 other "pure" starburst galaxies listed in Brandl et al. (2006), and obtained an upper limit of $\log \lambda L_{\lambda(9\mu m)}/\lambda L_{\lambda(90\mu m)} \sim -0.4$. The result shows that the far-IR emission from the cool dust is more dominant than the mid-IR emission from hot dust in the

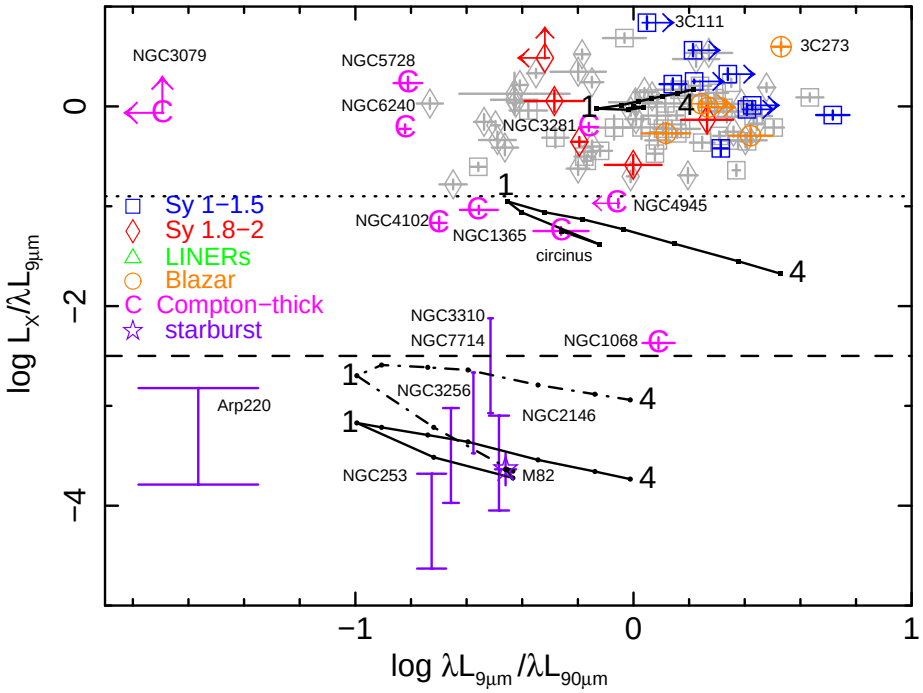

Figure A.2: Color-color plot of log $L_{\rm X}/\lambda L_{9\mu{\rm m}}$ vs. log $\lambda L_{9\mu{\rm m}}/\lambda L_{90\mu{\rm m}}$ for 89 AGN including 9 Compton-thick (CT) sources and 7 starburst galaxies detected by *AKARI*. Color symbols in the plots are radio-loud AGN and blazars. Gray symbols are radio-quiet AGN. Magenta character "C" indicates Compton thick sources. Open purple stars show starburst galaxies in Table A.1, and indicate the estimated hard X-ray (14–195 keV) flux ranges by using the non-thermal (higher bar) and thermal model (lower bar). The dotted line at log $L_{\rm X}/\lambda L_{9\mu{\rm m}}$ ∼–0.9 shows an approximate boundary between normal AGN and CT sources. The dashed line at log $L_{\rm X}/\lambda L_{9\mu{\rm m}}$ ∼–2.5 shows the boundary below which only starburst galaxies are present. The solid lines show how the sources move on the color-color plots when the redshift is changed from 0.0 to 4.0. The lines are calculated for three types of galaxies, a Seyfert galaxy located at (0, 0), Circinus galaxy as a CT AGN, and M82 as a starburst galaxy. The solid and dot-dashed lines for M82 correspond to the different model (non-thermal and thermal, respectively).

local starburst galaxies.

On the other hand, RL AGN are not separated out in this figure. 3C 111 and 3C 273 lie towards the top right region in the plot (again 3C 111 has the largest $\log L_{\rm X}/L_{\rm IR}$ ratio), so it might be possible to define some region here, but in general RL AGN and blazars do not occupy any specific region.

In summary, the hard X-ray and IR color–color plot successfully differentiates the composite CT AGN/starburst galaxies, and also distinguishes these from the remaining sources (Sy 1, Sy 2, LINERs, and RL AGN).

A.3.3 *K*-corrections in the color–color plane

In order to be useful for general source classification, the regions determined in the previous section must be shown to accommodate the effect of SED *K*-corrections at higher redshifts. I

checked this by applying *K*-correction for template SEDs of Seyferts, CT AGN, and starburst galaxies separately. For Seyferts, I use the high-luminosity starburst model spectrum ($L = 10^{13} L_{\odot}$) by Lagache et al. (2003). For CT AGN and starburst galaxies, I use the Seyfert 2 and M82 model spectra, respectively, by Polletta et al. (2007). I show the color tracks on the plane of Figure A.2 when the redshift is varied from $z = 0.0$ to 4.0. I assumed a color–color position of (0, 0) for the local origin of the *K*-correction locus for Seyferts. Similarly, the loci of CT AGN and starburst galaxies start at the positions of Circinus Galaxy and M82, respectively. The plotted loci show that our diagnostic regions are independent of source redshift.

With current and upcoming hard X-ray missions of continually improving sensitivity (e.g., *INTEGRAL*, *Swift*, *NuSTAR*, *eROSITA*, and *ASTRO-H*), and similar increases in sensitivity expected in the IR (e.g., *WISE* and *SPICA*), our work investigates the degree to which blind IR/X-ray surveys can be used for classification and separation of AGN and starburst galaxies, using directly observed photometric properties without the requirement of detailed spectroscopy or source modeling. For instance, changing from the *Swift*/BAT 14–195 keV and *AKARI* 9 μm bands to the *NuSTAR* 6–79 keV and *WISE* 12 μm bands, respectively, the maximal shift in the ordinates of the color–color plane is only $\sim$20% towards lower $L_{\rm X}$, for a Seyfert SED at $z \sim 4$.

Appendix B

SEDs with *AKARI* and *WISE*

Seyfert 1

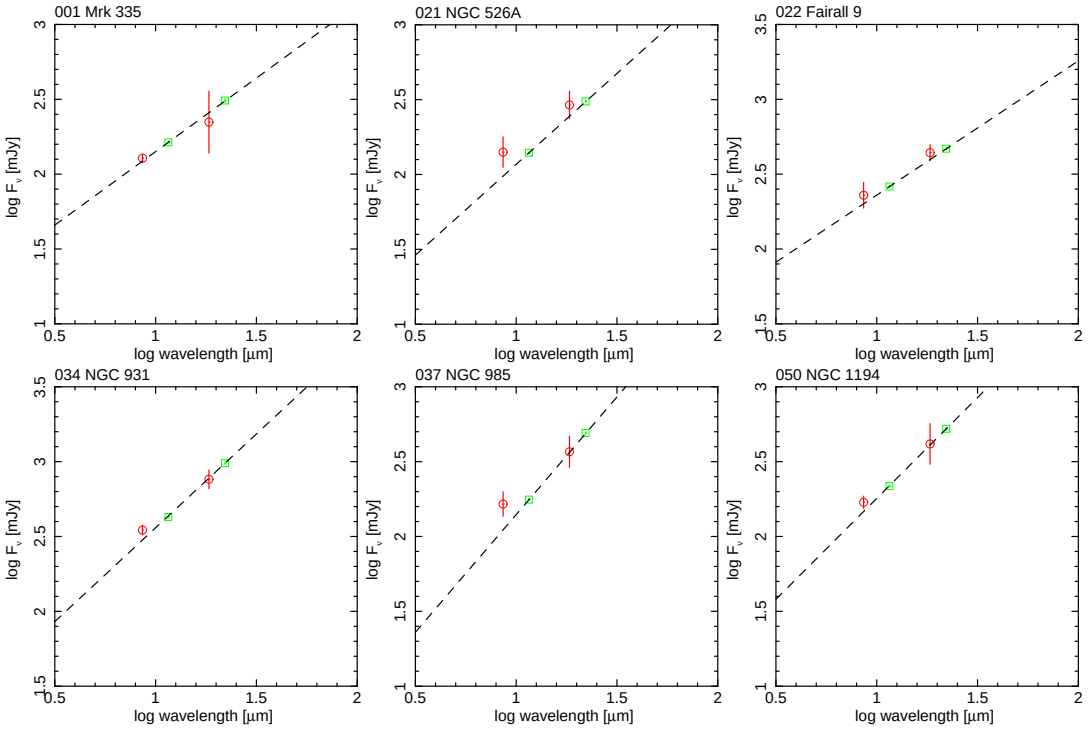

Figure B.1: SEDs of Seyfert 1 with *AKARI* (red point) and *WISE* (green point) bands. In each panel, data points are plotted for the isophotal wavelengths defined as 8.61, 11.56, 18.39, and 22.09 μm for S9W, W3, L18W, and W4, respectively. Object number in the 22-month *Swift*/BAT hard X-ray survey catalog and object name are shown on the top left of a figure. Broken line is the best-fit power-law model to the data.

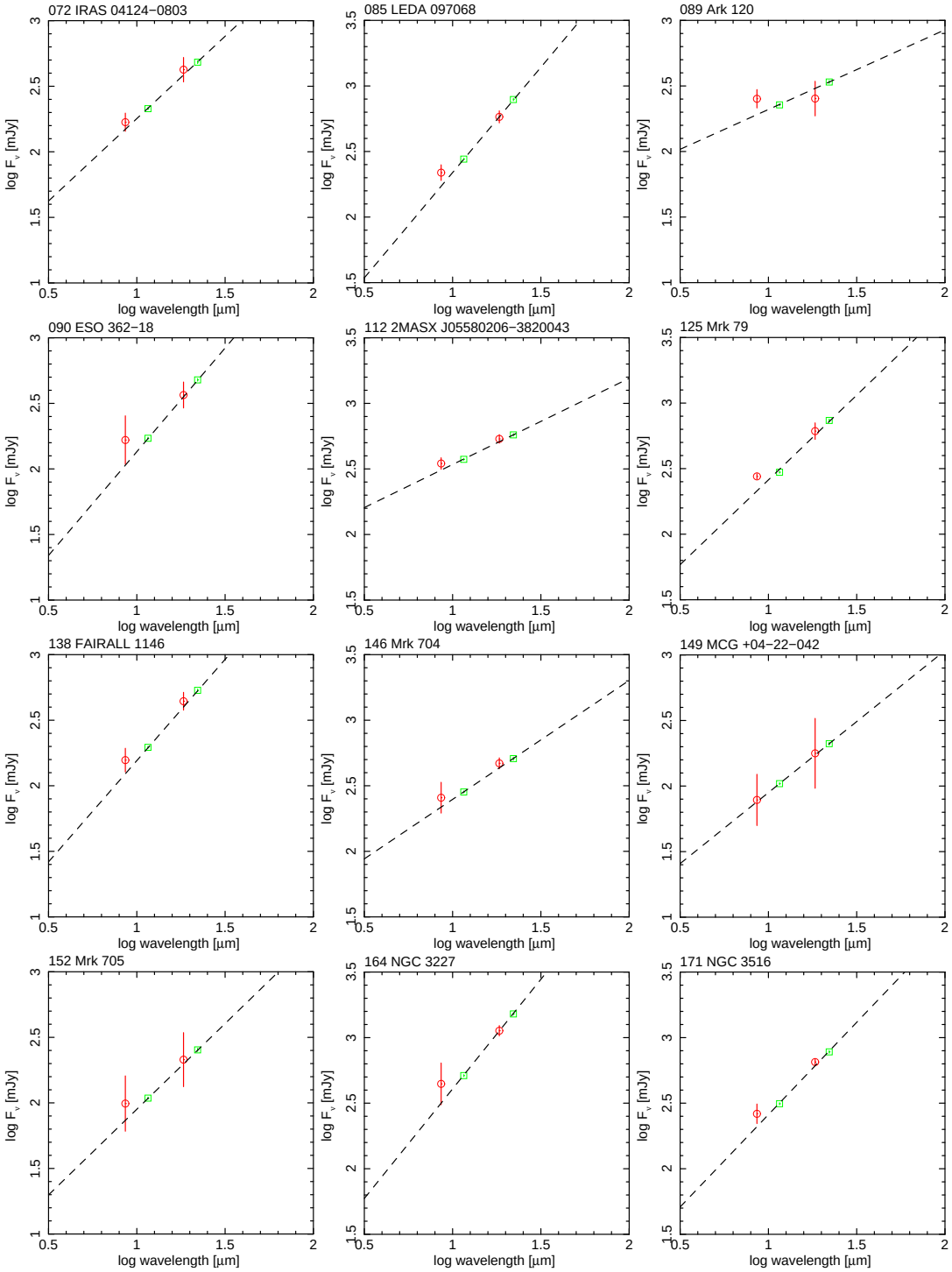

Figure B.1: *Continued.*

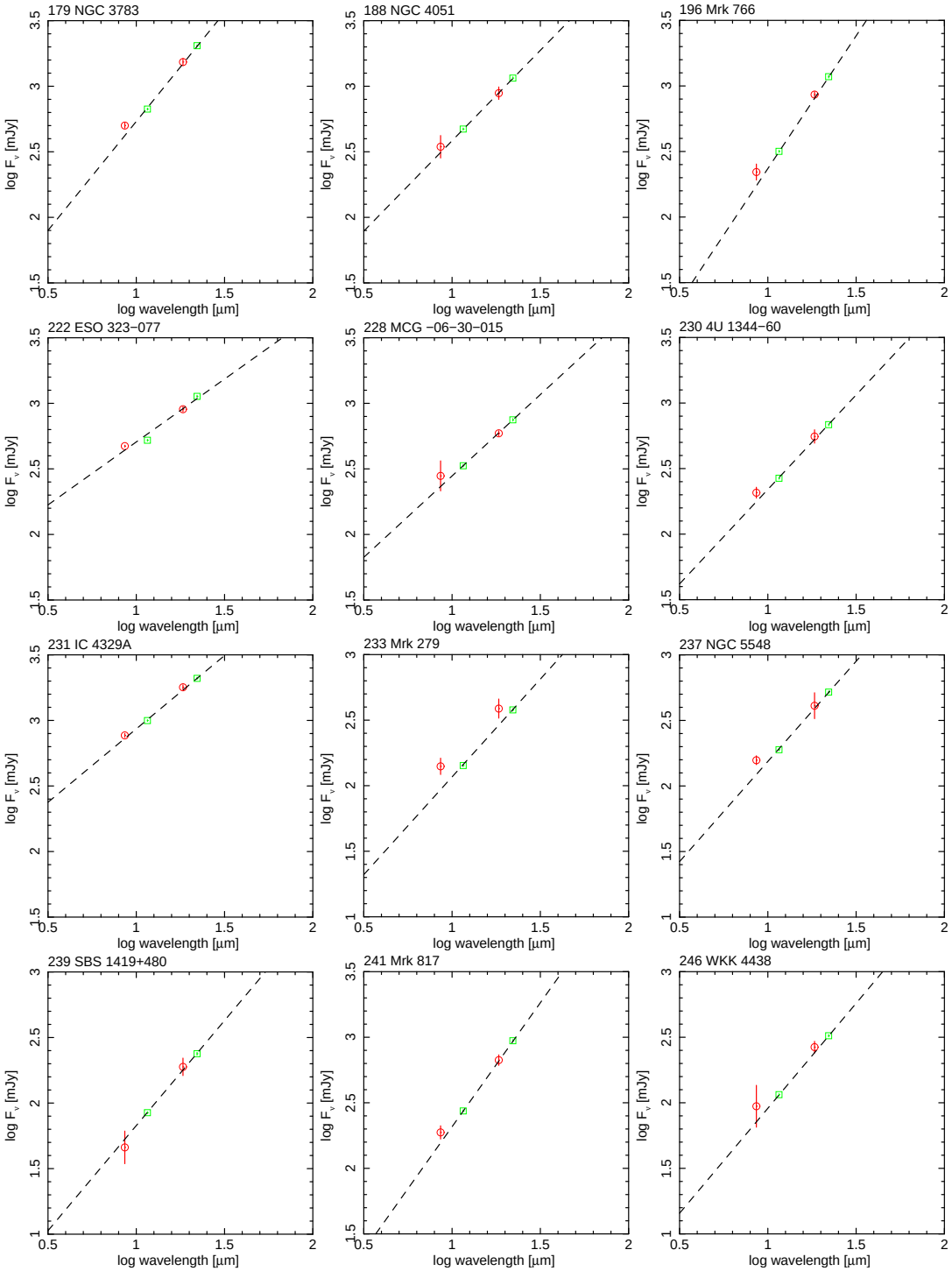

Figure B.1: *Continued.*

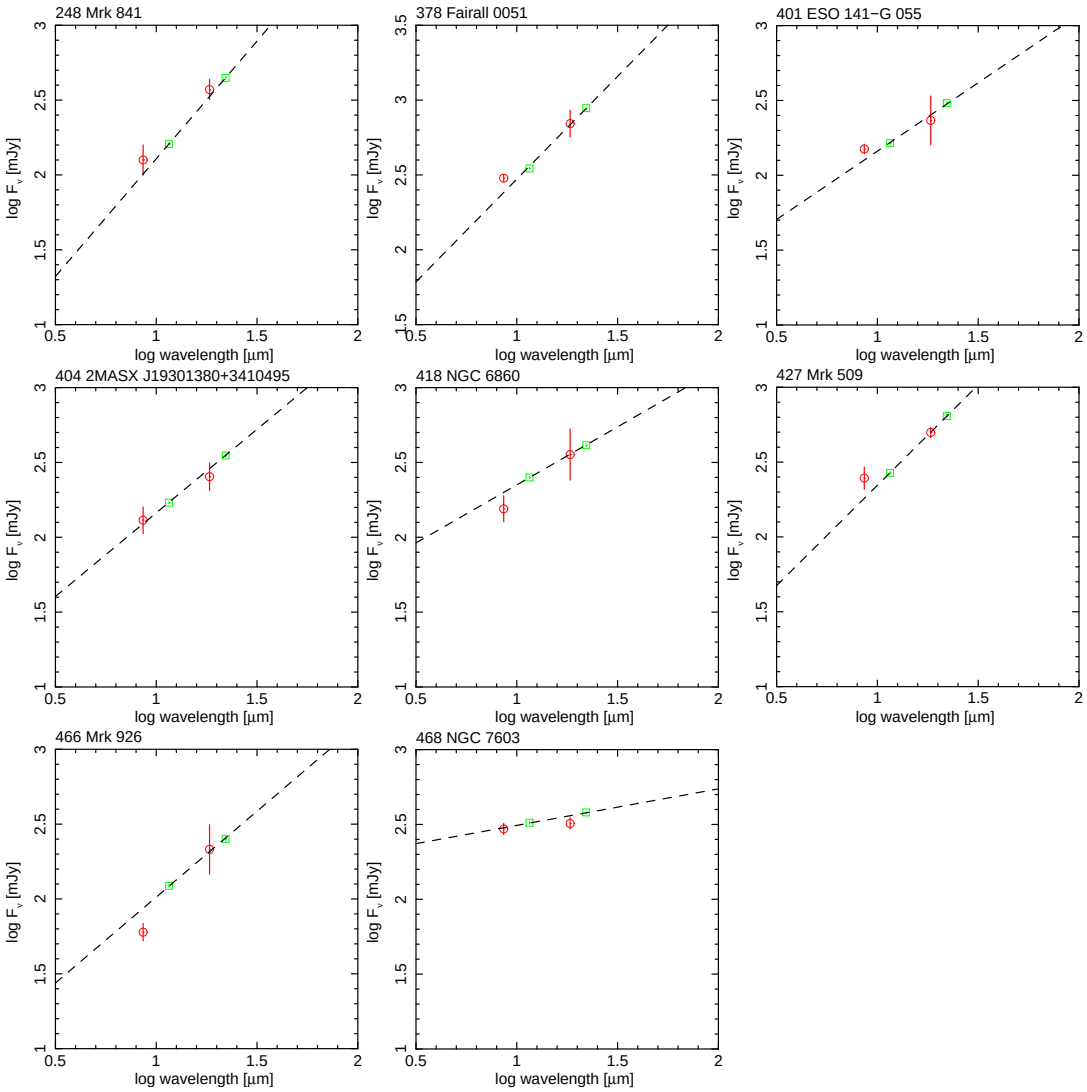

Figure B.1: *Continued.*

Seyfert 2

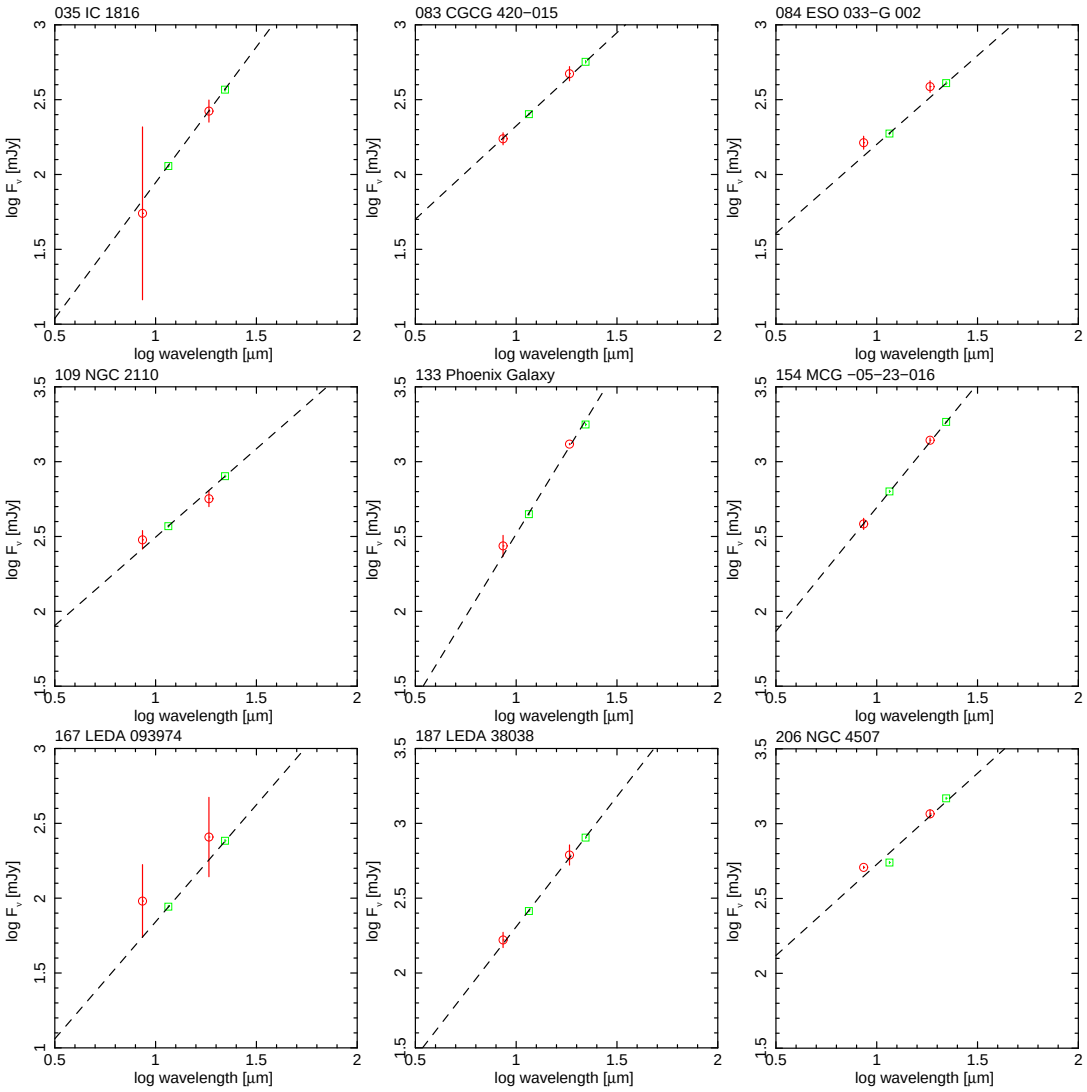

Figure B.2: SEDs of Seyfert 2 with *AKARI* (red point) and *WISE* (green point) bands. In each panel, data points are plotted for the isophotal wavelengths defined as 8.61, 11.56, 18.39, and 22.09 μm for S9W, W3, L18W, and W4, respectively. Object number in the 22-month *Swift*/BAT hard X-ray survey catalog and object name are shown on the top left of a figure. Broken line is the best-fit power-law model to the data.

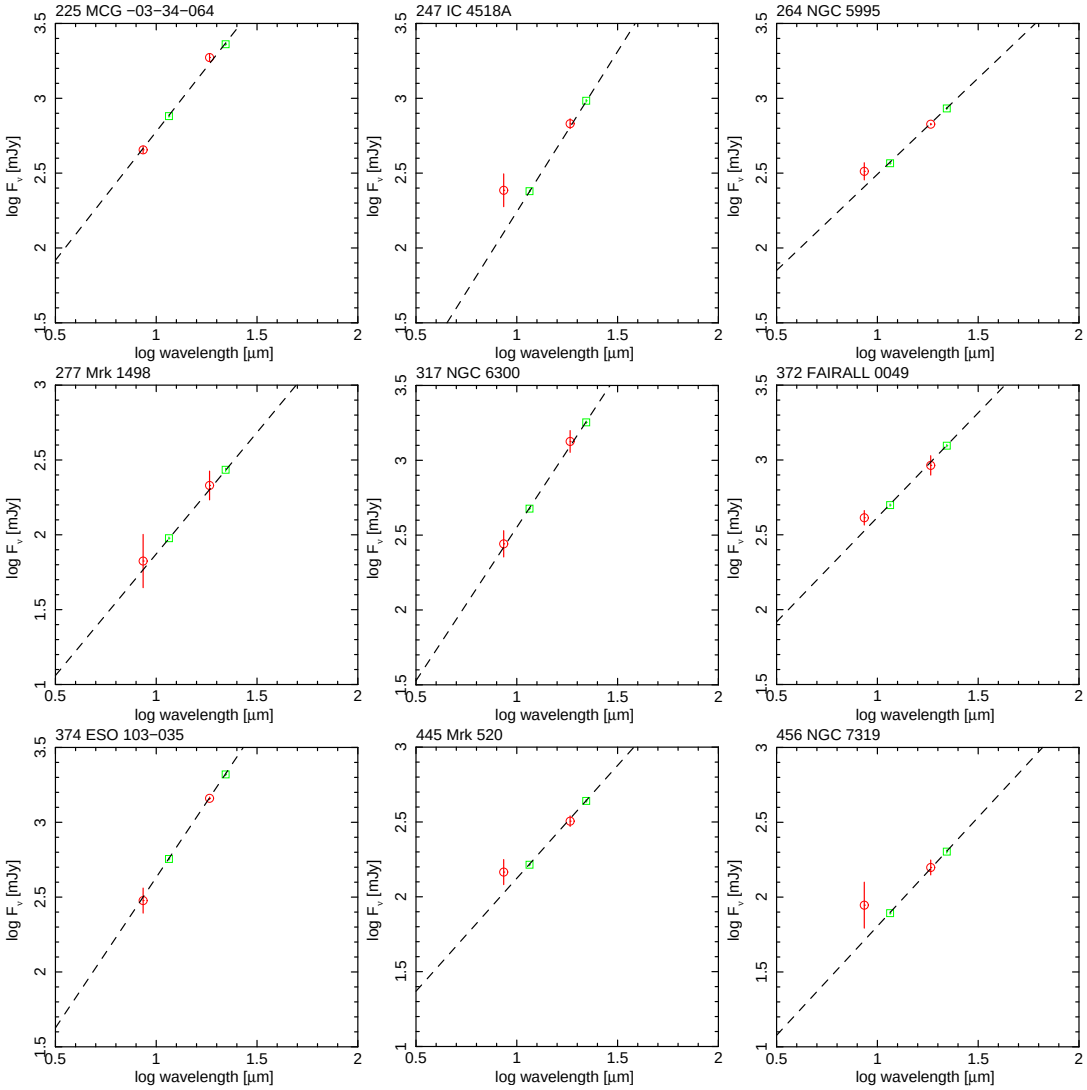

Figure B.2: *Continued.*

Type 1 radio-loud AGN

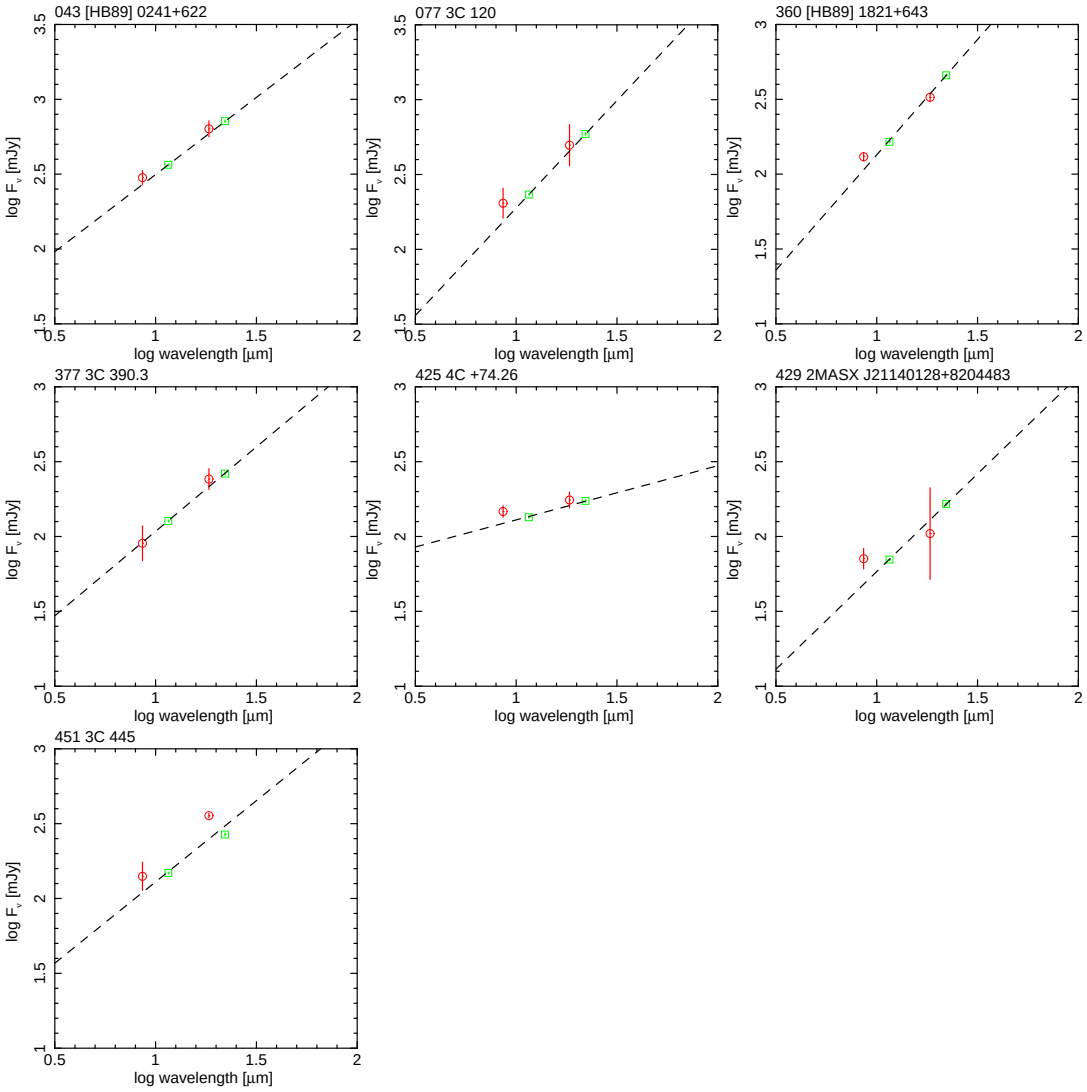

Figure B.3: SEDs of type 1 radio-loud AGN with *AKARI* (red point) and *WISE* (green point) bands. In each panel, data points are plotted for the isophotal wavelengths defined as 8.61, 11.56, 18.39, and 22.09 μm for S9W, W3, L18W, and W4, respectively. Object number in the 22-month *Swift*/BAT hard X-ray survey catalog and object name are shown on the top left of a figure. Broken line is the best-fit power-law model to the data.

Type 2 radio-loud AGN

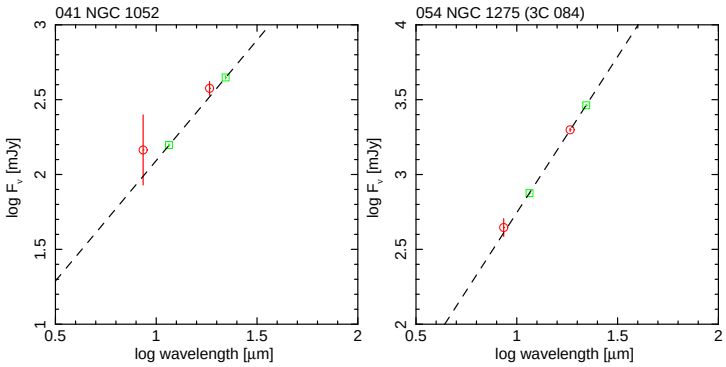

Figure B.4: SEDs of type 2 radio-loud AGN with *AKARI* (red point) and *WISE* (green point) bands. In each panel, data points are plotted for the isophotal wavelengths defined as 8.61, 11.56, 18.39, and 22.09 μm for S9W, W3, L18W, and W4, respectively. Object number in the 22-month *Swift*/BAT hard X-ray survey catalog and object name are shown on the top left of a figure. Broken line is the best-fit power-law model to the data.

Compton-thick AGN

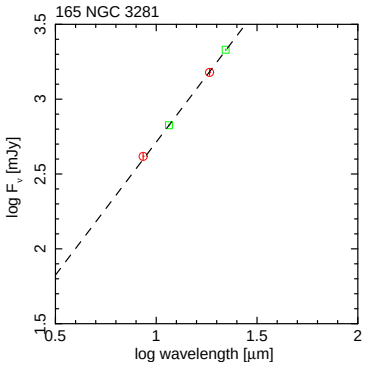

Figure B.5: SEDs of Compton-thick AGN with *AKARI* (red point) and *WISE* (green point) bands. In each panel, data points are plotted for the isophotal wavelengths defined as 8.61, 11.56, 18.39, and 22.09 μm for S9W, W3, L18W, and W4, respectively. Object number in the 22-month *Swift*/BAT hard X-ray survey catalog and object name are shown on the top left of a figure. Broken line is the best-fit power-law model to the data.

Blazar

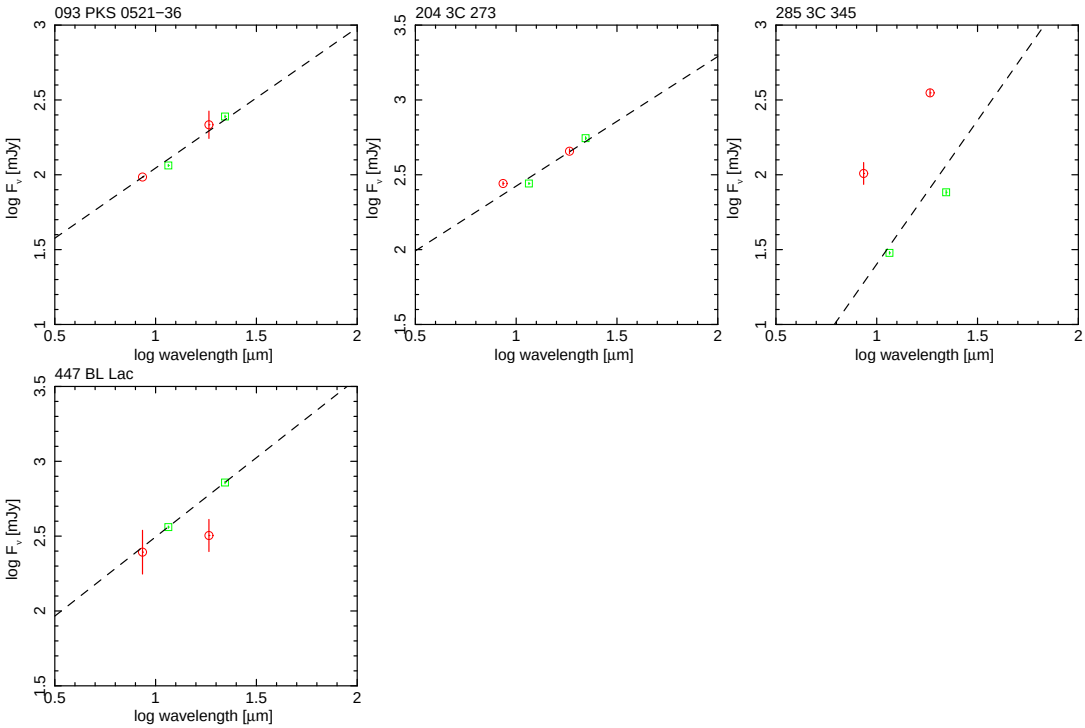

Figure B.6: SEDs of Blazar with *AKARI* (red point) and *WISE* (green point) bands. In each panel, data points are plotted for the isophotal wavelengths defined as 8.61, 11.56, 18.39, and 22.09 μm for S9W, W3, L18W, and W4, respectively. Object number in the 22-month *Swift*/BAT hard X-ray survey catalog and object name are shown on the top left of a figure. Broken line is the best-fit power-law model to the data.

LINER

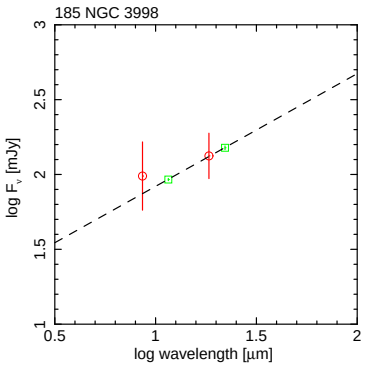

Figure B.7: SEDs of LINER with *AKARI* (red point) and *WISE* (green point) bands. In each panel, data points are plotted for the isophotal wavelengths defined as 8.61, 11.56, 18.39, and 22.09 μm for S9W, W3, L18W, and W4, respectively. Object number in the 22-month *Swift*/BAT hard X-ray survey catalog and object name are shown on the top left of a figure. Broken line is the best-fit power-law model to the data.

Appendix C

Relative calibration error between *AKARI* and *WISE*

When comparing of observed fluxes between different satellites, we need to consider relative calibration error because the standard magnitudes (bandpasses) are different between them. Therefore, I estimate relative calibration error between *AKARI* and *WISE* by using bright stars. In this calculation, I use A- and F-type stars observed by both *AKARI* and *WISE* because their spectra in IR bands can be approximated by Black body radiation.

I show plots of Signal-to-Noise ratios of *AKARI* for A- and F-type stars, which are detected by *AKARI* and *WISE* simultaneously (Figure C.1). I select bright stars based on *AKARI* fluxes, following as,

- Flux $>$ 800 mJy, and S/N $>$ 50: *AKARI* 9 μm
- Flux $>$ 300 mJy, and S/N $>$ 10: *AKARI* 18 μm.

S/N is calculated by the flux divided by the flux error.

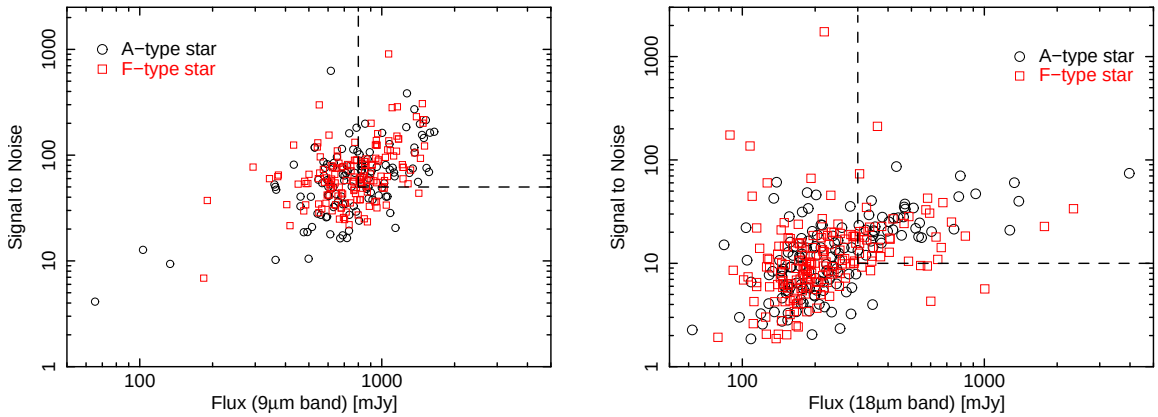

Figure C.1: Signal-to-Noise ratio of A- and F-type stars detected by *AKARI* and *WISE* bands. Black and red circle shows the A- and F-type star. The abscissa show fluxes of *AKARI* (9 and 18 μm). The ordinate show Signal-to-Noise ratio. The upper-right region as indicate by the dotted box shows the selection as bright sources.

I calculate relative flux ratio ΔF (i.e., $\frac{F_{\rm W}-F_{\rm A}}{F_{\rm A}}$) for selected-bright stars, and show the distribution of ΔF (Figure C.2). Also, I fit this distribution by using Gaussian model, and summarize results of fitting in Table C.1.

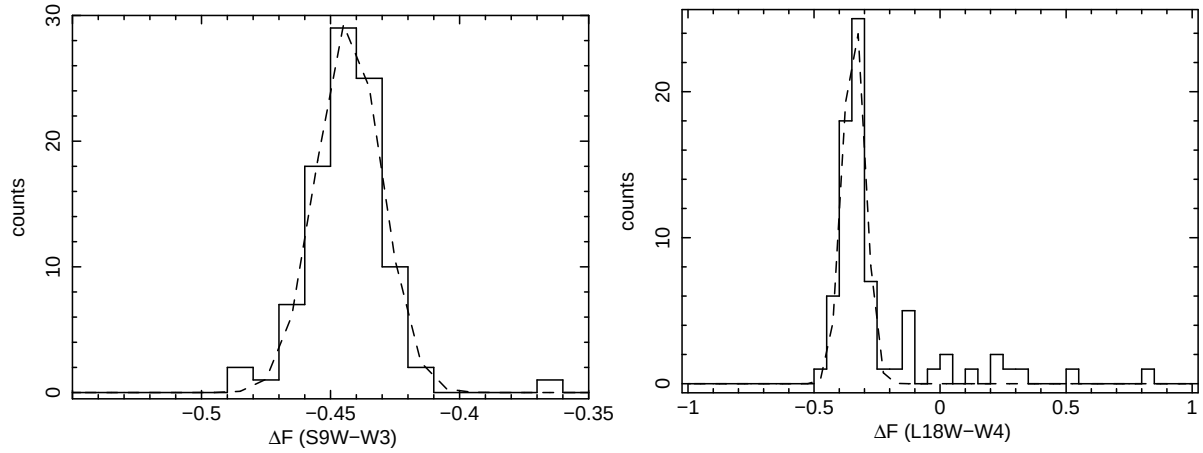

Figure C.2: Distribution of ΔF for A- and F-type stars between *AKARI* and *WISE* bands. Solid line shows the distribution of ΔF by using cataloged fluxes. Dashed line shows the fitted model of the Gaussian.

Table C.1: Statistics of ΔF of stars

AKARI/*WISE* [μm]	A/F type	ΔF	
		average	standard deviation
(1)	(2)	(3)	(4)
9 /12	38/57	-0.443	0.012 ± 0.001
18/22	40/34	-0.342	0.044 ± 0.004

Col. 1: Wavelengths of observations. Col. 2: Number of A- and F- stars in each band. Col. 3: Average of ΔF. Col. 4: standard deviation of ΔF.

Next, I calculate ΔF by using the Plank spectrum. The Plank function is described as,

$$F_\nu(T) = \frac{2h\nu^3/c^2}{\exp(h\nu/kT) - 1}. \tag{C.1}$$

When the temperature of F0 star (7200 K), the ΔF is calculated as -0.428 and -0.301 in S9W-W3 and L18W-W4, respectively. The difference ΔF between the observation and model is -0.015 and -0.041. Therefore, I can obtain relative calibration error as 1.5% and 4.1% in S9W-W3 and L18W-W4, respectively.

Bibliography

Abdo, A. A., Ackermann, M., Agudo, I., et al. 2010, ApJ, 716, 30

Angel, J. R. P., & Stockman, H. S. 1980, ARA&A, 18, 321

Antonucci, R. 1993, ARA&A, 31, 473

—. 2011, ArXiv e-prints

Asmus, D., Gandhi, P., Smette, A., Hönig, S. F., & Duschl, W. J. 2011, A&A, 536, A36

Ballo, L., Braito, V., Reeves, J. N., Sambruna, R. M., & Tombesi, F. 2011, MNRAS, 418, 2367

Barvainis, R. 1987, ApJ, 320, 537

Barvainis, R., Lehár, J., Birkinshaw, M., Falcke, H., & Blundell, K. M. 2005, ApJ, 618, 108

Bauer, M., Pietsch, W., Trinchieri, G., et al. 2008, A&A, 489, 1029

Blandford, R. D., & Ostriker, J. P. 1978, ApJL, 221, L29

Blundell, K. M., & Rawlings, S. 2001, ApJl, 562, L5

Bodaghee, A., Courvoisier, T. J.-L., Rodriguez, J., et al. 2007, A&A, 467, 585

Brandl, B. R., Bernard-Salas, J., Spoon, H. W. W., et al. 2006, ApJ, 653, 1129

Bregman, J. N. 1990, A&A, 2, 125

Bregman, J. N., Glassgold, A. E., Huggins, P. J., et al. 1986, ApJ, 301, 708

Bridle, A. H., & Perley, R. A. 1984, ARA&A, 22, 319

Carleton, N. P., Elvis, M., Fabbiano, G., et al. 1987, ApJ, 318, 595

Clavel, J., Wamsteker, W., & Glass, I. S. 1989, ApJ, 337, 236

Comastri, A. 2004, in Astrophysics and Space Science Library, Vol. 308, Supermassive Black Holes in the Distant Universe, ed. A. J. Barger, 245

Comastri, A., Iwasawa, K., Gilli, R., et al. 2010, ApJ, 717, 787

Courvoisier, T. J.-L., Turner, M. J. L., Robson, E. I., et al. 1987, A&A, 176, 197

Cusumano, G., La Parola, V., Segreto, A., et al. 2010, A&A, 524, A64

Dale, D. A., Smith, J. D. T., Armus, L., et al. 2006, ApJ, 646, 161

Daly, R. A. 1990, ApJ, 355, 416

della Ceca, R., Griffiths, R. E., Heckman, T. M., Lehnert, M. D., & Weaver, K. A. 1999, ApJ, 514, 772

Dicken, D., Tadhunter, C., Axon, D., et al. 2010, ApJ, 722, 1333

Donato, D., Ghisellini, G., Tagliaferri, G., & Fossati, G. 2001, A&A, 375, 739

Dullemond, C. P., & van Bemmel, I. M. 2005, A&A, 436, 47

Edelson, R. A., & Malkan, M. A. 1987, ApJ, 323, 516

Elitzur, M. 2008, NewAR, 52, 274

Elvis, M. 2000, ApJ, 545, 63

Elvis, M., Wilkes, B. J., McDowell, J. C., et al. 1994, ApJs, 95, 1

Enya, K., Yoshii, Y., Kobayashi, Y., et al. 2002a, ApJS, 141, 23

—. 2002b, ApJS, 141, 31

—. 2002c, ApJS, 141, 45

Evans, D. A., Worrall, D. M., Hardcastle, M. J., Kraft, R. P., & Birkinshaw, M. 2006, ApJ, 642, 96

Fanaroff, B. L., & Riley, J. M. 1974, MNRAS, 167, 31P

Fossati, G., Maraschi, L., Celotti, A., Comastri, A., & Ghisellini, G. 1998, MNRAS, 299, 433

Gandhi, P., Crawford, C. S., Fabian, A. C., & Johnstone, R. M. 2004, MNRAS, 348, 529

Gandhi, P., Fabian, A. C., & Crawford, C. S. 2006, MNRAS, 369, 1566

Gandhi, P., Horst, H., Smette, A., et al. 2009, A&A, 502, 457

Genzel, R., Lutz, D., Sturm, E., et al. 1998, ApJ, 498, 579

González Delgado, R. M., Heckman, T., Leitherer, C., et al. 1998, ApJ, 505, 174

González-Martín, O., Papadakis, I., Braito, V., et al. 2011, A&A, 527, A142

Gorjian, V., Werner, M. W., Jarrett, T. H., Cole, D. M., & Ressler, M. E. 2004, ApJ, 605, 156

Goulding, A. D., & Alexander, D. M. 2009, MNRAS, 398, 1165

Grandi, P., & Palumbo, G. G. C. 2007, ApJ, 659, 235

Grandi, P., Tagliaferri, G., Giommi, P., Barr, P., & Palumbo, G. G. C. 1992, ApJS, 82, 93

Haardt, F., & Maraschi, L. 1993, ApJ, 413, 507

Hardcastle, M. J., Evans, D. A., & Croston, J. H. 2009, MNRAS, 396, 1929

Heckman, T. M. 1980, A&A, 87, 152

Ho, L. C., & Peng, C. Y. 2001, ApJ, 555, 650

Ho, L. C., & Ulvestad, J. S. 2001, ApJS, 133, 77

Hoffman, D. I., Cutri, R. M., Masci, F. J., et al. 2012, AJ, 143, 118

Hönig, S. F., Beckert, T., Ohnaka, K., & Weigelt, G. 2006, A&A, 452, 459

Hönig, S. F., & Kishimoto, M. 2010, A&A, 523, A27

—. 2011, A&A, 534, A121

Hönig, S. F., Kishimoto, M., Gandhi, P., et al. 2010, A&A, 515, A23

Horst, H., Duschl, W. J., Gandhi, P., & Smette, A. 2009, A&A, 495, 137

Horst, H., Gandhi, P., Smette, A., & Duschl, W. J. 2008, A&A, 479, 389

Horst, H., Smette, A., Gandhi, P., & Duschl, W. J. 2006, A&A, 457, L17

Hunt, L. K., Zhekov, S., Salvati, M., Mannucci, F., & Stanga, R. M. 1994, A&A, 292, 67

Ichikawa, K., Ueda, Y., Terashima, Y., et al. 2012, ApJ, 754, 45

Ikeda, S., Awaki, H., & Terashima, Y. 2009, ApJ, 692, 608

Imanishi, M., Dudley, C. C., Maiolino, R., et al. 2007, ApJs, 171, 72

Ishihara, D., Onaka, T., Kataza, H., et al. 2010, A&A, 514, A1

Isobe, T., Feigelson, E. D., Akritas, M. G., & Babu, G. J. 1990, ApJ, 364, 104

Itoh, T., Done, C., Makishima, K., et al. 2008, PASJ, 60, 251

Iwasawa, K., Sanders, D. B., Evans, A. S., et al. 2005, MNRAS, 357, 565

Iyomoto, N., Fukazawa, Y., Nakai, N., & Ishihara, Y. 2001, ApJl, 561, L69

Jaffe, W., Meisenheimer, K., Röttgering, H. J. A., et al. 2004, Nature, 429, 47

Jarrett, T. H., Cohen, M., Masci, F., et al. 2011, ApJ, 735, 112

Joint Iras Science, W. G. 1994, VizieR Online Data Catalog, 2125, 0

Kaneda, H., Yamagishi, M., Suzuki, T., & Onaka, T. 2009, ApJl, 698, L125

Kaneda, H., Ishihara, D., Suzuki, T., et al. 2010, A&A, 514, A14

Kataoka, J., Reeves, J. N., Iwasawa, K., et al. 2007, PASJ, 59, 279

Kawaguchi, T., & Mori, M. 2010, ApJL, 724, L183

Kellermann, K. I., Sramek, R., Schmidt, M., Shaffer, D. B., & Green, R. 1989, AJ, 98, 1195

Kishimoto, M., Hönig, S. F., Beckert, T., & Weigelt, G. 2007, A&A, 476, 713

Koratkar, A., & Blaes, O. 1999, PASP, 111, 1

Kozłowski, S., Kochanek, C. S., Stern, D., et al. 2010, ApJ, 716, 530

Krabbe, A., Böker, T., & Maiolino, R. 2001, ApJ, 557, 626

Krolik, J. H., & Begelman, M. C. 1988, ApJ, 329, 702

Lagache, G., Dole, H., & Puget, J.-L. 2003, MNRAS, 338, 555

Laurent, O., Mirabel, I. F., Charmandaris, V., et al. 2000, A&A, 359, 887

Lawrence, A. 1991, MNRAS, 252, 586

Leipski, C., Haas, M., Willner, S. P., et al. 2010, ApJ, 717, 766

Levenson, N. A., Radomski, J. T., Packham, C., et al. 2009, ApJ, 703, 390

Lutz, D., Maiolino, R., Spoon, H. W. W., & Moorwood, A. F. M. 2004, A&A, 418, 465

Maiolino, R., Salvati, M., Bassani, L., et al. 1998, A&A, 338, 781

Malkan, M. A., Gorjian, V., & Tam, R. 1998, ApJs, 117, 25

Malmrose, M. P., Marscher, A. P., Jorstad, S. G., Nikutta, R., & Elitzur, M. 2011, ApJ, 732, 116

Marchese, E., Della Ceca, R., Caccianiga, A., et al. 2012, A&A, 539, A48

Matt, G. 2000, A&A, 355, L31

Matt, G., Fabian, A. C., Guainazzi, M., et al. 2000, MNRAS, 318, 173

Matt, G., Guainazzi, M., Frontera, F., et al. 1997, A&A, 325, L13

Matt, G., Guainazzi, M., Maiolino, R., et al. 1999, A&A, 341, L39

McHardy, I. 1988, MmSAI, 59, 239

McHardy, I., Lawson, A., Newsam, A., et al. 1999, MNRAS, 310, 571

Meléndez, M., Kraemer, S. B., Armentrout, B. K., et al. 2008, ApJ, 682, 94

Miller, L., Turner, T. J., & Reeves, J. N. 2008, A&A, 483, 437

Molina, M., Bassani, L., Malizia, A., et al. 2008, MNRAS, 390, 1217

Moorwood, A. F. M., van der Werf, P. P., Kotilainen, J. K., Marconi, A., & Oliva, E. 1996, A&A, 308, L1

Mor, R., Netzer, H., & Elitzur, M. 2009, ApJ, 705, 298

Moran, E. C., Lehnert, M. D., & Helfand, D. J. 1999, ApJ, 526, 649

Mulchaey, J. S., Koratkar, A., Ward, M. J., et al. 1994, ApJ, 436, 586

Mullaney, J. R., Alexander, D. M., Goulding, A. D., & Hickox, R. C. 2011, MNRAS, 414, 1082

Murakami, H., Baba, H., Barthel, P., et al. 2007, PASJ, 59, 369

Mushotzky, R. F., Done, C., & Pounds, K. A. 1993, ARA&A, 31, 717

Mushotzky, R. F., Winter, L. M., McIntosh, D. H., & Tueller, J. 2008, ApJL, 684, L65

Nenkova, M., Ivezić, Ž., & Elitzur, M. 2002, ApJL, 570, L9

Nenkova, M., Sirocky, M. M., Nikutta, R., Ivezić, Ž., & Elitzur, M. 2008, ApJ, 685, 160

Neugebauer, G., & Matthews, K. 1999, AJ, 118, 35

Neugebauer, G., Soifer, B. T., Matthews, K., & Elias, J. H. 1989, AJ, 97, 957

Osterbrock, D. E. 1989, Astrophysics of gaseous nebulae and active galactic nuclei

Padovani, P. 1992, MNRAS, 257, 404

Persic, M., & Rephaeli, Y. 2002, A&A, 382, 843

Pier, E. A., & Krolik, J. H. 1992, ApJ, 401, 99

—. 1993, ApJ, 418, 673

Pietsch, W., Roberts, T. P., Sako, M., et al. 2001, A&A, 365, L174

Plotkin, R. M., Anderson, S. F., Brandt, W. N., et al. 2012, ApJl, 745, L27

Polletta, M., Tajer, M., Maraschi, L., et al. 2007, ApJ, 663, 81

Ranalli, P., Comastri, A., Origlia, L., & Maiolino, R. 2008, MNRAS, 386, 1464

Ranalli, P., Comastri, A., & Setti, G. 2003, A&A, 399, 39

Rees, M. J. 1989, MNRAS, 239, 1P

Rigby, J. R., Diamond-Stanic, A. M., & Aniano, G. 2009, ApJ, 700, 1878

Risaliti, G., Elvis, M., & Nicastro, F. 2002, ApJ, 571, 234

Risaliti, G., Maiolino, R., & Salvati, M. 1999, ApJ, 522, 157

Risaliti, G., Braito, V., Laparola, V., et al. 2009, ApJl, 705, L1

Robson, E. I., Litchfield, S. J., Gear, W. K., et al. 1993, MNRAS, 262, 249

Russell, H. R., Fabian, A. C., Sanders, J. S., et al. 2010, MNRAS, 402, 1561

Sambruna, R. M., Eracleous, M., & Mushotzky, R. F. 1999, ApJ, 526, 60

Sanders, D. B., & Mirabel, I. F. 1996, ARA&A, 34, 749

Sanders, D. B., Phinney, E. S., Neugebauer, G., Soifer, B. T., & Matthews, K. 1989, ApJ, 347, 29

Schartmann, M., Meisenheimer, K., Camenzind, M., et al. 2008, A&A, 482, 67

Schmidt, M., & Green, R. F. 1983, ApJ, 269, 352

Schweitzer, M., Lutz, D., Sturm, E., et al. 2006, ApJ, 649, 79

Simpson, C. 2005, MNRAS, 360, 565

Soria, R., & Motch, C. 2004, A&A, 422, 915

Stein, W. A., Odell, S. L., & Strittmatter, P. A. 1976, ARA&A, 14, 173

Sturm, E., Lutz, D., Verma, A., et al. 2002, A&A, 393, 821

Suganuma, M., Yoshii, Y., Kobayashi, Y., et al. 2006, ApJ, 639, 46

Sunyaev, R. A., & Titarchuk, L. G. 1980, A&A, 86, 121

Taniguchi, Y., Ikeuchi, S., & Shioya, Y. 1999, ApJL, 514, L9

Tazaki, F., Ueda, Y., Ishino, Y., et al. 2010, ApJ, 721, 1340

Teng, S. H., Veilleux, S., Anabuki, N., et al. 2009, ApJ, 691, 261

Tueller, J., Mushotzky, R. F., Barthelmy, S., et al. 2008, ApJ, 681, 113

Tueller, J., Baumgartner, W. H., Markwardt, C. B., et al. 2010, ApJs, 186, 378

Ueda, Y., Akiyama, M., Ohta, K., & Miyaji, T. 2003, ApJ, 598, 886

Ulrich, M.-H., Maraschi, L., & Urry, C. M. 1997, ARA&A, 35, 445

Unwin, S. C., Wehrle, A. E., Lobanov, A. P., et al. 1997, ApJ, 480, 596

Urry, C. M., & Padovani, P. 1995, PASP, 107, 803

Vasudevan, R. V., & Fabian, A. C. 2007, MNRAS, 381, 1235

Vasudevan, R. V., Fabian, A. C., Gandhi, P., Winter, L. M., & Mushotzky, R. F. 2010, MNRAS, 402, 1081

Vermeulen, R. C., Ros, E., Kellermann, K. I., et al. 2003, A&A, 401, 113

Véron-Cetty, M.-P., & Véron, P. 2010, A&A, 518, A10

Vignali, C., Brandt, W. N., & Schneider, D. P. 2003, AJ, 125, 433

Vignali, C., & Comastri, A. 2002, A&A, 381, 834

Vignati, P., Molendi, S., Matt, G., et al. 1999, A&A, 349, L57

Weaver, K. A., Meléndez, M., Mushotzky, R. F., et al. 2010, ApJ, 716, 1151

Winter, L. M., Mushotzky, R. F., Reynolds, C. S., & Tueller, J. 2009, ApJ, 690, 1322

Wright, E. L., Eisenhardt, P. R. M., Mainzer, A. K., et al. 2010, AJ, 140, 1868

Xu, C., Livio, M., & Baum, S. 1999, AJ, 118, 1169

Yamamura, I., Makiuti, S., Ikeda, N., et al. 2010, VizieR Online Data Catalog, 2298, 0

Yamauchi, C., Fujishima, S., Ikeda, N., et al. 2011, PASP, 123, 852

Zakamska, N. L., Strauss, M. A., Krolik, J. H., et al. 2003, AJ, 126, 2125

Zezas, A. L., Georgantopoulos, I., & Ward, M. J. 1998, MNRAS, 301, 915

Acknowledgment

This research is based on observations with *AKARI*, a JAXA project with the participation of ESA and *Swift*/BAT, a NASA project with an international team. Also, this publication makes use of data products from the *WISE*, which is a joint project of the University of California, Los Angeles, and the Jet Propulsion Laboratory/California Institute of Technology, funded by the National Aeronautics and Space Administration.

In the three years for this work, I have been supported by many people and think that I would not complete this thesis without their help.

Firstly I am very grateful for my supervisor Professor T. Dotani, who has guided and encouraged me to write this doctor thesis. I feel myself fortunate to be given his valuable advice and knowledge about astrophysics. I have learned a lot of things from his strict attitude for deriving and treating scientific result. And I would like to thank post-doctor P. Gandhi, who always gave accurate instructions to me. He always encouraged me and gave useful advice.

Professor T. Nakagawa and associate professor K. Enya have great knowledge and experience about mid-IR variability, I would thank for useful discussion with them. Also associate professor I. Yamamura and post-doctor S. Takita advised me kindly how to use the *AKARI*/PSC.

I thank colleagues and friends at ISAS: T. Fujinaga, K. Saitoh, T. Sato, Y. Koseki, N. Katayama, R. Hirano, Y. Toba, K. Kusuno, T. Haga, and K. Hanawa. A little discussion and a lot of trivial talk with them is precious memory for my life. I also wish to thank A. Koyama who is a secretary of our laboratory. I always refresh with her interesting story.

Finally, I would acknowledge my father, mother and brother for their great help. The support of my mind when I seem to fail is always their kindness and tenderness.